Institut für Geodäsie und Geoinformation

Strategies for the Empirical Determination of the Stochastic Properties of Terrestrial Laser Scans

Dissertation

zur

Erlangung des akademischen Grades

Doktor der Ingenieurwissenschaften (Dr.–Ing.)

der

Landwirtschaftlichen Fakultät

der

Rheinischen Friedrich–Wilhelms–Universität Bonn

vorgelegt von

M.Sc. Berit Henrike Jost

geb. Schmitz

aus Dormagen

Bonn 2023

Referent:	Prof. Dr. Heiner Kuhlmann
Korreferent:	Prof. Dr. Christoph Holst
Korreferent:	Prof. Dr. Andreas Wieser

Tag der mündlichen Prüfung: 23. Juni 2023

Angefertigt mit Genehmigung der Landwirtschaftlichen Fakultät der Universität Bonn

Strategies for the Empirical Determination of the Stochastic Properties of Terrestrial Laser Scans

Abstract

Terrestrial laser scanners (TLS) are suitable for the surface approximation of objects and their geometric changes due to the temporally and spatially high-frequent data acquisition. However, precise geodetic engineering tasks require detailed knowledge about the performance of the sensors and especially about their uncertainty to use them for precise measurements, e.g., in deformation analysis or surface approximations. Due to the complex transition behavior between error sources and effects on the point cloud, the correct description of the point cloud's stochastic model represented by the variance-covariance matrix is not yet solved. In particular, the interaction of the laser beam with the environment and the measurement object, taking into account different measurement arrangements (distances and angles of incidence), is so diverse that it is impossible to model all errors. However, if these errors are neglected in the stochastic model, this can lead to biased surface approximations, incorrect statistical tests, or misinterpreting errors as deformations. For this reason, strategies for the empirical determination of the stochastic properties of terrestrial laser scans are developed in this dissertation. In particular, the determination of the range precision for different surfaces and measurement configurations, as well as correlations between individual measurement points, are in focus. Specifically, the following aspects are addressed:

- The object surface and scanning configuration mainly influence the range precision, which the reflected intensity of the laser beam can fully describe. This work contributes to efficiently determining the range precision by presenting a test field simplified for users and further developing the existing methodology. This contributes to a more realistic description of the main diagonal of the variance-covariance matrix representing the stochastic model.
- Especially the interaction of the laser beam with the object is individual as it depends on the surface. The laser spot is integrated over a certain area, and neighboring laser spots overlap due to the dense acquisition of data points. This results in a smoothing effect and leads to the fact that the resolution capability of the scanner does not match the resolution set in the scanner. This thesis develops a new method for determining the resolution capability, which enables a more economic measurement planning. Furthermore, correlations are derived from overlapping laser spots, which are integrated into the stochastic model.
- These rather short-scale correlations can be determined empirically via another method developed in this thesis. For this purpose, the stochastic signal of the point cloud must first be separated from the deterministic part. This is done with the help of a reference geometry generated with a sensor of higher accuracy. Subsequently, this work presents two methods for quantifying the short-scale correlations in the point cloud.
- The previous methods can be implemented well for point clouds of smaller objects (approximately up to 2 m x 2 m). However, this is not straightforward to realize for larger objects as the stochastic properties change within the point cloud. Furthermore, a reference geometry is not easy to establish due to a lack of suitable sensors and deformations of the reference objects. For this reason, this thesis presents a method for creating a reference geometry of a larger object that allows for the analysis of long-scale correlations.

These different aspects provide a better understanding of the uncertainties in terrestrial laser scanning and, thus, form the basis for setting up a more realistic stochastic model of the point cloud to make statistically more reliable statements in a deformation analysis and unbiased surface approximations. Furthermore, the presented strategies do not require special laboratory conditions but can be performed by qualified users if an appropriate object, such as a roughly planar wall, is available.

Strategien zur empirischen Bestimmung der stochastischen Eigenschaften terrestrischer Laserscans

Zusammenfassung

Terrestrische Laserscanner (TLS) eignen sich durch die zeitlich und räumlich hochfrequente Datenaufnahme zur flächenhaften Aufnahme von Objekten und deren geometrischen Änderungen. Präzise ingenieurgeodätische Aufgaben, z.B. Deformationsanalysen oder Flächenapproximationen, erfordern allerdings detailliertes Wissen über die Genauigkeit der Sensoren. Durch das komplexe Transferverhalten zwischen Abweichungsquellen und Auswirkungen auf die Punktwolke, ist die korrekte Beschreibung ihres stochastischen Modells eine bisher ungelöste Aufgabe. Insbesondere die Interaktion des Laserstrahls mit der Umgebung und dem Messobjekt unter Berücksichtigung unterschiedlicher Messanordnungen (Strecken und Einfallswinkel) ist so vielfältig, dass eine Modellierung aller Abweichungen nicht möglich ist. Werden diese Abweichungen allerdings im stochastischen Modell vernachlässigt, so kann dies zu verzerrten Flächenapproximationen, falschen statistischen Tests oder einer Fehlinterpretation von Abweichungen als Deformationen führen. Aus diesem Grund werden in der vorliegenden Dissertation Strategien zur empirischen Bestimmung der stochastischen Eigenschaften terrestrischer Laserscans entwickelt. Speziell wird auf die folgenden Aspekte eingegangen:

- Die Streckenpräzision wird maßgeblich durch die Objektoberfläche und die Messkonfiguration beeinflusst. Diese beiden Einflüsse lassen sich vollständig durch die zurückgestrahlte Intensität des Laserstrahls beschreiben. Diese Arbeit liefert einen Beitrag zur effizienten Bestimmung der Streckenpräzision, indem sie ein für Nutzer vereinfachtes Testfeld präsentiert und die vorhandene Methodik weiterentwickelt. Dies liefert einen Beitrag zur realistischeren Beschreibung der Hauptdiagonalen der Kovarianzmatrix, welche das stochastische Modell repräsentiert.
- Besonders die Interaktion des Laserstrahls mit dem Objekt ist sehr individuell und abhängig von der Oberfläche. Der Laserspot wird über einen gewissen Bereich integriert und benachbarte Laserspots überlappen sich durch die räumlich hochfrequente Aufnahme des Scanners. Dadurch entstehen Verschmierungseffekte, die dazu führen, dass das tatsächliche Auflösungsvermögen des Scanners nicht mit der im Scanner eingestellten Auflösung übereinstimmt. Diese Arbeit entwickelt eine neue Methode zur Bestimmung des Auflösungsvermögens, was eine wirtschaftlichere Messplanung ermöglicht. Des Weiteren werden Korrelationen aus den sich überlappenden Laserspots abgeleitet, die in das stochastische Modell integriert werden.
- Diese eher kleinräumigen Korrelationen können über eine weitere Methode empirisch bestimmt werden. Dazu muss zunächst das stochastische Signal der Punktwolke von dem deterministischen Anteil getrennt werden. Dies erfolgt mithilfe einer Referenzgeometrie, die mit einem Sensor höherer Genauigkeit generiert wird. Anschließend präsentiert diese Arbeit zwei Methoden zur Quantifizierung der kleinräumigen Korrelationen in der Punktwolke.
- Die vorangegangenen Methoden lassen sich für Punktwolken kleinerer Objekte (ca. bis 2 m x 2 m) gut realisieren. Für größere Objekte ist dies allerdings nicht so einfach, da sich zum einen die stochastischen Eigenschaften der Punktwolke stark ändern und zum anderen eine Referenzgeometrie aufgrund von mangelnden Sensoren und Deformationen großer Objekte nicht einfach zu erstellen ist. Aus diesem Grund wird in dieser Arbeit eine Methode zur Erstellung einer Referenzgeometrie eines größeren Objektes präsentiert, die die Analyse von großräumigen Korrelationen erlaubt.

Diese verschiedenen Aspekte vermitteln ein besseres Verständnis für die Unsicherheiten beim terrestrischen Laserscanning und bilden somit die Basis ein realistischeres stochastisches Modell der Punktwolke aufzustellen, um statistisch sicherere Aussagen bei einer Deformationsanalyse und unverzerrte Flächenapproximationen zu tätigen. Die dargelegten Strategien benötigen keine speziellen Laborbedingungen, sondern können von qualifizierten Anwendern durchgeführt werden falls geeignete Objekte, wie z.B. eine grob planare Wand zur Verfügung stehen.

Inhaltsverzeichnis

Preface

This cumulative dissertation presents the development of strategies for empirically analyzing the stochastic properties of terrestrial laser scans. It is based on the following seven publications that were all subject to a peer-review process. It must be noted that the author changed her last name from Schmitz to Jost in 2022:

- **Publication A** (Peer-reviewed, Journal):
  Schmitz, B., Holst, C., Medic, T., Lichti, D. D., & Kuhlmann, H. (2019). How to Efficiently Determine the Range Precision of 3D Terrestrial Laser Scanners. *Sensors*, 19(6), 1466. `https://doi.org/10.3390/s19061466`
- **Publication B** (Peer-reviewed, Journal):
  Schmitz, B., Kuhlmann, H., & Holst, C. (2020). Investigating the resolution capability of terrestrial laser scanners and its impact on the effective number of measurements. *ISPRS Journal of Photogrammetry and Remote Sensing*, 159, 41–52. `https://doi.org/10.1016/j.isprsjprs.2019.11.002`
- **Publication C** (Peer-reviewed, Conference):
  Schmitz, B., Coopmann, D., Kuhlmann, H., & Holst, C. (2021a). Using the Resolution Capability and the Effective Number of Measurements to Select the Right Terrestrial Laser Scanner. In *Contributions to International Conferences on Engineering Surveying, INGEO & SIG 2020, Dubrovnik, Croatia. Springer Proceedings in Earth and Environmental Sciences* (pp. 85–97).: Springer, Cham
- **Publication D** (Peer-reviewed, Journal):
  Schmitz, B., Kuhlmann, H., & Holst, C. (2021c). Towards the empirical determination of correlations in terrestrial laser scanner range observations and the comparison of the correlation structure of different scanners. *ISPRS Journal of Photogrammetry and Remote Sensing*, 182, 228–241. `https://doi.org/10.1016/j.isprsjprs.2021.10.012`
- **Publication E** (Peer-reviewed, Journal):
  Schmitz, B., Kuhlmann, H., & Holst, C. (2021b). Deformation analysis of a reference wall towards the uncertainty investigation of terrestrial laser scanners. *Journal of Applied Geodesy*, 15(3), 189–206. `https://doi.org/10.1515/jag-2020-0025`
- **Publication F** (Peer-reviewed, Conference):
  Jost, B., Holst, C., & Kuhlmann, H. (2023b). How to be more accurate than a single laser scan: Creating the reference geometry of a large wall. In A. Wieser (Ed.), *Beiträge zum 20. Internationalen Ingenieurvermessungskurs, 11.-14. April 2023, Zurich, Switzerland* (pp. 131–144).: Wichmann, Berlin, Offenbach
- **Publication G** (Peer-reviewed, Conference):
  Jost, B., Coopmann, D., Holst, C., & Kuhlmann, H. (2023a). Real movement or systematic errors? – TLS-based deformation analysis of a concrete wall. *Journal of Applied Geodesy*, 17(2), 139–149. `https://doi.org/10.1515/jag-2022-0041`

The content of these publications is summarized in Chapter 4, and their most relevant scientific results and contributions are outlined in Chapter 5 of this thesis. The author of this dissertation has made the main contribution to each of these publications and, in particular, has provided the respective methodological progress herself.

1. Motivation and Objectives

The discipline of engineering geodesy is dedicated to the constantly evolving, application-oriented problems [Kuhlmann et al., 2014]. This includes especially the transition from point-based measurements to the area-based acquisition of objects and their geometries, which is possible due to the rapid development of laser scanning technologies [Holst & Kuhlmann, 2016]. Terrestrial laser scanners (TLS) sample the environment with a very high spatial and temporal density, which leads to the possibility to stop discretizing objects with point-wise measurements but considering areal acquisitions of the objects [Kuhlmann & Schwieger, 2015, p. 747]. Hence, these instruments gain more and more importance in engineering geodesy. As the instruments have evolved and become more accurate in recent years, this offers opportunities to utilize them for engineering tasks with high accuracy demands, such as area-based deformation analyses [Mukupa et al., 2017]. However, this requires detailed knowledge of the error budget of the scanning procedure to judge the scanner's performance and to distinguish between errors related to the scanning process and real geometric changes of the object. This dissertation proposes strategies to gain a more profound knowledge of the stochastic properties of terrestrial laser scanners – more specifically, of the range variances and the correlation between measurement points. The motivation is stated in Sec. 1.1, and the detailed exposition of the objectives is given in Sec. 1.2.

1.1 Motivation

Among others, two core competencies in engineering geodesy are the monitoring of objects and the quality assessment of the measurements [Kuhlmann et al., 2014]. Both tasks together allow for a deformation analysis, which judges whether differences between two measurement epochs are a real deformation or just reasoned by the uncertainties of the measurements [Pelzer, 1971, p. 7]. To perform a deformation analysis in geodetic engineering, mainly two tasks must be solved: First, point correspondences need to be built to compute the differences between two epochs that are compared to each other [Pelzer, 1971, p. 8]. Second, a realistic variance-covariance matrix (VCM) needs to be established that represents the stochastic properties of the differences [Pelzer, 1971, p. 10]. Finally, to separate between measurement uncertainties and real deformations of the object, a statistical congruence test is carried out [Heunecke et al., 2013, p. 499]. To transfer this procedure to TLS, point correspondences between non-signalized points as well as a sophisticated description of the uncertainties represented by the VCM must be established for the TLS point cloud. The VCM contains all information on the uncertainty of a random vector described by variances and covariances [Niemeier, 2008, p. 24f.]. This thesis contributes to the latter-mentioned task as it proposes strategies to empirically determine the stochastic properties that are necessary to fill the VCM of the point cloud. A special focus lies on the range variances as they vary depending on the object surface and on the correlations as they describe the stochastic dependency between the observations [Niemeier, 2008, p. 26] that are needed to calculate the covariances.

TLS measurements are mitigated by systematic and random errors caused by internal scanner misalignments, the atmosphere, the scanning configuration, the interaction between the laser beam and the object's surface, and the registration of laser scans [Cosarca et al., 2009; Soudarissanane et al., 2011]. On the one hand, these errors impact the point coordinates and hence, the point cloud differences, which holds especially for systematic errors. On the other hand, these errors cause uncertainties in the measurements, which are quantified in the stochastic model represented by a VCM. Systematic errors that cannot be fully calibrated introduce correlations between the measurements represented by the covariances in the VCM. It is inevitable to reduce the impact of systematic errors and gain detailed knowledge of the error budget of the point cloud. Otherwise, an unbiased deformation analysis is not possible. So far, a detailed quantification of errors and their correlations is not holistically feasible due to the amount of influencing factors with complex transmission behaviors [Holst & Kuhlmann, 2016; Kauker et al., 2016]. Thus, most deformation assessments rely on the visual inspection and interpretation of the data, not on a sophisticated statistical analysis [Wunderlich et al., 2016].

Especially the integration of correlations into the VCM is often neglected due to insufficient knowledge [Holst & Kuhlmann, 2016]. However, the following two examples demonstrate the existence of correlations. Within this thesis, it is distinguished between short-scale correlations that have correlations lengths of millimeters to decimeters and long-scale correlations that have longer correlation lengths. Fig. 1.1 shows the point cloud of a black and white target with the corresponding residuals to the best-fit plane. On the one hand, the deviations in the black parts of the target exceed the ones of the white parts, which shows that the uncertainty of the laser scan strongly depends on the object's reflectivity. On the other hand, wavy scan lines are visible in the point cloud and adjacent points deviate similarly from the plane, which demonstrates the existence of short-scale correlations. This exemplary emphasizes that the stochastic model is not just constructed by the variances of the single observations, but the scanning procedure as a whole must be considered.

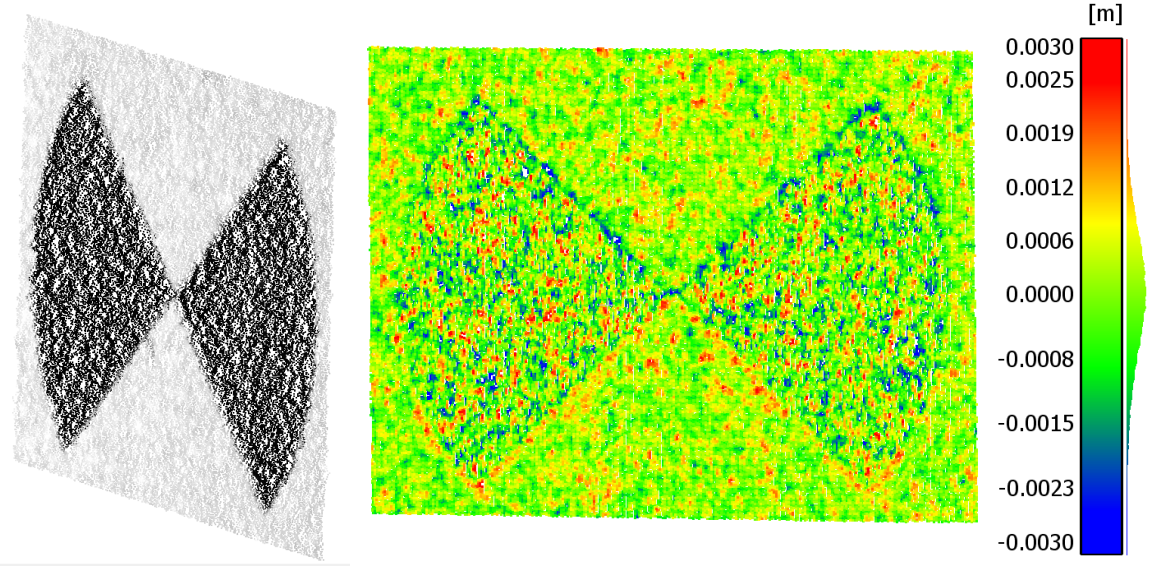

Abbildung 1.1: Left: point cloud of a black and white target; right: deviations of the point cloud to a best-fit plane.

Strategies exist to reduce the influence of systematic errors as some influences, such as internal misalignments, can be calibrated, e.g., [Holst et al., 2016a; Abbas et al., 2014; Chow et al., 2011; Lichti, 2007; Medić et al., 2017; Reshetyuk, 2009]. However, they can only be removed up to a certain precision, and some of the calibration parameters were found to change temporally [Medić et al., 2021]. Some errors from internal misalignments remain, but also errors due to the scanning geometry, the interaction between laser beam and object, and due to the atmosphere cannot or just partially be calibrated [Muralikrishnan, 2021]. They mainly affect neighboring points similarly, which are therefore correlated. Thus, the remaining errors cannot be modeled functionally and must be incorporated into the stochastic model. Otherwise, this may cause biases in the parameter estimation [Jurek et al., 2017], unrealistic parameter precision [Kuhlmann, 2001], falsified congruence testing in deformation analyses [Kermarrec et al., 2019], and misinterpretation of errors as deformations.

Fig. 1.2 depicts a Multiscale Model to Model Cloud Comparison (M3C2) [Lague et al., 2013] of two point clouds of the Bonn Reference Wall (Fig. 1.3) acquired with the Leica ScanStation P50 from two different stations. Deviations in the magnitude of ± 2.5 mm occur that are systematically distributed as large areas have deviations of the same sign and magnitude. These differences are reasoned by the effect of internal misalignments that remain after the calibration, systematic errors due to the different scan configurations, and the registration of both point clouds. Not knowing that the deviations result from systematic errors, one could misinterpret those as geometry changes of the object. Thus, these errors must either be calibrated or integrated as long-scale correlations into the VCM.

Consequently, to further evolve the two core competencies, monitoring of objects and the quality assessment of the measurements, it is necessary to gain more knowledge on the uncertainty of TLS with a special focus on determining correlations. Even though many methods exist to model the stochastic properties of

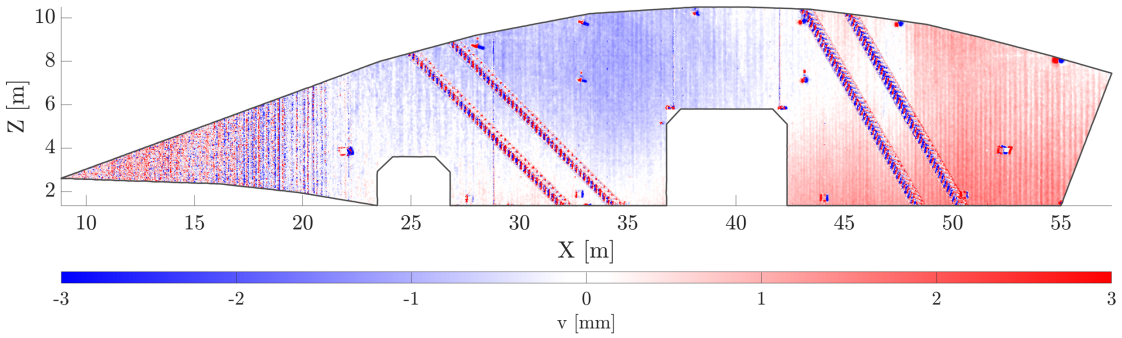

Abbildung 1.2: M3C2 point cloud comparison of two scans of the Bonn Reference Wall (Fig. 1.3) that are collected with the Leica ScanStation P50 from two different stations.

spatial data that are also applied to other geodetic disciplines, such as least-squares collocation, Kriging, spatial covariance modeling, etc., e.g., [Cressie, 1986, 1993; Moritz, 1972; Sherman, 2011], they are not yet transferred to TLS. The main problem before analyzing the stochastic properties is to separate the stochastic and the deterministic parts of the point cloud.

1.2 Objectives

The main goal of this thesis is to develop strategies, which help to gain a more profound knowledge of the stochastic properties of TLS to derive a more enhanced stochastic model, which consequently can be used to fill the VCM with more entries. All these strategies work on real data without identifying the concrete error sources as their impact on the point cloud is not always straightforward to model, and they are user-oriented to make these strategies feasible to be replicated by qualified users.

Fig. 1.3 shows a photo of the Bonn Reference Wall located on the Agricultural Campus Klein-Altendorf at the University of Bonn. It is a concrete wall of 9.50 m in height and 50 m in width. As an artistic effect, it has tire tracks within the concrete.

Abbildung 1.3: The Bonn Reference Wall.

The overreaching goal is to fully describe the uncertainty of a point cloud of an object, for example, the Bonn Reference Wall. Several challenges occur to reach the goal, tackled one after another within this thesis. For example, while scanning the wall with a terrestrial laser scanner with ten meters orthogonal distance and the scanner placed in the middle of the wall, the following scan configurations occur: Fig. 1.4 depicts the changing intensity, i.e., the strength of the backscattered signal (top), the changing incidence angle α of 0° to 60°, i.e., the angle between the surface normal and line-of-sight (middle), and the changing distance of 10 m to 25 m (bottom).

As will be elaborated in Sec. 3.4, all three parameters have a high impact on the error budget of the point cloud, especially since the changing scanning geometry leads to different uncertainties and correlated

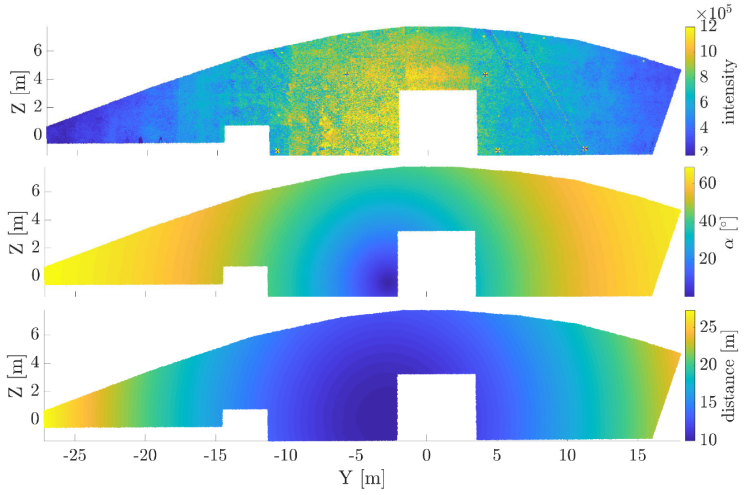

Abbildung 1.4: Varying intensity (top), incidence angle (middle), and range (bottom) of a scan acquired of the Bonn Reference Wall.

measurements. Therefore, to achieve the goal of better describing the uncertainty of a point cloud, e.g., of the Bonn Reference Wall, this thesis addresses the following subtopics:

1. **Surface-dependent range precision** – As especially the surface properties of the object and the scanning configuration impact the precision of the rangefinder [Wujanz et al., 2017], a measurement setup is presented to derive the range precision of each measurement, which solely depends on the intensity value (Publication A [Schmitz et al., 2019]).

2. **Resolution capability and the effective number of measurements** – The dense spatial acquisition of 3D points leads to overlapping neighbored laser spots, which are not infinitesimally small. Thus, neighbored measurements cannot be treated as individual, independent observations, but correlations between adjacent points exist. They lead to a smoothing of the point cloud and the reduction of details, which can, for example, be observed at the tire tracks of the wall. This smoothing effect is quantified for different scanners by the resolution capability, which also provides information about the effective number of measurements that quantifies the number of uncorrelated points in the point cloud (Publications B and C [Schmitz et al., 2020, 2021a]).

3. **Empirical determination of short-scale correlations** – The previously mentioned correlations caused by the interaction between the laser beam and the object's surface are also determined empirically without the necessity of the resolution capability but with the use of a reference geometry (Publication D [Schmitz et al., 2021c]).

4. **Establishment of a test field to analyze long-scale correlations** – The investigation of the stochastic properties requires the separation of the deterministic and the stochastic part of the point cloud. While this is a viable claim for smaller objects (up to four square meters) by knowing the geometry of the object very well or by acquiring the object's geometry with a sensor of superior accuracy, this is not easily transferable to larger objects of several meters in width and height due to the varying scan geometry (Fig. 1.4) and possible deformations of the object. Hence, a methodology is proposed to generate a very accurate geometry of the test object, which represents the deterministic part of the point cloud. Subtracting this geometry from the point cloud allows for the analysis of the stochastic part (Publications E, F, and G [Schmitz et al., 2021b; Jost et al., 2023a,b]).

Sec. 2.2 will set these goals in the scientific context and outlines open questions that will be addressed by following these objectives. By addressing these subjects, this thesis contributes to developing an enhanced

understanding of the uncertainty of TLS. Furthermore, it further gains knowledge on the resolution capability of TLS and also provides strategies to analyze the uncertainty of larger objects.

This thesis is structured as follows: Chap. 2 places this thesis in its scientific context. A brief overview of the theoretical background is given in Chap. 3. The content of the contributing publications is summarized in Chap. 4, and their most important results are presented in Chap. 5. Chap. 6 provides further considerations on the topic that may be part of future research. Finally, a conclusion is given in Chap. 7.

2. Scientific Context

Due to the fast and dense acquisition of TLS data with up to two million points per second [Leica Geosystems, 2018] and point distances of less than a millimeter at distances of ten meters [Leica Geosystems, 2017; Zoller + Fröhlich, 2018], new opportunities are opened. For example, deformation analysis is one of the main tasks in engineering geodesy [Kuhlmann et al., 2014]. By measuring signalized points in two epochs, building coordinate differences, and setting these in relation to the measurement uncertainty, it is evaluated whether an object is deformed or not [Heunecke & Welsch, 2000]. This standard procedure is carried out with point-wise measuring systems, such as total stations, leveling, or global navigation satellite systems (GNSS). Since these instruments have been studied for decades, their stochastic properties can be trustfully determined to perform congruence testing.

Furthermore, as the error sources of the previously named instruments are well studied and known in detail, it is possible to propagate the accuracy of the final result. Otherwise, multiple single-point measurements are carried out, and an empirical accuracy is derived for the measurement. Thus, detailed knowledge of the error budget or the possibility of repeatable measurements is mandatory.

TLS cannot fulfill these requirements. On the one hand, performing repeatable measurements of a point to derive an empirical standard deviation is impossible since a point cannot be specifically targeted [Holst & Kuhlmann, 2016]. On the other hand, the massive variety of errors coming from the scanner itself, the interaction of laser and object, the environment, and the scan strategy [Cosarca et al., 2009] can hardly be quantified and propagated further, although promising approaches for a part of errors have been established [Kauker & Schwieger, 2017; Kerekes & Schwieger, 2020].

The enhanced technical processing of TLS compared to older geodetic instruments more and more leads to the feeling of TLS as a black box as the pre-processing of the raw observations and the error sources are not made accessible to the users [Walser & Gordon, 2013]. Furthermore, as a reflectorless measuring system, the emitted laser beam interacts with the surface and is, therefore, strongly dependent on the surface properties [Gordon, 2008]. Since surfaces have many variations of materials, roughness, and colors, simple modeling is impossible. Thus, it is hard to functionally model the systematic errors, especially those related to the object surface. This is the main difference to point-wise measuring systems: the functional relation of the errors is only limitedly known, and many systematic errors occur that cannot be modeled.

Section 2.1 reviews approaches and methods already published to determine the stochastic properties of laser scanners. This thesis will address the open points outlined in Sec. 2.2.

2.1 State of the Art

Since the systematic errors can only be reduced to a certain limit (see more in Sec. 3.4), the remaining systematic errors correlate the measurements as they affect points that are spatially close to each other in a partially similar way [Holst & Kuhlmann, 2016]. Thus, TLS data are highly correlated. Neglecting these correlations in the stochastic model leads to biases in the estimation or the judgment of deformations, which is proven by many studies, e.g., [Holst et al., 2014; Jurek et al., 2017; Kermarrec et al., 2019; Harmening & Neuner, 2020; Zhao et al., 2019]. This demonstrates the relevance of determining the stochastic properties of TLS measurements to integrate them into the stochastic model, which the VCM represents, or to identify an alternative realistic stochastic measure such as the effective number of measurements [Holst & Kuhlmann, 2016], which quantifies the number of uncorrelated points in the scan [Bartels, 1935].

To quantify the uncertainty of TLS a VCM $\mathbf{\Sigma}_{ll}$ can be established that represents the stochastic properties variances σ_i^2 and covariances σ_{ij} (see more in Sec. 3.1) for the TLS observation types range r, horizontal angle φ, and vertical angle θ:

$$\boldsymbol{\Sigma}_{ll} = \begin{bmatrix} \overbrace{\begin{bmatrix} \sigma_{r_1}^2 & \sigma_{\varphi_1 r_1} & \sigma_{\theta_1 r_1} \\ \sigma_{r_1\varphi_1} & \sigma_{\varphi_1}^2 & \sigma_{\theta_1\varphi_1} \\ \sigma_{r_1\theta_1} & \sigma_{\varphi_1\theta_1} & \sigma_{\theta_1}^2 \end{bmatrix}}^{\boldsymbol{\Sigma}_{1,1}} & \cdots & \overbrace{\begin{bmatrix} \sigma_{r_n r_1} & \sigma_{\varphi_n r_1} & \sigma_{\theta_n r_1} \\ \sigma_{r_n\varphi_1} & \sigma_{\varphi_n\varphi_1} & \sigma_{\theta_n\varphi_1} \\ \sigma_{r_n\theta_1} & \sigma_{\varphi_n\theta_1} & \sigma_{\theta_n\theta_1} \end{bmatrix}}^{\boldsymbol{\Sigma}_{n,1}} \\ \vdots & \ddots & \vdots \\ \underbrace{\begin{bmatrix} \sigma_{r_1 r_n} & \sigma_{\varphi_1 r_n} & \sigma_{\theta_1 r_n} \\ \sigma_{r_1\varphi_n} & \sigma_{\varphi_1\varphi_n} & \sigma_{\theta_1\varphi_n} \\ \sigma_{r_1\theta_n} & \sigma_{\varphi_1\theta_n} & \sigma_{\theta_1\theta_n} \end{bmatrix}}_{\boldsymbol{\Sigma}_{1,n}} & \cdots & \underbrace{\begin{bmatrix} \sigma_{r_n}^2 & \sigma_{\varphi_n r_n} & \sigma_{\theta_n r_n} \\ \sigma_{r_n\varphi_n} & \sigma_{\varphi_n}^2 & \sigma_{\theta_n\varphi_n} \\ \sigma_{r_n\theta_n} & \sigma_{\varphi_n\theta_n} & \sigma_{\theta_n}^2 \end{bmatrix}}_{\boldsymbol{\Sigma}_{n,n}} \end{bmatrix}. \tag{2.1}$$

The sub-matrices $\boldsymbol{\Sigma}_{i,i}$ describe the VCM within each 3D point i whereas $\boldsymbol{\Sigma}_{i,j}$ quantifies the covariance between two scan points i and j. The overreaching goal of research in this field is to fill all entries of $\boldsymbol{\Sigma}_{ll}$. This thesis contributes to further approach this goal. The starting point of this thesis in the context of existing studies will be elaborated in the following.

Elementary Error Model and Synthetic Covariance Matrix

The establishment of a stochastic model can be approached from two sides: forward modeling and backward modeling. The forward modeling quantifies errors and propagates them according to the variance propagation law to establish a synthetic VCM by applying the elementary error model [Schwieger, 1999]. This model says that the difference between the true value and the measured value is a sum of various elementary errors that can be subdivided into a) non-correlating, b) functional correlating, and c) stochastic correlating errors [Schwieger, 1999]:

a) Non-correlating errors only affect single measurements and do not cause any correlations. Thus, they represent the noise that can be either taken from the manufacturers' specifications or empirical investigations such as Wujanz et al. [2017]; Heinz et al. [2018]; Schmitz et al. [2019].

b) The functional model of the functional correlating errors is known, and their influence can be eliminated from the point cloud, e.g. internal scanner errors are determined in the calibration [Lichti, 2007; Reshetyuk, 2010; Holst et al., 2016a; Medić, 2021]. They are determined with a certain precision that needs to be integrated into the stochastic model.

c) The stochastic correlation errors cause physical correlations between the measurements due to the measuring process. Their functional model and magnitude are mostly not well known and, therefore, hard to model. Examples are overlapping laser spots, the influence of the scanning geometry, or variations in the atmosphere.

Kauker & Schwieger [2017] and Kerekes & Schwieger [2020] show the success of applying the elementary error model to TLS, which is included in surface parameterizations by Raschhofer et al. [2021]. However, this strategy needs to quantify all influencing errors, which already works for the instrumental and atmospheric errors [Kerekes & Schwieger, 2020, 2021], but the integration of the influence of the object surface paired with the scanning geometry is still missing so far. The existence of errors resulting from the reflecting properties of the target [Zámečníková et al., 2014; Lambertus et al., 2018] and the scanning geometry [Soudarissanane et al., 2011; Zámečníková & Neuner, 2018; Linzer et al., 2021; Linzer & Neuner, 2022] is proven, but, so far, a modeling strategy does not yet exist due to the variability of both influencing error sources [Muralikrishnan, 2021]. Thus, the interaction of the laser beam with the surrounding and the scanning geometry cannot be modeled forwardly and lead to unsolved questions. For this reason, this thesis approaches more empirical strategies.

Empirical Assessment of Laser Scanning Uncertainty

The stochastic properties can be modeled backwards to avoid making assumptions about the error sources. Therefore, the stochastic and the deterministic part of the point cloud must be separated to analyze the stochastic part. Many studies on laser scanner uncertainty focused on the noise of the instrument by using known geometric structures and investigating the residuals of these structures, such as planes [Boehler et al., 2003; Soudarissanane et al., 2011; Wunderlich et al., 2013; Lambertus et al., 2018], or spheres [Heister, 2006; Wunderlich et al., 2013; Lindstaedt et al., 2012]. Other studies acquired the surface with a sensor of superior accuracy, such as a laser tracker + T-Scan [Linzer et al., 2021], a measurement arm [Holst et al., 2017a], or structured light scanners [Gordon, 2008; Wujanz et al., 2017] as a commonly used strategy is to compare the instrument to be evaluated against a reference instrument [Muralikrishnan, 2021]. This leads to the opportunity to analyze the uncertainty of TLS in terms of the scanner's precision depending on different parameters such as object color [Kersten et al., 2005b; Clark & Robson, 2004; Voegtle et al., 2008], material [Lichti & Harvey, 2002; Lee et al., 2010; Wujanz et al., 2017], or reflectivity [Pfeifer et al., 2007; Lambertus et al., 2018].

Most studies focus on the residuals to a reference to quantify the scanner's uncertainty, which is primarily related to random and systematic range errors if the incidence angle is low. The angular precision, however, is mainly taken from the manufacturer's specifications [Holst & Kuhlmann, 2016] as the angular measurement is only related to the scanner's internal processes and not to the interaction with the object. First approaches for determining the angular precision and temporal correlations between angular measurements are presented in Kermarrec & Lösler [2021] and Kermarrec & Hartmann [2021].

Other geodetic disciplines widely explored the field of spatial statistics in the context of least squares collocation, Kriging, spatial covariance modeling, etc., e.g., Moritz [1972]; Cressie [1986, 1993]; Sherman [2011]. However, the transfer to TLS data is still missing. While the integration of correlations into GNSS is a common procedure [Kuhlmann, 2001; Kermarrec & Schön, 2016], the quantification of correlations is not straightforward and hard to accomplish [Holst & Kuhlmann, 2016] due to the numerous different error sources in TLS measurements (see Sec. 3.4).

The result of a laser scan is a 3D point cloud with Cartesian coordinates derived from polar observations. During the calculation of the Cartesian coordinates, correlations between the single coordinates are introduced that can be derived by variance propagation and that need to be considered while working with Cartesian coordinates [Kermarrec et al., 2019]. First investigations on temporal correlations were carried out by Koch [2008] and Koch et al. [2010], who considered the observations as multiple measurements after scanning an object multiple times and treated them as a time series to derive an auto-covariance matrix. The high temporally frequent sampling of data points leads to temporal correlations between the measurements, which are further investigated in Kermarrec et al. [2020]; Kermarrec & Lösler [2021]; Kermarrec et al. [2021]. Both correlation types will not be the focus of this thesis as only polar observations are considered, and spatially close points are usually measured within a short period. That is why herein, the focus is on spatial correlations.

The integration of spatial correlations is targeted with the previously introduced synthetic VCM based on the elementary error, which is still leaking some effects. Thus, this thesis will focus on the empirical determination of spatial correlations as Jurek et al. [2017] prove their relevance.

Resolution Capability

The very dense acquisition of data leads to neighboring laser spots overlapping. On the one hand, this smoothes the measured surface [Bitenc et al., 2019], and on the other hand, spatially adjacent points are correlated [Kern, 2003] (see more in Sec. 3.3). Thus, the scanner resolution cannot be set equal to the resolution capability as scanners have such a high frequent acquisition [Lichti & Jamtsho, 2006]. The measured points do not deliver individual information on the object and are, therefore, correlated. So far, this effect is not considered in the VCM. Different studies present approaches to investigate the edge behavior [Wunderlich

et al., 2013] and to derive the resolution capability [Boehler et al., 2003; Lichti, 2004; Lichti & Jamtsho, 2006; Centeno et al., 2010; Huxhagen et al., 2011; Pesci & Teza, 2008]. However, nobody has put that into the context of correlated measurements so far. For this reason, Publications B and C develop a more enhanced approach to derive the resolution capability empirically, and they demonstrate a procedure to integrate resulting correlations into the VCM. The empirical results can be confirmed by Chaudhry et al. [2021], who proposed a modeling approach for the resolution capability without needing empirical data.

2.2 Open Questions

The establishment of a synthetic VCM by applying the elementary error model is still leaking the influence of the scanning geometry and the object surface properties [Kerekes & Schwieger, 2020], which strongly affects the TLS rangefinder's uncertainty [Zámečníková et al., 2014; Zámečníková & Neuner, 2018; Linzer et al., 2021; Linzer & Neuner, 2022]. Moreover, even those errors that can be calibrated partially underlie temporal changes, as shown in Medić et al. [2021], who demonstrated the temporal instability of calibration parameters. Thus, remaining influences exist that cause errors in the point cloud but that cannot be calibrated. So far, the main focus in the empirical uncertainty analysis of TLS lies in determining the scanner's precision using residuals from a known object. The empirical determination of correlations was not in focus besides the forward modeling of the VCM and the determination of temporal correlations.

This thesis focuses on determining stochastic properties such as range variances, short-scale correlations induced by the object and laser beam interaction, and on long-scale correlations from remaining systematic errors and atmospheric effects that cannot be calibrated. To analyze the remaining error budget, new research topics need to be addressed that summarized in the following questions:

A) **To which extent can the combined influence of the object surface and scanning geometry on the stochastic properties be integrated into the stochastic model considering the precision and correlations?**
This question will be addressed in goal 1 (determination of the surface-dependent range precision), goal 2 (determination of the resolution capability), and goal 3 (empirical determination of short-scale correlations) of Sec. 1.2.

B) **Which details can be actually seen in the scan when the overlap of laser spots leads to correlated measurements that smooth contours in the point cloud?**
This question will be addressed in goal 2 (determination of the resolution capability) and goal 3 (empirical determination of short-scale correlations) of Sec. 1.2.

C) **How to derive a reference geometry to separate the deterministic and the stochastic parts of the point cloud with special focus on large objects?**
This question will be addressed in goal 3 (empirical determination of short-scale correlations) and goal 4 (establishment of a test field to analyze long-scale correlations) of Sec. 1.2.

The strategies presented in this thesis to answer the above questions do not rely on many assumptions about the error sources and do not aim at quantifying them. Instead, it is the task to quantify or reduce their combined influence in real-world scenarios.

3. Statistical and Geodetic Basics

This thesis presents strategies for empirically determining the stochastic properties of terrestrial laser scans. This section delivers the basic theoretical background to understand the content of the relevant publications. Sec. 3.1 explains the stochastic model's composition and theoretical determination. Afterwards, Sec. 3.2 addresses the principle of TLS while Sec. 3.3 further focuses on its resolution capability. To understand why errors occur in TLS measurements, Sec. 3.4 outlines the relevant error sources. Finally, Sec. 3.5 outlines the basics of deformation analyses and the relevance of the stochastic model.

3.1 Composition and Theoretical Determination of the Stochastic Model

In geodesy, as a rule, strict quality requirements are placed on the task of deriving spatial information from empirically collected data, which infers the evaluation of the measurement quantity as well as the specification of comprehensible, also interdisciplinary accepted quality characteristics [Niemeier, 2008, p. 1]. This section gives a brief insight into the stochastic description of measurements and the empirical determination of the uncertainty.

TLS measurements are considered to be the realizations

$$\mathbf{y} = \begin{bmatrix} y_1 \\ \vdots \\ y_n \end{bmatrix} \tag{3.1}$$

of random variables

$$\mathbf{Y} = \begin{bmatrix} Y(s_1) \\ \vdots \\ Y(s_n) \end{bmatrix} = \begin{bmatrix} Y_1 \\ \vdots \\ Y_n \end{bmatrix} \tag{3.2}$$

of a spatial stochastic process for any set of sample locations $\{s_i : 1, ..., n\} \subset \mathbb{R}$. The statistical variation can be decomposed into a deterministic trend term $\mu(s)$ and a stochastic residual term $\epsilon(s)$ consisting of a signal term $\gamma(s)$ and a noise term $\delta(s)$ (Fig. 3.1) [Cressie, 1993, p. 113], [Schuh, 2017, p. 75]:

$$Y(s) = \mu(s) + \underbrace{\gamma(s) + \delta(s)}_{\epsilon(s)} \quad , \quad s \in \mathbb{R}. \tag{3.3}$$

In terms of TLS, the three components are characterized as follows:

a) Deterministic trend $\mu(s)$ (black in Fig. 3.1) describes the real geometry of the object and all errors that can be eliminated knowing the deterministic function, such as internal misalignments in the scanner calibration (Sec. 3.4.1).

b) Signal $\gamma(s)$ (red in Fig. 3.1) includes all errors that cannot be modeled functionally but that are correlated and cause colored noise.

c) Noise $\delta(s)$ (blue in Fig. 3.1) contains the white noise.

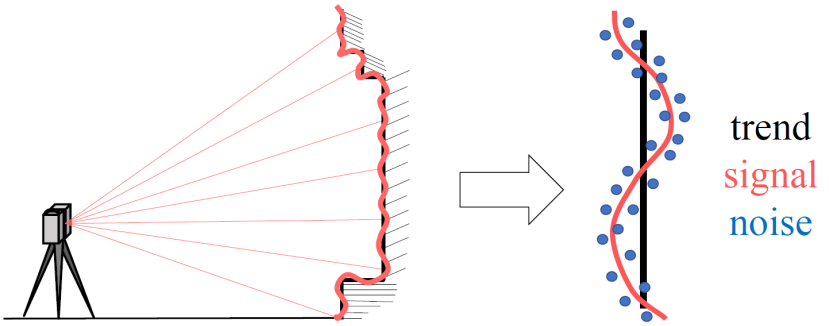

Abbildung 3.1: Composition of a TLS measurement: trend, signal, and noise.

It is important to separate the deterministic trend $\mu(s)$ from the stochastic residual term $\epsilon(s)$ to analyze the latter one, i.e., the stochastic part of the measurements. The signal term is described as colored noise, and the noise term consists of white noise. Both together are expected to be distributed around zero and thus, defined as:

$$\begin{aligned} \epsilon(s) = Y(s) - \mu(s) \Rightarrow E[\epsilon(s)] &= E[Y(s)] - \mu(s) \\ \Rightarrow E[\epsilon(s)] &= 0. \end{aligned} \tag{3.4}$$

The mean vector of $\mathbf{Y}$ is given by

$$E(\mathbf{Y}) = [E(Y_1), ...E(Y_n)]^T = [\mu_1, ..., \mu_n]^T = \mu, \tag{3.5}$$

the variance of a random variable is defined by

$$\text{var}(Y_i) = E[(Y_i - \mu_i)^2] = \sigma^2(s_i) = \sigma_i^2, \tag{3.6}$$

which describes the non-correlating errors, and the covariance of two random variables Y_i and Y_j can be denoted as

$$\text{cov}[Y_i, Y_j] = E[(Y_i - \mu_i)(Y_j - \mu_j)] = \sigma_{ij} \tag{3.7}$$

describing the covariance of two stochastic-correlated variables. This leads to the variance-covariance matrix (VCM)

$$\text{cov}(\mathbf{Y}) = \begin{bmatrix} \text{var}(Y_1) & \dots & \text{cov}(Y_1, Y_n) \\ \vdots & \ddots & \vdots \\ \text{cov}(Y_n, Y_1) & \dots & \text{var}(Y_n) \end{bmatrix} = \begin{bmatrix} \sigma_1^2 & \dots & \sigma_{1n} \\ \vdots & \ddots & \vdots \\ \sigma_{n1} & \dots & \sigma_{n^2} \end{bmatrix} = \mathbf{\Sigma} \tag{3.8}$$

given $\text{cov}(Y_i, Y_i) = \text{var}(Y_i)$ [Niemeier, 2008, p. 24 ff.]. Herein, the variances σ_i^2, i.e., the squared standard deviation, of the observations build the matrix's main diagonal. They build the sum of the variances of colored noise $\sigma_{c_i}^2 = r_c \cdot \sigma_i^2$ and white noise $\sigma_{w_i}^2 = r_w \cdot \sigma_i^2$ with r_c and r_w being the ratio of colored and white noise following $r_c + r_w = 1$ [Jurek et al., 2017]. The rest of the VCM is filled with the covariances σ_{ij}, which is composed of the correlation coefficient ρ_{ij}, which describes the stochastic dependency between the observations and the colored noise (σ_{c_i} and σ_{c_j}) of the observations i and j following [Koch, 1999, p. 97 ff.]

$$\sigma_{ij} = \rho_{ij} \cdot \sigma_{c_i} \cdot \sigma_{c_j}. \tag{3.9}$$

Thus, it is necessary to know the variances of the single observations, the ratio of colored noise, and the correlation coefficient between the observations to fully populate the VCM.

To get back to the TLS measurements and the realization $\mathbf{y}$ of the stochastic process $Y(s)$, we transfer Eq. (3.3) to

$$\mathbf{y} = \mathbf{A}\mathbf{x} + \mathbf{v} \tag{3.10}$$

with n discrete, equidistant values, $\mathbf{Ax}$ denoting the deterministic trend, and $\mathbf{v}$ defining the residuals and therefore, the stochastic signal. With this and given the definition of variances and covariances from Eqs. (3.6) and (3.7), we can derive the empirical covariance function of $\mathbf{y}$ [Cressie, 1993, p. 49], [Heunecke et al., 2013, p. 343]:

$$\hat{C}(h) = \frac{1}{n-h-1} \sum_{j=1}^{n-h} \mathbf{v}(j)\mathbf{v}(j+h) \quad \text{with} \quad h = 1, ..., m, \quad m = n/10. \tag{3.11}$$

To get the empirical correlation function, we apply [Cressie, 1993, p. 67]

$$\hat{\rho}(h) = \frac{\hat{C}(h)}{\hat{C}(0)}. \tag{3.12}$$

For the generalization and prediction of correlations, an analytical function ρ is estimated through the empirical data of $\hat{\rho}(h)$. Different kinds of correlation functions exist, but the choice of function will not be the subject of this thesis. The values from this function can be used to fill the correlation matrix

$$R = \begin{bmatrix} 1 & \rho_{12} & \rho_{13} & \dots \\ \rho_{21} & 1 & \rho_{23} & \dots \\ \rho_{31} & \rho_{32} & 1 & \dots \\ \vdots & \vdots & \vdots & \ddots \end{bmatrix}. \tag{3.13}$$

As a measure for the number of uncorrelated measurements, the effective number of measurements n_{eff} was introduced by Bartels [1935] as it implies the amount of independent information in the measurements. It is often applied to time-series, for example, in GNSS applications [Kuhlmann, 2001] and defined as [Taubenheim, 1969]:

$$n_{eff} = \frac{n}{1 + 2\sum_{h=1}^{m} \frac{n-h}{n} \rho(h)} \quad \text{with} \quad m = n/10 \tag{3.14}$$

with n describing the number of all observations, ρ describes the auto-correlation function, and h the number of intervals between two measured values. Publication B [Schmitz et al., 2020] extends this equation for spatial data to derive the effective number of measurements for 2D data as follows:

$$n_{eff_{2D}} = \frac{n}{1 + 2\sum_{h=1}^{m_x} \sum_{k=0}^{m_y} \frac{(n_x-h)}{n_x} \cdot \frac{(n_y-k)}{n_y} \rho(h,k)}. \tag{3.15}$$

The total number of points n is divided into n_x points in the horizontal direction (X-direction) and n_y points in the vertical direction (Y-direction) on the object surface so that $n_x \cdot n_y = n$ holds. A second run variable k with a second sum is inserted into Eq. (3.14). Variable h runs over all $m_x = n_x/10$ points, while k runs over all $m_y = n_y/10$ points. Hence, if the 2D autocorrelation function is known, a point cloud's effective number of measurements can be calculated. Holst & Kuhlmann [2016] suggest also deriving this term for TLS point clouds. This will be addressed in Publication B [Schmitz et al., 2020].

All the previously shown computations assume stationary and equidistant data. For stationary data, the mean and the covariances only depend on the spatial lag between two observations and not on their position [Sherman, 2011, p. 4]. That means that one VCM holds for the whole data set.

It is impossible to estimate non-stationary covariance functions naturally. However, if smaller parts are assumed to be locally stationary, the estimation is still possible [Sherman, 2011, p. 69]. Another term to be introduced is isotropy. The covariances of isotropic data only depend on the distance between the observations and not on their direction or orientation [Sherman, 2011, p. 48]. At the same time, data are called anisotropic if their covariances depend on the direction of the spatial distances [Sherman, 2011, p. 89].

Ignoring the correct anisotropy leads to the following effects [Sherman, 2011, p. 89]:

- Assuming isotropy a priori, revealing the direction-dependent correlation is impossible, so the true underlying spatial structure is not known. This could imply an insufficient understanding of the physical phenomena of the process.
- If the covariance structure is further used for prediction tasks such as Kriging, the weights and the variances are wrongly estimated.
- Assuming the wrong spatial structure induces a wrong stochastic model that impacts the parameter estimation and their accuracies.

As will be seen in Secs. 3.2 and 3.4, TLS data cannot be treated as equidistant, and due to different object surface properties and scanning configurations it mostly cannot be treated as stationary. How to tackle this will be especially topic of Publication D [Schmitz et al., 2021c].

3.2 Principle of Terrestrial Laser Scanning

Panoramic-type TLS acquire the environment by sampling the horizontal angle φ, the vertical angle θ, and the range r as a polar measuring system. A TLS has three axes: a vertical standing axis, a trunnion axis, and a collimation axis. It consists of three main elements: the angular encoders, a rotating mirror, and an electro-optical distance measurement (EDM) unit. The mirror rotates around the trunnion axis with a very high frequency and deflects the laser beam produced by the EDM in the direction of the collimation axis. This creates a vertical profile. By slowly rotating around the standing axis, the whole environment beside the area below the scanner is sampled. The result is a 3D point cloud with X-, Y-, and Z-coordinate. The scanner also provides an intensity value, representing the backscattered signal's strength. Most scanners also have an integrated camera so that each point gets a red, blue, and green value to define the color of the point [Kuhlmann & Holst, 2015, p. 4ff.].

Some scanners can measure in two faces: the scanner rotates around the standing axis by 180° while capturing the environment from 0° to 180° with the front and from 180° to 360° with the back face. The front and back faces are swapped when the scanner rotates further and measures a second time [Muralikrishnan, 2021]. As some systematic errors influence the observations in opposite directions, this can be used to quantify or reduce errors similar to total stations [Schofield & Breach, 2007, p. 167ff.]

The laser beam does not hit the object as an infinitesimally small point but is reflected as a spot with a certain area. This results from the fact that the light is diffracted as it exits the laser. Accordingly, the light is deflected outward at the edges and spreads further with increasing distance [Vosselman & Maas, 2010, p. 12f.]. In more detail, the beam first converges to a minimum diameter D_0 and is focused there. Subsequently, the signal expands. These are the characteristics of the so-called Gaussian beam [Reshetyuk, 2009]. Figure 3.2 shows the simplified concept of beam divergence. Here γ describes the angle at which the beam diverges and $D(r)$ the distance-dependent diameter of the spot that hits the object. To calculate the diameter of the beam $D(r)$ when it hits the object at a distance r, the rule of thumb is used [Reshetyuk, 2009; Vosselman & Maas, 2010]:

$$D(r) = D_0 + 2 \cdot r \cdot \tan\frac{\gamma}{2} \approx D_0 + r \cdot \gamma. \tag{3.16}$$

The angular sampling interval defines the point distance Δ between two successively recorded points taken ω and the distance r following $\Delta = \omega \cdot r$ [Lichti & Jamtsho, 2006].

The distance measurement is carried out according to the time-of-flight, phase-shift, or a mixed form, namely waveform digitizing for Leica scanners [Kuhlmann & Holst, 2015, p. 6ff.]. The received laser power P_r is theoretically described by the laser range equation introduced by Jelalian [1992]:

$$P_r = \frac{P_t D_r^2 \psi}{4r^2} \eta_{sys} \eta_{atm} \cos(\alpha). \tag{3.17}$$

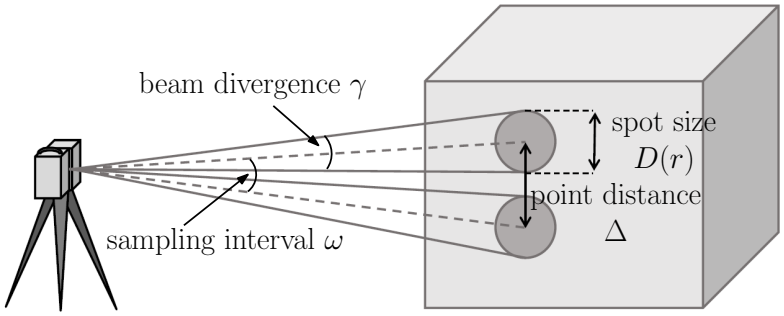

Abbildung 3.2: Impact of the beam divergence and the sampling interval on the spot size and the point distance on the object according to [Kuhlmann & Holst, 2015, p. 11].

The transmitted laser power P_t is attenuated depending on the receiver aperture diameter D_r, the range r, a system factor η_{sys}, the atmospheric transmission factor η_{atm}, the target reflectance ψ, and the incidence angle α, which denotes the angle between the surface normal and the line-of-sight. As some of the parameters are presumably constant, the received laser power mainly depends on the target's reflectance and the scanning configuration characterized by the range and incidence angle. This has a high impact on the precision of the range observation σ_r as it can be fully modeled by the received laser power P_r, also called intensity, as introduced by Wujanz et al. [2017]:

$$\sigma_r = a \cdot P_r^b + c \tag{3.18}$$

with the parameters a, b, and c.

3.3 Resolution Capability

One of the quality features that describes the performance of a TLS is the resolution capability [Wunderlich et al., 2013]. It is described as the minimum step between two measurements that can be distinguished with a probability of 95% [Kamerman, 1993]. In terms of TLS, it is separated between the resolution capability in the distance direction, which denotes the ability of the instrument to resolve two objects on the same line-of-sight [Kamerman, 1993], and the resolution capability in the angular direction, which describes the ability of a system to resolve objects on adjacent line-of-sights [Lichti & Jamtsho, 2006].

The resolution capability in distance direction mainly depends on the precision of the rangefinder. The noisier the range observations, the more complex the separation between two measurements on the same line-of-sight [Schmitz et al., 2020]. This thesis, however, focuses on the resolution capability in the angular direction, which mainly depends on the laser spot size $D(r)$ (Eq. 3.16) and the point distance Δ [Lichti & Jamtsho, 2006]. TLS are capable of sampling the environment with a very high spatial resolution of less than 1 mm @ 10 m, e.g., [Leica, 2013; Leica Geosystems, 2017; Zoller + Fröhlich, 2018]. The spot size at the front window D_0 in Eq. (3.16) has the size of at least a few millimeters (e.g., Leica ScanStation P20: 2.8 mm [Leica, 2013]; Faro Focus 3D X130: 2.25 mm [Faro, 2015]; Z+F Imager 5016: 3.5 mm [Zoller + Fröhlich, 2018]) and it expands with a longer distance according to Eq. (3.16). The range measurement is averaged over the whole spot [Lichti et al., 2005]. Thus, if a high scanner resolution is chosen, the laser spots unavoidably overlap, and neighbored laser spots partially illuminate the same surface (Fig. 3.3). This leads to the following two effects: neighbored measurements do not provide individual information on the object as they are correlated [Schmitz et al., 2020], and the object structure is smoothed due to the average over the whole laser spot [Bitenc et al., 2019]. Hence, if the laser beam hits two objects, as seen in Fig. 3.4, the measured point lies between both surfaces, and the laser scan cannot represent the sharp edge in the point cloud, but an S-shaped curve occurs.

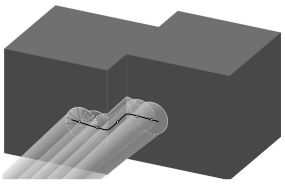

Abbildung 3.3: Overlapping laser spots on an object's edge.

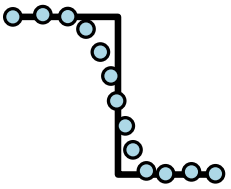

Abbildung 3.4: Schematically resulting point cloud of an edge scan.

Even if the point spacing is 1 mm, but the spot size is 1 cm, smaller objects cannot be resolved in the point cloud. For this reason, it is necessary to distinguish between the resolution defined by the point distance and the resolution capability of the scanner. Therefore, a new methodology is developed in Publication B [Schmitz et al., 2020] to determine the resolution capability and derive correlations between the points.

3.4 Error Sources of TLS Measurements

The error sources that mitigate the quality of the point cloud are illustrated in Fig. 3.5, namely scanner misalignments, the scanning geometry in combination with the object, the atmosphere, and the registration of different point clouds [Cosarca et al., 2009; Soudarissanane et al., 2011; Zogg, 2008].

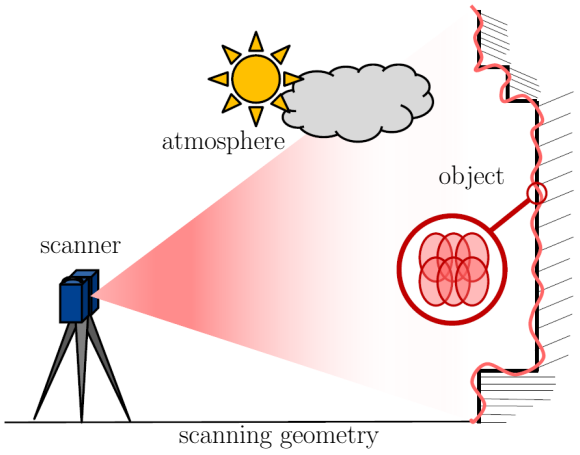

Abbildung 3.5: Error sources of terrestrial laser scans.

Internal misalignments in the scanner occur due to construction imperfections, affecting all three observation types, namely range, horizontal, and vertical angle. In addition, the scanning geometry, the interaction of the laser beam and object, and the atmosphere influence the emitted laser beam, which is part of the EDM. For this reason, the latter-mentioned error sources only influence the range measurement [Holst & Kuhlmann, 2016]. In the following, the different error sources are inspected more deeply. Sec. 3.4.1 explains the impact of internal scanner misalignments, Sec. 3.4.2 recapitulates the scanning geometry and object surface, and Sec. 3.4.3 addresses the atmospheric effects.

3.4.1 Scanner Misalignments

A scanner cannot be perfectly constructed. That is why the system always underlies physical scanner misalignments that systematically affect the observations of the scanner. They are characterized by offsets, tilts,

and eccentricities in the axis, the EDM unit, or the angular encoders [Muralikrishnan et al., 2015]. Different functional models exist to calibrate these errors for TLS. One common strategy is to base the model on the most crucial total station errors, namely, rangefinder offset, collimation, and trunnion axis errors, and vertical index offset [Abbas et al., 2014; Lichti, 2010], or more complex total station models that consider all known errors [Holst & Kuhlmann, 2014; Lichti, 2007].

The American National Institute of Standards and Technology (NIST) introduced a functional model that consists of 18 parameters that describe mechanical misalignments in the scanner [Muralikrishnan et al., 2016]. Based on these 18 parameters, Medić et al. [2020] established a user-oriented, efficient calibration field at Campus Klein-Altendorf (University of Bonn), which will be used in the further course of the thesis. Furthermore, they reduced the 18 parameters to ten relevant parameters for high-end panoramic-type scanners [Medić et al., 2017].

Even though many studies put effort into the calibration of TLS, Medić et al. [2021] demonstrated that not all calibration parameters are stable with time and temperature. Hence, it cannot be guaranteed that the calibration parameters calculated in the calibration field are still valid for the measurements in the field. One strategy to tackle this is an in-situ calibration, performed during the measurement in the field [Medić et al., 2019]. However, this is still the subject of current research and needs to be solved [Medić, 2021].

Fig. 3.6 depicts the influence of internal scanner misalignments on the point cloud to get an impression of the magnitude of errors. It compares two scans of a water dam acquired with two different instruments, namely the Leica ScanStation P50 and the Z+F Imager 5016. The colors indicate the M3C2 differences between the point clouds. Both scans were acquired within 30 minutes. Hence, the dam did not deform within this time, but both point clouds show systematic deviations in the interval of ±6 mm.

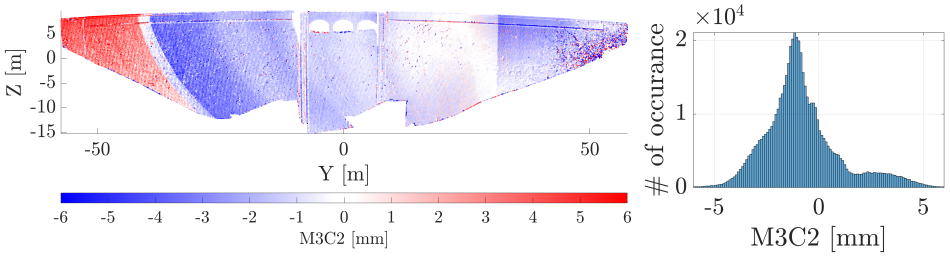

Abbildung 3.6: M3C2 differences between a scan of the Leica ScanStation P50 and the Z+F Imager 5016 that have been acquired within a short time from the same station.

After calibrating both scanners according to the description given in Medić et al. [2020], the differences are substantially reduced (Fig. 3.7), but systematic effects are still apparent in the interval of ±4 mm.

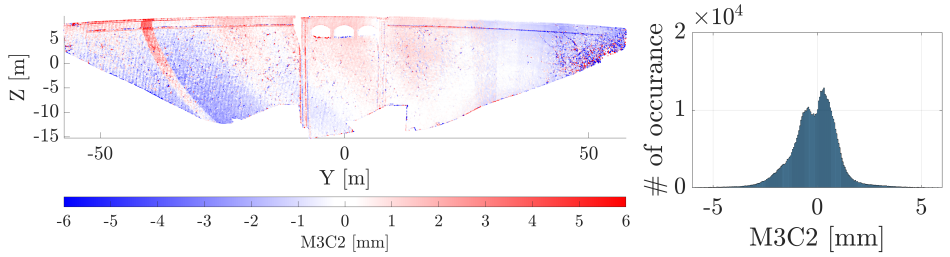

Abbildung 3.7: M3C2 differences between a scan of the Leica ScanStation P50 and the Z+F Imager 5016 that have been acquired within a short time from the same station. User calibration is applied to both scans.

Strategies to calibrate mechanical misalignments in the scanner exist, but there are still some challenges to solve to reduce all systematic errors resulting from this error source. Hence, the remaining errors still affect the point cloud. As they cannot be considered deterministically, they must be incorporated into the stochastic model.

3.4.2 Scanning Geometry and Object Surface

In contrast to the scanner misalignments, errors due to the scanning geometry, mainly characterized by the range and the incidence angle, are part of current research. However, no standardized evaluation and calibration methods exist [Muralikrishnan, 2021]. As a result, the scanning geometry causes random as well as systematic errors, and likewise does the object surface, which is characterized by the material, roughness, and color.

The impact of the scanning geometry and the object reflectivity on the range noise is well studied (e.g., [Soudarissanane et al., 2011; Voegtle & Wakaluk, 2009; Bolkas & Martinez, 2018; Boehler et al., 2003; Soudarissanane, 2016]). The noise increases with higher incidence angles, longer distances, and lower reflective surfaces. These changes in the scanning settings reduce the received intensity, as can be seen in Eq. (3.17). For this reason, changes in the scanning geometry or the object surface that affect the range precision can be fully described by the intensity as shown in Eq. (3.18). Publication A [Schmitz et al., 2019] presents a strategy to derive this function efficiently and user-oriented.

The scanning geometry and object surface also cause systematic errors in the range observations, which often exceed the magnitude of random errors [Holst & Kuhlmann, 2014; Holst et al., 2016a]: one effect is related to the reflectivity of the object, and the other effect to the incidence angle. Finally, scanning on different reflective surfaces leads to systematic offsets in the range measurement as higher reflective surfaces are measured farther away than lower reflective surfaces [Kersten et al., 2005a; Pfeifer et al., 2007; Zámečníková et al., 2014]. The latter study tries to find a physical relationship, but not all effects can be modeled. Thus, a calibration strategy is not yet valid.

Further biases in the distance measurement occur due to the incidence angle. In this context, two explanations exist – one geometric and one physical [Kern, 2003; Joeckel et al., 2008; Schäfer, 2017]: Both explanations are based on the fact that the laser beam is elongated on the surface if the incidence is higher than 0° and the signal is averaged over the whole beam to determine the range (Fig. 3.8).

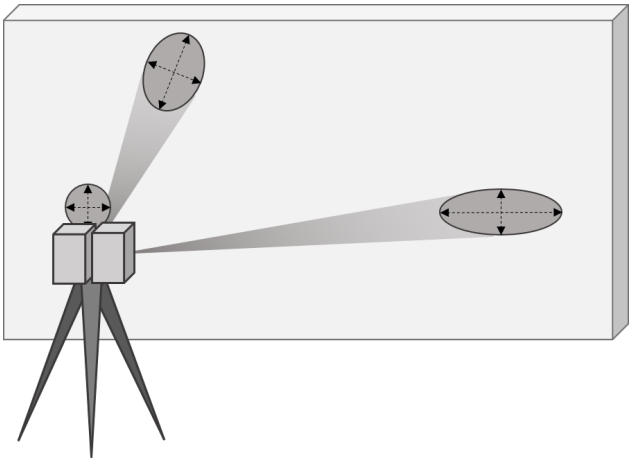

Abbildung 3.8: Elongation of the laser spot at different incidence angles.

Due to the elongation, the center of the spot does not correspond to the intersection of the collimation axis and the object. Hence, the measured horizontal and vertical angles do not correspond to the measured distance, which is too long. Another aspect is that the parts of the signal closer to the instrument have a higher impact on the distance measurement. Thus, the measured distance is too short and does not correspond to the collimation axis (Fig. 3.10). The bias becomes evident in the studies of Zámečníková & Neuner [2018], Linzer et al. [2021], and Linzer & Neuner [2022], who verified the theory that the measured distance does not correspond to the collimation axis. This distance offset is also linked to the surface reflectivity, which supports the physical explanation as the intensity distribution varies. They also provide methods to correct this offset. However, they are not yet transferable to all scanners.

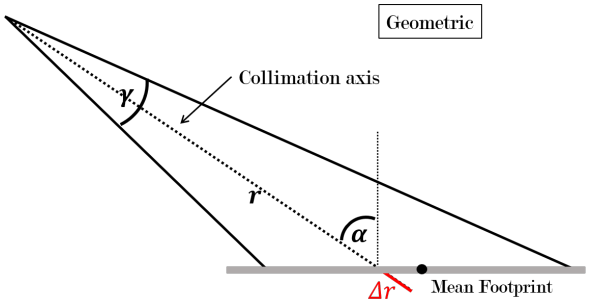

Abbildung 3.9: Impact of the elongated laser beam on the range measurements with the geometric explanation where the distance is measured too long.

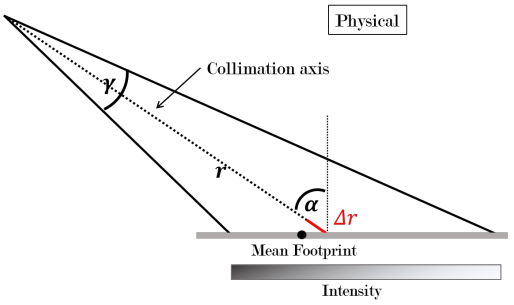

Abbildung 3.10: Impact of the elongated laser beam on the range measurements with the physical explanation where the distance is measured too short.

3.4.3 Atmospheric Effects

The atmospheric conditions have mainly two effects on the point cloud: firstly, it changes the velocity of the emitted signal, and secondly, it affects the vertical angle due to the diffraction of the laser beam [Schofield & Breach, 2007, p. 47, p. 137].

Temperature, air pressure, and air humidity influence the velocity of the laser beam [Barrell & Sears, 1939]. The current atmospheric conditions must be considered as the EDM measures the distance depending on the velocity. The impact is well studied, and approx. 1°C temperature cause 1 ppm, i.e. 1 μm/m change in the distance. The same holds for $3-4$ hPa, also causing 1 ppm distance change depending on the frequency of the laser. The influence of the humidity is negligible low [Kahmen, 2006, p. 170ff.].

Despite the influence on the range observation, the refraction affects the vertical angle. Due to different conditions in the horizontal atmospheric layers, the laser beam is diffracted vertically [Witte & Sparla, 2011, p. 245]. This leads to a bending of the laser beam, which depends on the vertical gradient of temperature and air pressure [Friedli, 2020, p. 88]. Thus, the measured vertical angle does not correspond to the position of the reflected signal, which is empirically shown in Friedli et al. [2019]. This effect can reach up to decimeters for long-range laser scanners at a distance of more than one kilometer [Friedli, 2020, p. 33]. Furthermore, the strength of the beam curvature depends on the current atmospheric conditions, which can be very variable and, thus, hard to determine correctly [Witte & Sparla, 2011, p. 291]. So far, no proper general model exists to model the temperature profile along the laser path, which limits the accuracy of the determination [Friedli, 2020, p. 86].

Both effects result in systematic errors in the point cloud. Correction formulas can partly correct the influence [Friedli, 2020]. Due to model uncertainties, the remaining effects must be considered in the stochastic model. As the atmospheric effects vary slowly, they must be integrated as long-scale correlations. The atmospheric influence increases with the magnitude of the measurement range [Kerekes & Schwieger, 2020] but also at shorter distances, these effects might occur and cannot be entirely neglected. As the existing models are not sufficient to reduce all effects, they must be incorporated into the stochastic model.

3.5 Deformation Analysis

Knowledge of the stochastic properties is essential to perform a deformation analysis as it is evaluated whether coordinate differences are related to the stochastic of the measurements or real geometry changes. As the topic of this thesis aims at progressing the area-based deformation analysis, its basic theory will be outlined in this section.

Regular monitoring of buildings is essential to observe movements and abnormal behaviors to detect damages and threats to safety at the earliest possible time to prevent hazards [Welsch & Heunecke, 2001]. This is

relevant for man-made objects such as water dams [Scaioni et al., 2018; Barzaghi et al., 2018; Alba et al., 2006], bridges [Kuhlmann & Glaser, 2002; Cosser et al., 2003; Yu et al., 2017; Lienhart et al., 2017], or tunnels [Chmelina et al., 2012; Scaioni et al., 2014; Strauss et al., 2020].

Heunecke & Welsch [2000] distinguish between four deformation models:

a) Congruence models: the state of an object is geometrically compared at different epochs without consideration of time and deformation causes.

b) Kinematic models: description of displacements with a function of time disregarding deformation causes.

c) Static models: displacements are modeled in a functional relationship between stress and strain.

d) Dynamic models: displacements are considered to be a function of load and time.

The first two models are assigned to the descriptive models, and the latter two to the cause-response models. Publication E [Schmitz et al., 2021b] uses the congruence and dynamic models.

For the congruence model, it is only essential to know whether geometric objects, represented by points or surfaces, are moving. The causes for deformation are not of interest, but it is evaluated whether coordinate differences between two epochs are related to geometric changes or just due to uncertainties in the measurement process. Therefore, it is inevitable to have a correct description of the uncertainty of the measurements represented by a VCM. The differences $\mathbf{d}$ between coordinates of identical points or surface representations of different epochs are tested using the congruence test [Heunecke et al., 2013]:

$$T = \frac{\mathbf{d}^T \boldsymbol{\Sigma}_{dd}^{-1} \mathbf{d}}{f} \sim F_{f,\infty,1-\alpha} \tag{3.19}$$

where $\boldsymbol{\Sigma}_{dd}$ represents the VCM of $\mathbf{d}$, which is composed of the summed covariance matrices of the single epochs that also include the measurement uncertainty of the single observations represented by the VCM $\boldsymbol{\Sigma}_{ll}$ and – depending on the sensor and surface representation – also the calibration uncertainty, uncertainty of the geodetic datum, and surface approximation uncertainty. The test value T follows a Fisher distribution with f and ∞ degrees of freedom and the significance level α. Eq. (3.19) demonstrates the importance of the VCM as it is necessary to decide whether a deformation happened.

To analyze stochastic properties of measurements, the deterministic trend is separated from the stochastic part. However, measurement objects can be affected by outer conditions, such as temperature or humidity, that lead to geometric deformations. The ability to predict deformations can be useful to avoid misinterpreting those as the uncertainty of the measurement sensor. Therefore, dynamic deformation modeling can be used, which is subdivided into three different steps: measurements, modeling, and evaluation. Measurements include the determination of the deterministic quantities as well as the displacements. Hence, data of input U_t and output g_t quantities are collected. The second step deals with the modeling of system input and system reaction. A functional relation

$$g(t) = \varphi(g_{t-\tau}, U_t) \tag{3.20}$$

needs to be established that depends on an initial state of the system $g_{t-\tau}$ at a certain time $t - \tau$ and influencing input quantities U_t to estimate the state of the system $g(t)$ at time t. The third step is the evaluation of the model, where the deviation between computed and measured system reaction is determined to judge the model's performance [Welsch & Heunecke, 2001]. This allows for the description of the temporal course of the deformation as well as the prediction of the deformation.

In Publication E [Schmitz et al., 2021b], the displacements of the Bonn Reference Wall (Fig. 1.3) should be modeled so that the movement can be predicted for further measurements. This is necessary if laser scans should be corrected by the movement with a certain model to create a reference and to separate the deterministic and stochastic parts of the point cloud. The congruence model is needed to check the stability of the reference frame, and the dynamic deformation model is used to model and predict the movement of the wall not to interpret deformations as uncertainties of the scanning process.

4. Content of the Relevant Publications

The content of the relevant publications of this thesis is summarized in Fig. 4.1.

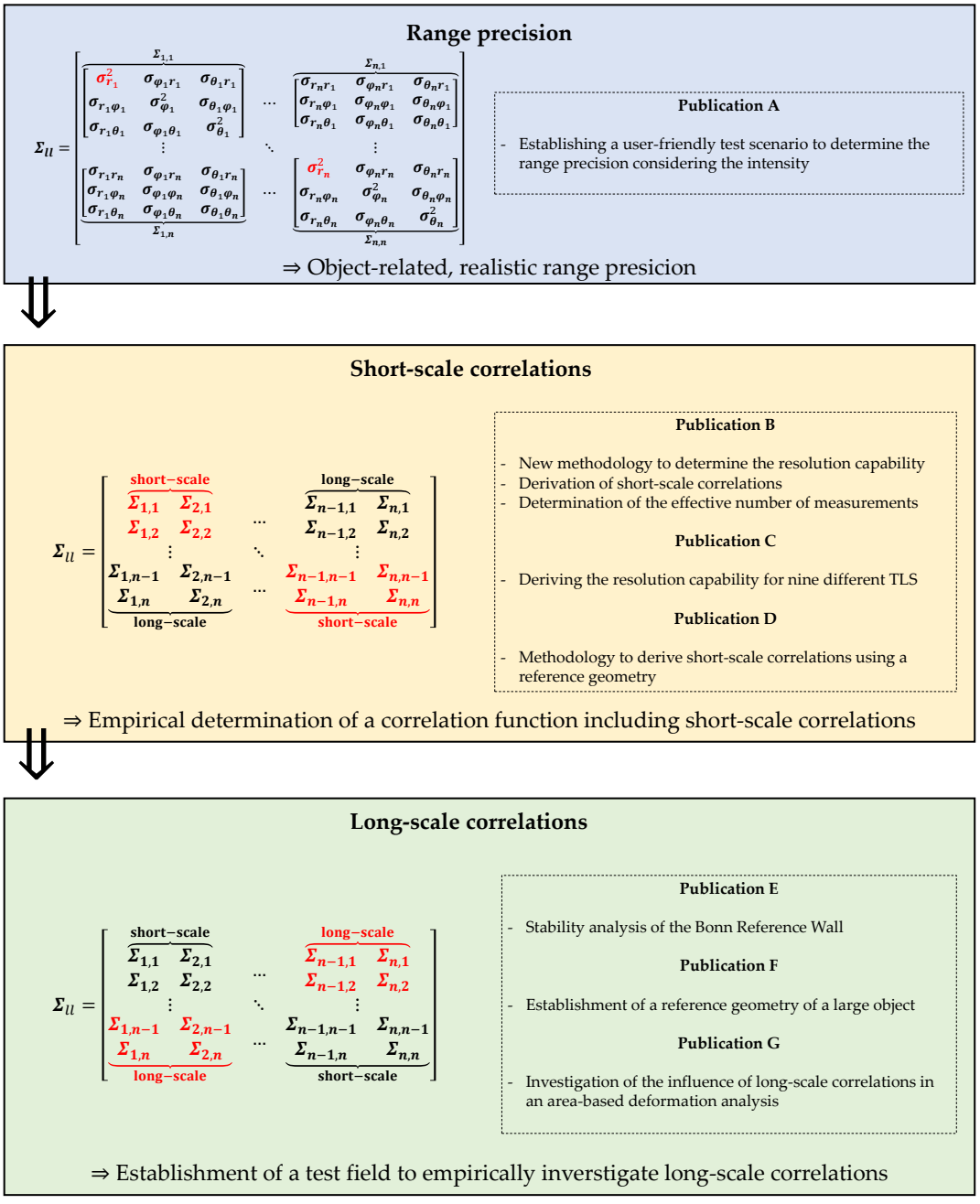

Abbildung 4.1: Summary of the content of the relevant publications contributing to this thesis.

It is subdivided into three major topics indicated by the three colored boxes that contribute to the determination of the stochastic properties that can be used in future research to establish a fully populated VCM of a terrestrial laser scan (Eq. 2.1). The parts where the presented methods contribute to the research getting closer to the goal of filling these entries are marked in red. The single publications are assigned to the corresponding boxes, and their major contributions are summarized in this chapter.

The blue box shows Eq. (2.1) and highlights the entries of the range variances, which will be addressed in Sec. 4.1. The yellow and green boxes show respectively the submatrices $\mathbf{\Sigma}_{i,i}$ of the 3D points and the covariance matrices $\mathbf{\Sigma}_{i,j}$ of two scan points. It is assumed that points with the indices 1 and 2 are close to each other as well as the indices $n-1$ and n. Correlations between those points are referred to as short-scale correlations, which are the topic of the yellow box and will be addressed in Sec. 4.2. In contrast, points with indices 1 and n are farther apart. Correlations between them are referred to as long-scale correlations and the topic of Sec. 4.3.

4.1 Empirical Determination of the Range Precision

In contrast to the precision of the angular measurements, the rangefinder observations are influenced by outer effects such as the atmosphere, the interaction with the object, and the scanning configuration as mentioned in Sec. 3.4. For this reason, the range precision is much more variable as it depends on the distance, the incidence angle, and the object's reflectance. All these effects can be modeled by the backscattered intensity (Eq. 3.18), which is necessary to fill the main diagonal of the VCM with the variances of the ranges as demonstrated in Wujanz et al. [2017]. Thus, it is necessary to develop a user-friendly setup to determine the range precision of the scanner, which will be shown in Publication A [Schmitz et al., 2019].

Publication A (Peer-Review, Journal)

- Schmitz, B., Holst, C., Medic, T., Lichti, D. D., & Kuhlmann, H. (2019). How to Efficiently Determine the Range Precision of 3D Terrestrial Laser Scanners. *Sensors*, 19(6), 1466. `https://doi.org/10.3390/s19061466`

This publication addresses the efficient empirical determination of the rangefinder's precision, and it evolves the approach of Wujanz et al. [2017] to obtain the intensity-based range precision of panoramic-type TLS with an easy and cheap experiment, which makes the approach feasible for qualified users to replicate it. So far, the determination relied on either 1D or 2D measurements [Wujanz et al., 2017; Heinz et al., 2018], which are impossible to obtain for every scanner, or quasi-ranges were used that were yielded from orthogonal aligned special reflecting targets [Wujanz et al., 2018]. All existing approaches need the raw intensity values, which are not always provided by the manufacturer (Eq. 3.18).

For this reason, this study focuses on the easy and quick setup of a test environment to derive the range precision directly from the 3D point cloud without the necessity of 1D or 2D data or orthogonally aligned test targets. Furthermore, it introduces the possibility of using scaled intensity values provided by the manufacturer. The two main aspects are addressed within the publication:

- To get a cost-efficient measurement setup, it is necessary to use higher incidence angles to get a larger variety of intensity values as no special reflecting targets, but paper boards are used. Considering the single observation groups in the plane adjustment and not weighing them equally, the standard deviation of the range measurements can be obtained from the adjustment. Hence, paper boards with different gray scales are affixed to a magnetic wall and scanned from several distances and incidence angles. This allows for a much quicker determination of the intensity function and a cost- and time-efficient installation of the test environment.

- To evaluate whether the function can also be established for scanners that do not provide raw intensity values, the scaled intensity-based and the raw intensity-based functions are compared for one scanner which provides both kinds. The investigation shows that both functions determine the same range precision. However, intensity values can be manipulated, for example, by enhancing the intensity with the distance. If this is the case, the function is not valid anymore, but it can be established for different distance classes.

In conclusion, the intensity-based range precision is estimated from an easy setup, as it is also possible to use measurements collected with a higher incidence angle. This simplifies the acquisition of a large variety of intensity values, which allows for a quicker determination of the function. Furthermore, a restricted possibility exists to determine the intensity-based range precision for scaled intensity values. The results of this publication will be elaborated in detail in Sec. 5.1.

4.2 Determination of Short-Scale Correlations

One of the primary error sources that cannot be reduced by calibration is the object surface and its interaction with the laser beam (Sec. 3.4). As pointed out in Sec. 3.2, the laser spot that hits the object is not infinitesimally small and neighbored laser spots overlap when the point distance is small. Hence, it is assumed that correlations between neighbored points exist as they partially illuminate the same object's surface. The following publications determine the resulting short-scale correlations using two different approaches. Publications B and C [Schmitz et al., 2020, 2021a] derive the correlation from the resolution capability of the point cloud. In contrast, Publication D [Schmitz et al., 2021c] determines the correlation by building the difference between the point cloud and a reference geometry.

Publication B (Peer-Review, Journal)

- Schmitz, B., Kuhlmann, H., & Holst, C. (2020). Investigating the resolution capability of terrestrial laser scanners and its impact on the effective number of measurements. *ISPRS Journal of Photogrammetry and Remote Sensing*, 159, 41–52. `https://doi.org/10.1016/j.isprsjprs.2019.11.002`

This publication develops a new methodology to determine the spatial expansion of the resolution capability in an angular direction, which is a measure of the minimum object's size that can be resolved in the point cloud, and it develops a strategy to integrate correlations due to the object surface into the VCM. Furthermore, it is evaluated how many points contribute to individual information by estimating the effective number of measurements (Sec. 3.1).

The new methodology allows for the separation of the resolution capability in different angular directions, the determination up to a distance of 80 m, and the evaluation continuously in space without making any assumptions about the laser beam shape. The proposed methodology uses the so-called Böhler Star. This is a test specimen of 1.25 m x 1.25 m size, which has two parallel aluminum planes that have a distance of 0.25 m. The foreground plane has recesses with an opening angle of 15° seen from the center. The methodology determines the width of the transition areas between the fore- and background planes, where the points cannot be assigned to one of the planes since the spot hits both planes (Figs. 3.3 and 3.4). The resolution capability is determined for different angular directions, so the expansion in different directions is quantified differently. It is determined for the Leica ScanStation P20 and the Z+F Imager 5016 for different resolutions, distances, and quality levels. It is demonstrated that the resolution capability has a linear increase with the distance and increases with a lower resolution. Furthermore, the spatial expansion is different since both scanners can better resolve objects in the horizontal than in the vertical direction. Hence, the resolution capability can be approximated by an ellipse whose area describes the minimum size of objects that can be resolved in the point cloud.

The estimated resolution capability is used to determine the correlation between neighboring points, assuming that points with a smaller point spacing than the resolution capability are correlated. Therefore, each point gets an ellipse marking the area where a smaller object cannot be resolved. All points that lie within one ellipse are assumed to be correlated. As stated in Sec. 2, the correlating impact of the object surface is not yet modelable. To determine the magnitude of the correlation resulting from the interaction between laser beam and object surface, the percentage of overlap between points is calculated and incorporated as the correlation into the VCM (Sec. 5.2).

The resulting correlation matrix is used to quantify the effective number of measurements (Eq. 3.14), which specifies how many points provide individual information on the object. It is demonstrated that the closer the points are together, the smaller the ratio between the effective number of measurements and the actual number of points in the point cloud. For example, scanning with the highest resolution of 0.8mm @ 10m at a distance of 40 m with the Leica ScanStation P20, only 7.3% of the measured points are uncorrelated. This shows that scanning with a high resolution does not necessarily increase the level of detail of the point cloud.

Publication C (Peer-Review, Conference)

- Schmitz, B., Coopmann, D., Kuhlmann, H., & Holst, C. (2021a). Using the Resolution Capability and the Effective Number of Measurements to Select the Right Terrestrial Laser Scanner. In *Contributions to International Conferences on Engineering Surveying, INGEO & SIG 2020, Dubrovnik, Croatia. Springer Proceedings in Earth and Environmental Sciences* (pp. 85–97).: Springer, Cham

While the methodology to determine the resolution capability is the focus of Publication B [Schmitz et al., 2020], this publication extends the empirical investigations by determining the resolution capability of nine scanners in total: Leica ScanStation P40, Leica RTC360, Leica Nova MS60, Faro Focus 3D X130, Leica BLK360, Leica HDS6100, Leica ScanStation P50, Leica ScanStation P20, and Zoller + Fröhlich Imager 5016. All scanners' resolution capability is determined at four different distances (10 m, 20 m, 30 m, and 40 m). For comparability reasons, almost the same settings are used with 3.1 mm @ 10 m and the lowest quality level, and the best achievable settings, i.e., highest resolution and highest quality level, are used. The results are presented in Sec. 5.2.

It is demonstrated that the shapes of the resulting ellipses vary between different scanner types. However, scanners having the same rangefinder technology, such as Leica ScanStation P40 and Leica ScanStation P50, provide similar results. For some scanners, the resolution capability has an elliptical expansion with a higher excess in the vertical direction, and others expand circularly. However, all scanners show a linear increase of the resolution capability with the distance, allowing for interpolating between the measured distances.

Using the highest resolution does not necessarily lead to a better resolution capability, as some scanners provide almost similar results using a point distance of 3.1mm @ 10m or 0.8mm @ 10m. Furthermore, the point cloud does not contain more object details due to the overlapping laser spots and correlated measurements. Hence, this investigation shows that using a lower resolution in the scanner settings can save time and reduce the amount of data without losing any details.

Using the resolution capability of the different scanners allows for the judgment of which scanner can provide the most information, which is the Leica MS60 in this case. Hence, it is not always necessary to scan with the highest possible resolution since the spot size smooths out details so far that a lower resolution provides the same amount of details in the point cloud but with less time and storage effort. This can make the data acquisition much more economic.

Publication D (Peer-Review, Journal)

- Schmitz, B., Kuhlmann, H., & Holst, C. (2021c). Towards the empirical determination of correlations in terrestrial laser scanner range observations and the comparison of the correlation structure of different scanners. *ISPRS Journal of Photogrammetry and Remote Sensing*, 182, 228–241. `https://doi.org/10.1016/j.isprsjprs.2021.10.012`

The previous publications determine short-scale correlations using the resolution capability obtained with a particular test specimen. Contrary, Publication D [Schmitz et al., 2021c] uses a reference geometry to analyze the stochastic part of the point cloud and determine correlations. This study develops two strategies to empirically determine the short-scale correlations in TLS measurements. Both methods are verified with simulated data and then applied to real data sets collected from a wooden wall. This study further states problems that occur when a larger object is scanned, as the correlation structure depends on the scanning configurations and the object's reflectivity. Hence, it proposes a strategy to apply the previously mentioned methods to larger objects.

The proposed methods rely on the fact that the trend of the point cloud must be reduced to analyze the stochastic part of the point cloud. Therefore, the test object is acquired with a laser tracker, which has superior accuracy to a TLS. Afterwards, the residuals between the reference geometry and the point cloud are analyzed. The first method (1D method) splits the point cloud into rows and columns so that the correlation in different directions is estimated separately, which allows for the determination of anisotropic correlations. The second (SF) method efficiently estimates the 2D correlation function by transforming the data into the spatial frequency domain. Thus, both methods are capable of estimating direction-dependent 2D correlation functions. Furthermore, with the use of simulated data, it is demonstrated that both methods can reproduce the initially simulated parameters.

Both methods are applied to real data from the Leica ScanStation P50, Z+F Imager 5016, Faro Focus 3D X130, and Leica BLK 360. It is demonstrated that spatial correlations with correlation lengths in the magnitude of millimeters to centimeters exist and that they are different for all scanners. Additionally, both methods obtain similar results within the expected uncertainty, and correlation functions are obtained for all scanners at two different distances. The results also correspond to Publication C [Schmitz et al., 2021a]. A summary of the results is given in Sec. 5.3.

The further course of the paper investigates the influence of a changing scanning geometry, such as range, incidence angle, and reflectivity of the surface. It is demonstrated that all three factors influence the stochastic behavior of the point cloud, which is relevant when the scanning geometry changes, for example, during the scan of a larger object of several meters in width and height (Fig. 1.4). Therefore, the study suggests a pipeline for proceeding with non-stationary data. As, so far, no strategy exists to generate a reference surface of a larger object, this pipeline only represents an outlook and is not applied to real data.

4.3 Generating a Test Scenario to Investigate Long-Scale Correlations

As mentioned in the summary of Publication D [Schmitz et al., 2021c], data of larger objects is not evaluated due to the lack of a reference geometry. The following Publications E & F [Schmitz et al., 2021b; Jost et al., 2023b] aim to tackle this problem as they want to generate a test scenario to analyze point cloud uncertainties for larger objects. The Bonn Reference Wall (Fig. 1.3) serves as the test object. Before generating the reference surface, its stability must be evaluated. If the wall changes its geometry, the strategy of generating a reference needs to be reconsidered. Publication E [Schmitz et al., 2021b] investigates the deformation of the Bonn Reference Wall. Afterwards, Publication F [Jost et al., 2023b] presents a strategy to generate a test scenario for investigating TLS uncertainties for point clouds of larger objects. Finally, Publication G [Jost et al., 2023a] shows how this strategy can improve the area-based deformation analysis.

Publication E (Peer-Review, Journal)

- Schmitz, B., Kuhlmann, H., & Holst, C. (2021b). Deformation analysis of a reference wall towards the uncertainty investigation of terrestrial laser scanners. *Journal of Applied Geodesy*, 15(3), 189–206. `https://doi.org/10.1515/jag-2020-0025`

To reduce the deterministic trend from a point cloud, precise knowledge of the object's geometry is essential to avoid the misinterpretation of possible systematic errors of the instrument as geometric changes of the object. Furthermore, if the test measurement of the TLS is not carried out at the same time as the reference geometry is acquired, it must be ensured that the test object is stable. Finally, as this thesis wants to use the Bonn Reference Wall as a test object for uncertainty analysis, it is inevitable to analyze the wall for deformations.

This publication performs a deformation analysis of the Bonn Reference Wall and investigates the establishment of a deformation model to predict further wall movements. In the first step, a stable superordinate reference frame is generated. This serves as a reference to perform the deformation analysis on six different days with varying atmospheric conditions. The deformation is analyzed between the days but also within the days. Afterwards, the acting forces are identified as the current temperature and long-term and short-term temperature changes. Further influencing factors are neglected to keep the deformation model as simple as possible to make it feasible to be used within the TLS uncertainty analysis. The investigation detects that the wall moves up to 1 mm within one day and up to 7 mm between the days of measuring.

A dynamic deformation model is established to correct the movement, which models the deformation depending on the previously mentioned acting forces (Sec. 5.4). The model manages to reduce the displacements by 45% so that the remaining standard deviation of the residuals after modeling is 0.61 mm. Compared to the results yielded in Publication A [Schmitz et al., 2019], which shows that the scanner precision can be around 0.4 mm, the achieved value is comparably high. For this reason, a second deformation model is developed, which models the deformation within one day with respect to the initial geometry of the day that needs to be acquired with a total station. This model achieves a standard deviation of 0.16 mm with 89% of the residuals lying in the interval of ± 0.25 mm, which is better than the TLS precision.

The primary outcome of this publication is that the wall changes its geometry with a magnitude that is not negligible for the uncertainty analysis of TLS. It further provides a strategy for how to consider this deformation. However, to avoid the risk of misinterpreting potential geometry changes as uncertainties of the scanner, the study suggests producing a reference geometry on the same day of testing and measuring on a cloudy day with a low temperature gradient. How this can be realized will be the subject of Publication F [Jost et al., 2023b].

Publication F (Peer-Review, Conference)

- Jost, B., Holst, C., & Kuhlmann, H. (2023b). How to be more accurate than a single laser scan: Creating the reference geometry of a large wall. In A. Wieser (Ed.), *Beiträge zum 20. Internationalen Ingenieurvermessungskurs, 11.-14. April 2023, Zurich, Switzerland* (pp. 131–144).: Wichmann, Berlin, Offenbach

The generation of a reference geometry of a larger object is more complex due to deformations of the object as described in Publication E [Schmitz et al., 2021b]. However, it is also necessary to analyze long-scale correlations, which is impossible with smaller objects, as done in Publication D [Schmitz et al., 2021c]. Using a sensor of higher accuracy than TLS takes enormous effort as the acquisition is very time-consuming, and the sensors do not always have a sufficient measurement range and resolution. Furthermore, the object could change the geometry within the acquisition or between the generation of the reference geometry and the test scans for the uncertainty analysis (Publication E [Schmitz et al., 2021b]). For this reason, this study proposes a methodology that uses the test scans themselves to generate a reference geometry.

Multiple scans are acquired from different stations, in two faces, and with two different scanners. Errors related to the scanning geometry, the interaction between the object and laser beam, and the scanner misalignments have different effects on the point cloud depending on the scanner's position with respect to the object. The mean of two face scans can reduce the impact of two-face sensitive calibration parameters. Different scanners have different internal scanner errors, and therefore, they also affect the point cloud differently. Although the single effects from single stations act systematically, all these effects together from

different stations and scanners have a rather random character, which leads to the assumption that averaging all the acquired scans will average out the majority of errors. Therefore, the resulting point cloud is more accurate than a single scan.

All scans are calibrated, registered, and averaged by building a grid over the whole point cloud and the median for each grid cell. It is demonstrated that the differences between the two utilized scanners can be significantly reduced by averaging the point clouds of each scanner separately. If two point clouds from different scanners and stations are compared, the residuals have a root-mean-square error (RMSE) of 1.00 mm. This is reduced to RMSE = 0.63 mm if the scanners are installed at the same position and to RMSE = 0.36 mm if the average of 14 scans per scanner is taken. In the final comparison, 95% of the compared points differ less than 0.5 mm. This value can be further reduced when all scans from both instruments are averaged (see Sec. 5.4 for more details).

In the further course of the paper, the averaged point cloud is used as a reference geometry to separate the deterministic part of the point cloud from the stochastic part. This allows for analyzing the laser scanner uncertainty also regarding long-scale correlations (Sec. 6.2). This result further allows the usage of the averaged point cloud in a deformation analysis as it is almost unbiased and much better suited to avoid misinterpreting errors as deformations (Publication G [Jost et al., 2023a]).

Publication G (Peer-Review, Journal)

- Jost, B., Coopmann, D., Holst, C., & Kuhlmann, H. (2023a). Real movement or systematic errors? – TLS-based deformation analysis of a concrete wall. *Journal of Applied Geodesy*, 17(2), 139–149. `https://doi.org/10.1515/jag-2022-0041`

The insufficient knowledge of the error budget and correlations impacts the area-based deformation analysis so far that point cloud differences cannot be reliably tested for significant deformations, and errors may be mistakenly interpreted as deformation. To reduce the latter effect, this study uses the previously introduced method of averaging multiple scans (Publication F [Jost et al., 2023b]) to perform an area-based deformation analysis with the reduced risk of misinterpreting systematic errors as deformations.

The Bonn Reference Wall (Fig. 1.3) is measured from seven different stations in two epochs in August and September 2021 with two laser scanners, namely Leica ScanStation P50 and Z+F Imager 5016. Additionally, the wall is monitored at 17 fixed points with a total station (Leica TS60) to get a reference solution for significant deformations. Several point cloud comparisons are carried out to illustrate the effects of systematic errors on the point cloud comparison. In several cases, the comparison of different scans from the same epoch generates higher deviations than the two-epoch comparison due to systematic effects resulting from the scanning geometry, remaining internal misalignments, and the registration.

While the point clouds within one epoch differ in the ±3 mm range, the actual deformation analysis provides point cloud differences in the range of ±1 mm between two epochs. This magnitude is confirmed by the total station measurements, which revealed a significant deformation of 8 out of 17 points in the magnitude of ±1 mm. By interpolating the area between the points, the color distribution and magnitude look similar between area-based and point-based deformation analyses when the averaging method is carried out. The results are described in more detail in Sec. 5.4.

In conclusion, this study demonstrates that averaging multiple scans makes the area-based deformation analysis more sensitive to smaller deformations and avoids misinterpreting systematic errors as deformations. However, the judgment of whether a point cloud difference is significant is only solved here by comparing the results to total station measurements.

5. Summary of the Most Important Results

The previous chapter summarized the content of all publications relevant for this thesis. This chapter highlights the most important results that were achieved in the named publications, which are

- the establishment of a test field for an easy and efficient determination of the TLS range precision (Sec. 5.1),
- the determination of the resolution capability (Sec. 5.2),
- the derivation of a correlation function for short-scale effects (Sec. 5.3), and
- the establishment of a reference geometry to analyze long-scale correlations (Sec. 5.4).

All aspects contribute to a better understanding of the TLS uncertainty and they provide strategies for the empirical determination of the TLS uncertainty with a special focus on the correlations.

5.1 Test Field for the Easy and Efficient Determination of the TLS Range Precision

While the precision of the angles can be determined once by the manufacturer or the user as it only relies on the instrument, the precision of the range strongly depends on the interaction between the laser beam and the object and the scanning geometry. Therefore, it is very variable. For this reason, this thesis only focuses on the range observations. A meaningful contribution in this research area was made by Wujanz et al. [2017] who demonstrated that the range precision can solely be determined by knowing the intensity of the point (Sec. 3.2). Publication A [Schmitz et al., 2019] developed this approach further by suggesting a very easy and cheap test field that allows qualified users to replicate the experiment to determine the range precision of their instrument. The test field consists of several paper boards with different gray scales (Fig. 5.1). Another option is to use a target with different reflectivities and varied ranges and incidence angles to achieve a large variety of intensity values (Fig. 5.2). By modifying the approach so far that the test field can also be acquired with high incidence angles, a wide range of intensity values can be obtained to determine the function of Eq. (3.18).

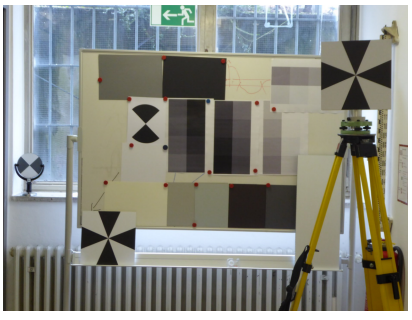

Abbildung 5.1: Cheap setup for an easy determination of the intensity-based range precision [Schmitz et al., 2019].

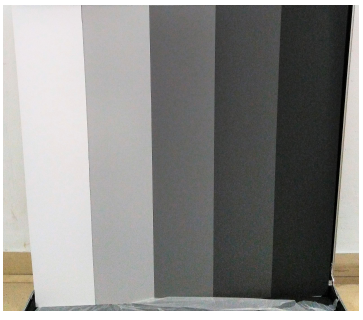

Abbildung 5.2: Target with different reflectivities to get different intensity values (modified from Schmitz et al. [2019]).

Furthermore, the utility of scaled intensity values is investigated as some manufacturers do not provide the original back-scattered intensity as they scale it to increase the visual appearance or to simplify the segmentation [Kaasalainen et al., 2009; Voegtle & Wakaluk, 2009; Kaasalainen et al., 2011; Eitel et al., 2010]. At least for the investigated scanners, it is possible to a limited extent to determine the function of the intensity-based range precision with scaled intensity values. If varying ranges are used, different functions need to be established as the intensity is scaled with the distance for these scanners. However, if the user knows the range of measuring, it is easily possible to determine the function with the suggested approach to get realistic values for the range precision of the scanner that can be integrated into the VCM of the point cloud (Eq. 3.8).

5.2 Determination of the Resolution Capability

Connecting the resolution capability in angular direction with the correlations between the points is a completely new approach. In Publication B [Schmitz et al., 2020], an algorithm has been developed that allows for the determination of the resolution capability in the angular direction. This workflow is more comprehensive than previous ones as it

- determines the resolution capability considering the spatial expansion without making any assumptions on the shape of the laser spot,
- determines the resolution capability continuously in space without discretization up to measurement distances of at least 80 m,
- does not need a reference surface generated by a superior measurement system.

It is discovered that the spatial expansion of the resolution capability is not necessarily circular. For some scanners, it is elliptical with a larger expansion in the vertical direction. On the one hand, this may be caused due to the elliptical shape of the laser spot [Schäfer, 2017]. On the other hand, while the laser beam is emitted, the scanner rotates further in the vertical direction. Depending on the integration time, the beam is elongated [Chaudhry et al., 2021].

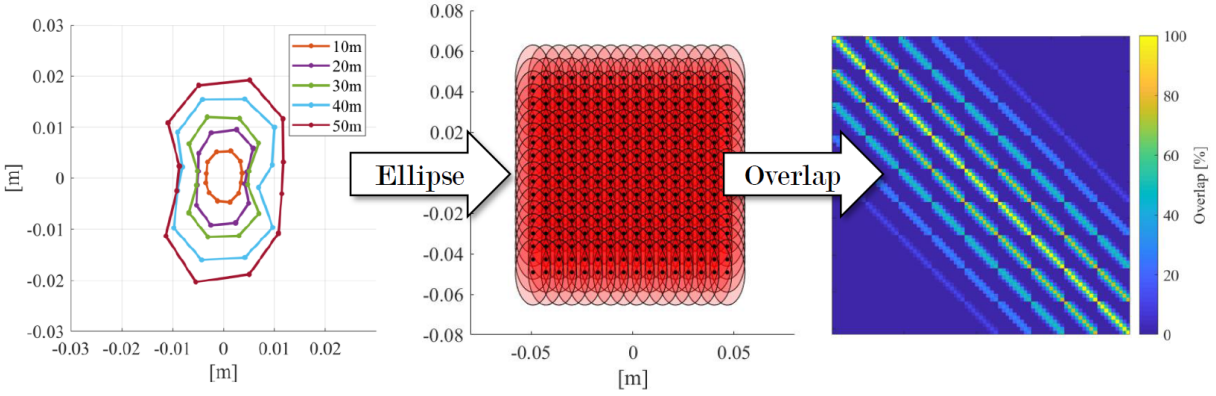

Abbildung 5.3: From the resolution capability to the overlap and correlation matrix (modified from Schmitz et al. [2020]).

For each scanner, a polygon can be determined that describes the resolution capability at a certain distance. Objects that are smaller than the indicated polygon cannot be resolved in the point cloud. Fig. 5.3 (left) depicts the polygons for the distances 10 m, 20 m, 30 m, 40 m, and 50 m for the Leica ScanStation P20 and a resolution of 1.6 mm @ 10 m. It is demonstrated that the spatial expansion is higher in the vertical direction and that the area of the polygon increases with higher distance.

For the integration into the VCM, the polygons are approximated by an ellipse as shown in Fig. 5.3 (middle). The black dots indicate the scan points on a 10 cm x 10 cm planar surface at a distance of 40 m and a resolution of 1.6 mm @ 10 m with the corresponding resolution capability marked in red. All points that lie within one ellipse cannot be resolved as their spots overlap. Thus, they are correlated. The size of the ellipse marks the correlation length and the overlap of different ellipses (Fig. 5.3, right) indicates the percentage to which neighbored points are correlated only considering correlations due to overlapping laser spots. Accordingly, the correlation between the points represented by the correlation coefficient ρ_{ij} is used to derive the covariances σ_{ij} according to Eq. (3.9) to incorporate the correlation into the VCM. Furthermore, as the correlation function can be derived from the overlap matrix, it is possible to estimate the effective number of measurements (Eq. 3.14). Thus, the actual number of points that provide individual information on the object can be determined.

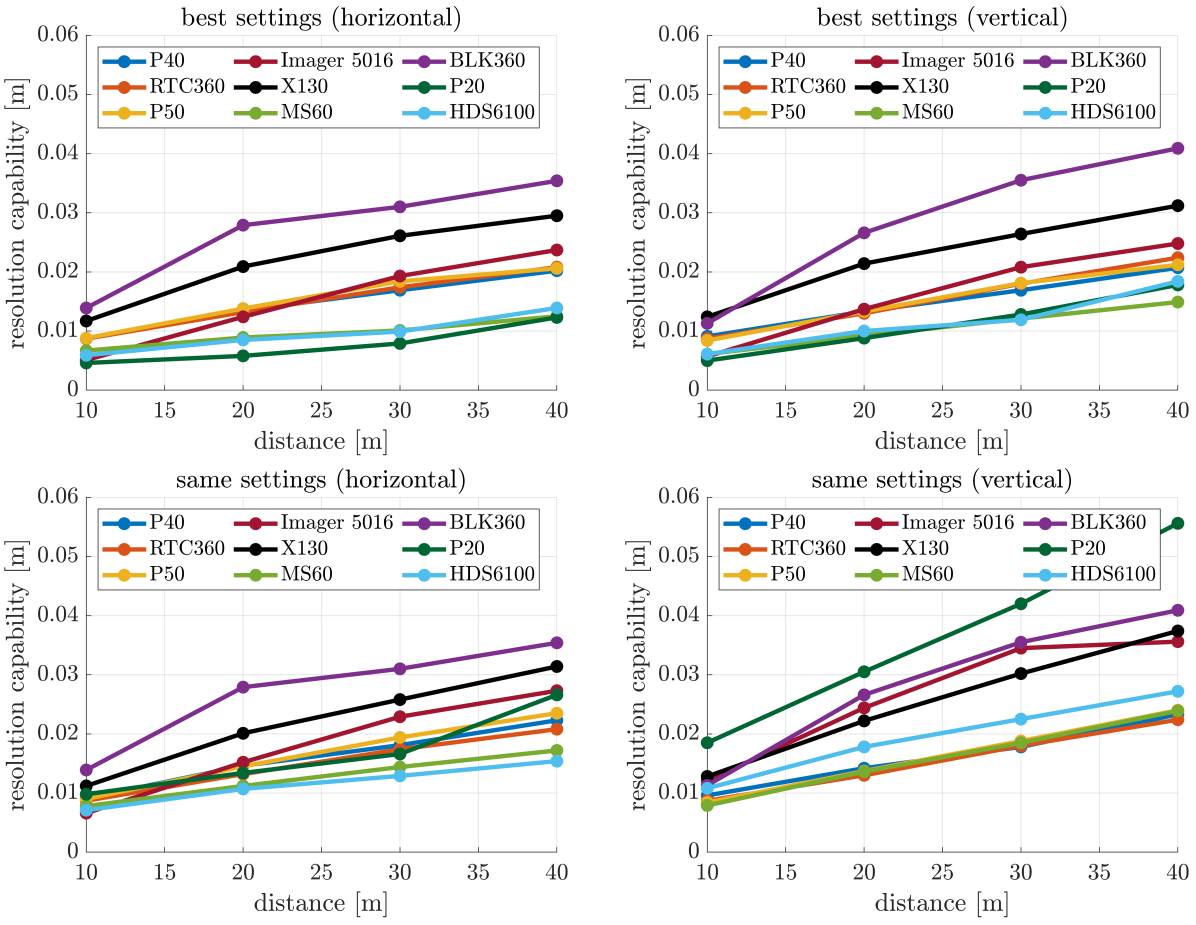

Abbildung 5.4: Resolution capability of different scanners at different distances; left: horizontal direction; right: vertical direction; top: best possible settings; bottom: almost same settings (modified from Schmitz et al. [2021a]).

To get an impression of the resolution capability and the effective number of measurements of different scanners, Publication C [Schmitz et al., 2021a] demonstrates an empirical study on nine different scanners. The resolution capability in the vertical and horizontal directions are depicted in Fig. 5.4 for the best possible scanner settings (highest resolution, highest quality) and comparable scanner settings (approx. 3 mm @ 10 m resolution, besides BLK360 which has 5 mm and lowest quality). The resolution capability increases almost linearly with a higher distance. Moreover, for some scanners, it differs between horizontal and vertical directions, and for some not (P40, P50, RTC 360). For more details on the analysis see Publication C [Schmitz et al., 2021a]. Most importantly, this comparison between scanners and scanner settings allows for answering the following questions:

- Which size of objects can the user resolve with the scanner?
- Which is the right scanner to resolve a certain object?
- Which are the most efficient and economic scanner settings?

The last point refers to the fact that the resolution capability of P40 and P50 does almost not change between the resolution of 0.8 mm @ 10 m and 3.1 mm @ 10 m. This is more specifically addressed in Tab. 5.1, which shows the resolution capability (RC) in the vertical direction at a distance of 30 m and the approximate scanning time for a scanning window of 45°. The values are provided for four scanners that are capable to measure with a resolution of 0.6 mm or 0.8 mm @ 10 m. The scanning time drastically increases while scanning with the highest resolution and highest quality level. The resolution capability of the Leica ScanStation P20 increases significantly when the highest resolution and best quality level are selected. An improvement is also evident for the Z+F Imager 5016. No clear improvement is seen for P40 and P50. When looking at the scan times for a 45° scanning window, it becomes clear how much more time-consuming it is to use the best settings, namely for P20 and Imager 5016 about 30 times and for P40 and P50 about 60 times as long as with the 3.1mm @ 10m. Of course, there are many more possibilities between these two settings. Nevertheless, this table shows how uneconomical the scan with the highest resolution can be in some cases.

Tabelle 5.1: Resolution capability vs. scanning time.

	3.1 mm @ 10 m; Quality low		**0.8mm/0.6mm @ 10 m, Quality high**	
Scanner	**RC (vert) [mm]**	**approx. time [min] 45° scan**	**RC (vert) [mm]**	**approx. time [min] 45° scan**
P20	42.0	00:26	12.8	13:32
P40	17.8	00:26	16.9	27:02
P50	18.8	00:26	18.1	27:02
Imager 5016	34.5	00:23	20.8	15:16

Publications B and C [Schmitz et al., 2020, 2021a] accomplish to get a better understanding of the resolution capability and the consequences for the VCM. The main scientific contributions are summarized as follows:

- An enhanced methodology to determine the resolution capability is developed, which provides information on the minimum size of objects that can be resolved in the point cloud and provides a measure for the economic data acquisition.
- This method can be used for the derivation of a correlation function for short-scale correlations and integration into the VCM.

This allows for the consideration of the proportion of correlations resulting from systematics due to the object surface that can be estimated from the overlapping laser spots. Consequently, the VCM becomes more realistic.

5.3 Deriving a Correlation Function for Short-Scale Effects

As seen in the previous section, the effect of overlapping laser spots has a substantial impact on short-scale correlations. To make the analysis more general and feasible for all materials, Publication D [Schmitz et al., 2021c] suggests a strategy to determine the short-scale correlations. As seen in Sec. 5.2, the correlation structure can be direction-dependent, i.e. anisotropic. Two methods are proposed that determine an elliptical 2D correlation function. One method separates the point cloud into rows and columns (1D), and the other

one uses spatial frequency analysis (SF) to determine the correlation function. In various simulations, the utility of both methods was validated, and also on real data, both methods present similar results within the expected uncertainty. Fig. 5.5 shows the stochastic part of a simulated point cloud correlated according to the Gaussian function

$$\rho(\Delta x, \Delta z) = r_c \cdot e^{-(\frac{\Delta x}{kx})^2 - (\frac{\Delta z}{kz})^2}, \tag{5.1}$$

with the parameters correlation length in horizontal direction $k_x = 6$ cm, in vertical direction $k_z = 12$ cm, and ratio of colored noise $r_c = 60\%$. The correlation length is defined as the distance where the correlation amounts to 37%. The spatial distances in horizontal and vertical direction are denoted by Δx and Δz. The corresponding correlation function is depicted in Fig. 5.6.

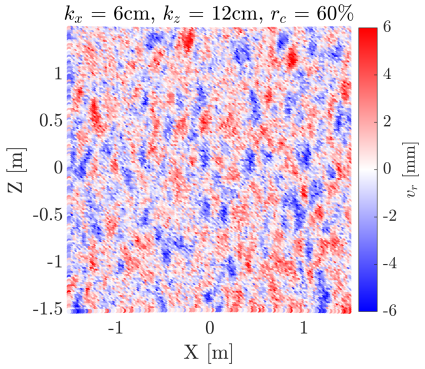

Abbildung 5.5: Simulated example for the stochastic part of correlated TLS measurements.

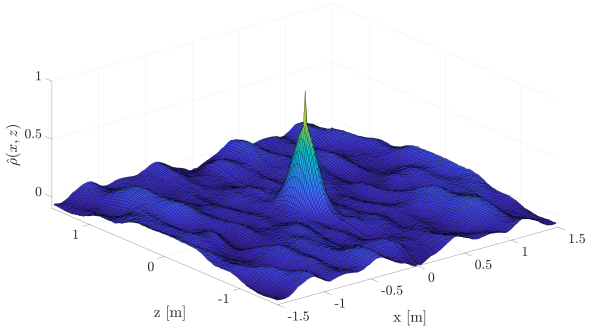

Abbildung 5.6: Correlation function that is used to correlate the measurements of Fig. 5.5 [Schmitz et al., 2021c].

Having evaluated the methods, the SF method has been considered to be more practicable on TLS data as it is more efficient and does not require the separation of the point cloud into rows and columns. Thus, it is applied to real data sets of a 1.50 m x 1.50 m wooden wall. The trend is subtracted by measuring the true geometry with a Leica Laser Tracker AT901 that has superior accuracy to the TLS. The remaining residuals are illustrated in Fig. 5.7 for the Z+F Imager 5016 and Fig. 5.8 for the Leica BLK360. Both scans are taken from a distance of 15 m to the wall and a resolution of 3.1 mm @ 10 m for the Z+F Imager 5016 and 5 mm @ 10 m for the Leica BLK360. These settings are chosen based on the results from Sec. 5.2. Therein, it is demonstrated that scanning with a higher resolution is not beneficial to get more details at this distance. Thus, these settings are an economically good choice to derive detailed data.

At first glance, the differences v_r between reference geometry and point cloud are much higher for the BLK360, but also the correlation structures of both instruments differ, as the area of residuals with the same magnitude is smaller but more elongated for the Imager 5016 compared to the BLK360. That demonstrates that the short-scale correlations strongly depend on the chosen instrument, but also that they exist. The empirical correlation function is estimated from the data according to Eqs. (3.11) and (3.12). Through these data, an analytical Gaussian function is estimated according to Eq. (5.1) as it suits the data the best. The choice of the right correlation function was not the focus of the study. Of course, also other analytical functions can be fitted through the empirical correlation function. Tab. 5.2 contains the estimated parameters that describe the correlation functions for both scanners. The results confirm the visual inspection that the shape of the BLK360 has a similar expansion in both directions but for the Imager 5016, the expansion is much more distinct in the vertical direction.

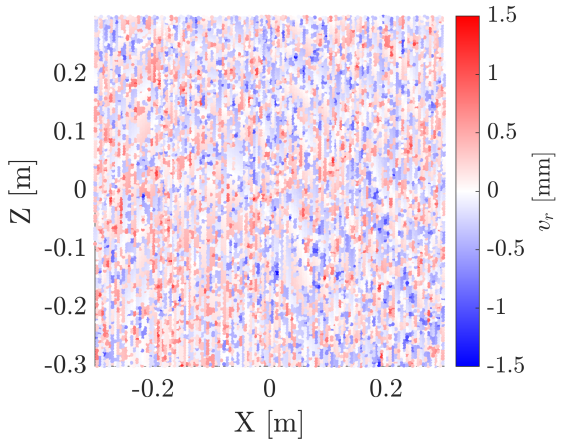

Abbildung 5.7: Stochastic part of the Z+F Imager 5016 acquired at a distance of 15 m with a resolution of 3.1 mm @ 10 m.

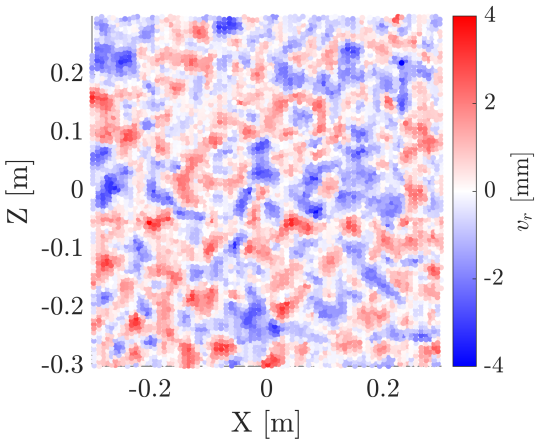

Abbildung 5.8: Stochastic part of the Leica BLK360 acquired at a distance of 15 m with a resolution of 5 mm @ 10 m.

Tabelle 5.2: Estimated parameters of the Gaussian correlation function (Eq. 5.1) for the empirical data sets of the Z+F Imager 5016 and the Leica BLK360.

Scanner	$\hat{k}_x$ **[mm]**	$\hat{k}_z$ **[mm]**	$\hat{r}_c$ **[mm]**
Imager 5016	3.9	12.6	70.2
BLK360	19.6	20.8	86.5

For the numerical interpretation, Figs. 5.9 and 5.10 demonstrate the expansion of the correlation by showing 25 measured points at a distance of 15 m indicated in black. The red ellipses represent the correlated area where the correlation is at least 37%. All points that lie within one ellipse are correlated, which are five points in vertical direction for the Imager 5016 and five points in vertical and horizontal direction for the BLK360 and all points that are included in between.

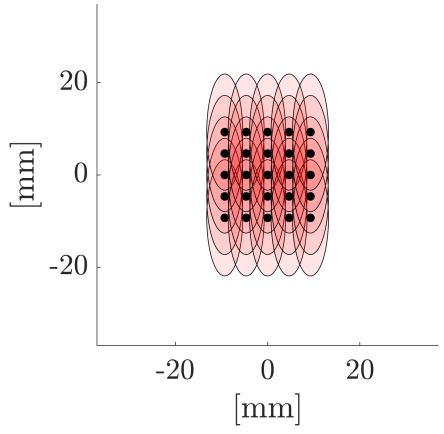

Abbildung 5.9: Exemplary representation of the correlation of 5x5 points measured with the Imager 5016. The black dots represent the measured points and the ellipses the area where the correlation is at least 37%. The axes of the ellipses correspond to the correlation lengths given in Tab. 5.2.

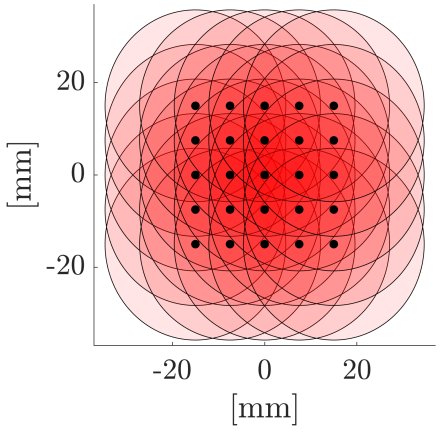

Abbildung 5.10: Exemplary representation of the correlation of 5x5 points measured with the BLK360. The black dots represent the measured points and the ellipses the area where the correlation is at least 37%. The axes of the ellipses correspond to the correlation lengths given in Tab. 5.2.

So far, two different methods have been introduced. One approach determines the correlation lengths using the resolution capability (RC-method, Sec. 5.2) and the other one analyzes the stochastic part of the point cloud (SP-method, this section). Figs. 5.11 and 5.12 compare the results of both methods. The RC-method obtains $k_x = 20.9$ mm and $k_z = 18.8$ mm for the BLK360. These values differ in maximum 2 mm or even less from the results given in Tab. 5.2, which shows that both methods obtain results in the same magnitude given that both methods have uncertainties in their determination. The RC-method estimates $k_x = 10.9$ mm and $k_z = 18.3$ mm for the Imager 5016, which differ $\Delta k_x = 7.0$ mm and $\Delta k_z = 5.7$ mm from Tab. 5.2. This results from uncertainties in both estimations and it must be noted that an aluminum test specimen is used for the resolution capability but a wooden wall is used for the separation of the stochastic part. As will be demonstrated later in this section, this leads to different correlation behavior. Furthermore, Chaudhry et al. [2021] demonstrated that the resolution capability lies within a certain bandwidth. Comparing their simulated values of the resolution capability to the correlation lengths obtained herein, these values lie within the bandwidth that is obtained for the Imager 5016.

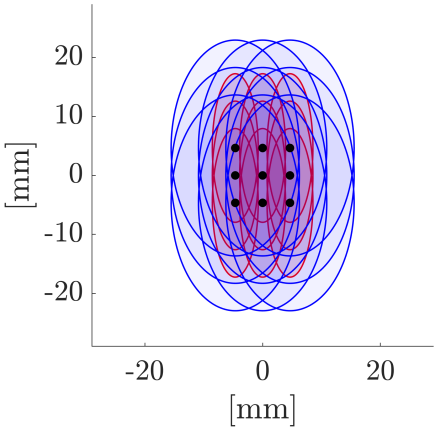

Abbildung 5.11: Comparison of the correlation lengths determined for the the Imager 5016 with empirical approach using the stochastic part of the point cloud (red) to the approach using the resolution capability (blue).

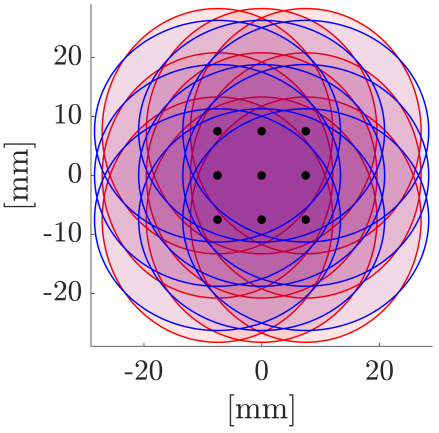

Abbildung 5.12: Comparison of the correlation lengths determined for the the BLK360 with empirical approach using the stochastic part of the point cloud (red) to the approach using the resolution capability (blue).

With the given parameters of the correlation function ρ, it is possible to fill the VCM using Eqs. (3.9) and (3.8). This method assumes stationary data, which can only be realized for smaller point clouds that hit the same material with the same angle of incidence, and the same range. Hence, it cannot be simply adopted to data sets of larger objects.

Influence of Different Scanning Configurations on the Correlation Structure of the Point Cloud

The previous results have been obtained for an orthogonal surface of the same reflectivity. However, while scanning larger objects, the range, incidence angle, and reflectivity change (Fig. 1.4). For this reason, Publication D [Schmitz et al., 2021c] investigated how far the correlation length in vertical direction changes using different of the latter mentioned parameters. Fig. 5.13 and Fig. 5.14 demonstrate the results, respectively. A target with five different reflective surfaces (Fig. 5.2) is scanned with varying scanning geometries and the correlation function is determined for each panel. Fig. 5.13 depicts the variation of the correlation length while scanning different gray scales at a distance of 15 m and a resolution of 3.1 mm @ 10 m with the Z+F Imager 5016. The color in the plot corresponds to the color on the target. The left bar of each color belongs to an incidence angle of 10°, and the right bar to an incidence angle of 50°. The brighter the surface the longer the correlation length, which is reasoned by the signal-to-noise ratio that is much higher for strong

reflective surfaces [Soudarissanane et al., 2011]. Furthermore, more signal is reflected and contributes to the distance measurements, i.e. the effective spot size is higher. Moreover, the correlation length increases for higher incidence angles. Here, the spot is elongated and the previous explanation holds likewise.

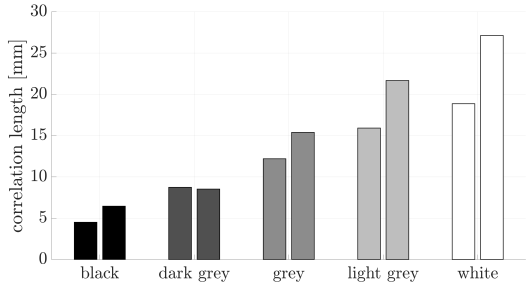

Abbildung 5.13: Correlation length depending on the reflectivity and incidence angle of the target (modified from Schmitz et al. [2021c]).

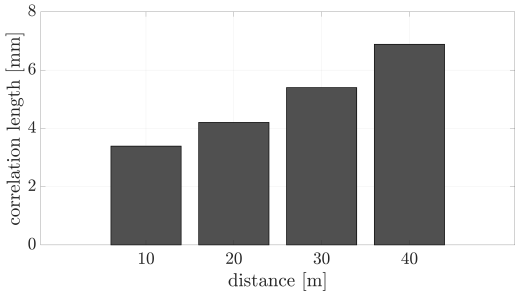

Abbildung 5.14: Correlation length depending on the distance between scanner and target (modified from Schmitz et al. [2021c]).

Fig. 5.14 presents the results for different ranges of the gray panel scanned with a resolution of 3.1 mm @ 10 m with the Z+F Imager 5016 at an incidence angle of 0° in the middle of the target. The correlation length increases with longer distance, which is related to the increased laser spot. Fig. 5.15 illustrates the spot size of three consecutively scanned points according to the spot size provided by the manufacturer [Zoller + Fröhlich, 2018]. It shows that the overlapping area of two spots increases as also the spot size increases. Thus, the area where two spots illuminate the same surface increases and so does the correlation length.

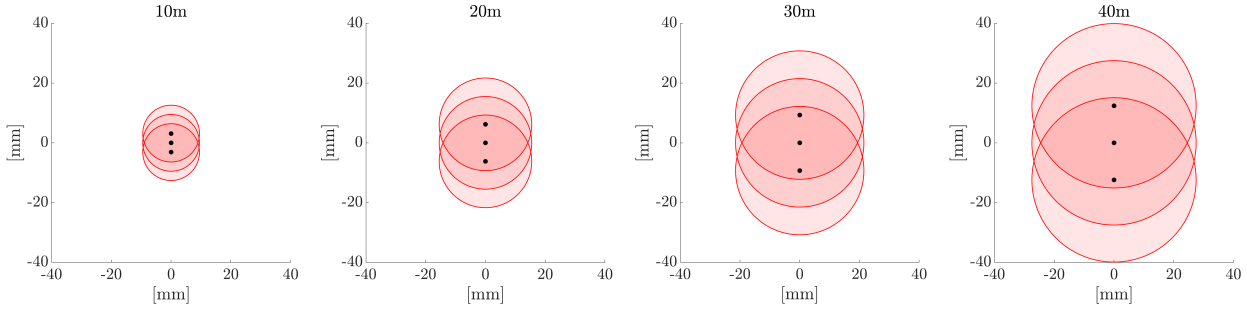

Abbildung 5.15: Laser spots (red) of three consecutively measured points (black) at four different distances.

These investigations demonstrate the relevance of determining the correlation length empirically as it has many impact factors. To transfer this method to larger objects where the scan range and incidence angle change along the object, Publication D [Schmitz et al., 2021c] also proposes a possible workflow by determining stationary patches [Schabenberger & Gotway, 2005, p. 425],[Atkinson & Lloyd, 2007], applying the SF method to determine the covariance function and to combine all patches by kernel convolution as suggested in Darbeheshti & Featherstone [2009].

In conclusion, the results contribute to the current research on the stochastic model of TLS as follows:

- Two methods are proposed to determine the short-scale correlations resulting from overlapping laser spots and the interaction between laser beam and object surface.
- The correlation function of four different scanners is determined and it differs between the scanners. Further variations are demonstrated for different ranges, incidence angles, and surface reflectivities.

- A workflow is suggested to approach the determination of short-scale correlations in non-stationary data, e.g. when the object is larger and the scanning geometry changes.

Thus, the integration of the short-scale correlations is now possible if a reference surface of the test object can be generated.

5.4 Establishment of a Reference Geometry to Analyze Long-Scale Correlations

As demonstrated in the previous section, the establishment of a reference geometry is necessary to separate the deterministic and stochastic parts to analyze the uncertainty of TLS. As seen before, using a geometric primitive or sensor of higher accuracy works fine for smaller structures. However, most objects in engineering tasks are larger than a few meters. Thus, a strategy is needed to analyze the uncertainty also for larger structures.

Publications E and F [Schmitz et al., 2021b; Jost et al., 2023b] contribute to the establishment of a reference geometry of the Bonn Reference Wall (Fig. 1.3) that is used to analyze the uncertainty of different scanners. To avoid the misinterpretation of deformations as errors in the scanner, it is mandatory that the test object does not deform or that the deformation is known. Fig. 5.16 demonstrates the effect: the trend (black) must be subtracted from the point cloud to analyze the stochastic part (red). If the wall deforms, the trend also deforms (green). In case the deformation is not considered, the analysis of the uncertainty is erroneously biased by the deformation.

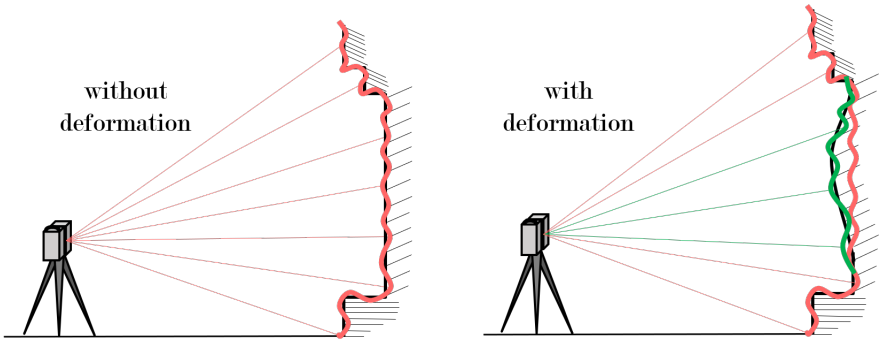

Abbildung 5.16: Measurement signal for an object without and with deformation (modified from Schmitz et al. [2021b]).

Stability of the Object

Publication E [Schmitz et al., 2021b] analyzes the Bonn Reference Wall for deformations (Sec. 4.3). The wall was monitored over six different days within one year with different atmospheric conditions. It was found that

- if there is a strong temperature gradient over the day, the wall bends with ±0.5 mm, and
- the upper part of the wall deforms up to 7 mm between summer and winter.

These values are not negligible in terms of the uncertainty analysis of TLS. Thus, a deformation model is proposed that aims at modeling the out-of-wall deformation ($\mathbf{\Delta y_{abs}}$) based on the temperature the day

before $\mathbf{T}_{-1d}$, the temperature one hour before $\mathbf{T}_{-1h}$, the temperature at the time of measuring $\mathbf{T}$, and the position on the wall $\mathbf{x}, \mathbf{z}$:

$$\begin{aligned}
&\boldsymbol{\Delta}\mathbf{y}_{\mathbf{abs}}(\mathbf{T}, \mathbf{T}_{-1d}, \mathbf{T}_{-1h}, \mathbf{x}, \mathbf{z}) = \\
&+(p_{10} + p_{11}\mathbf{x} + p_{12}\mathbf{z} + p_{13}\mathbf{x^2} + p_{14}\mathbf{xz} + p_{15}\mathbf{z^2})(\mathbf{T}_0 - \mathbf{T}) \\
&+(p_{20} + p_{21}\mathbf{x} + p_{22}\mathbf{z} + p_{23}\mathbf{x^2} + p_{24}\mathbf{xz} + p_{25}\mathbf{z^2})(\mathbf{T}_{-1d} - \mathbf{T}) \\
&+(p_{30} + p_{31}\mathbf{x} + p_{32}\mathbf{z} + p_{33}\mathbf{x^2} + p_{34}\mathbf{xz} + p_{35}\mathbf{z^2})(\mathbf{T}_{-1h} - \mathbf{T}).
\end{aligned} \tag{5.2}$$

The model manages to reduce the displacements so that the outcome of the model has a standard deviation of 0.61 mm, which is too much for the uncertainty analysis since Publication A [Schmitz et al., 2019] determines a range precision of lower than 0.4 mm. Thus, the deformation may still be misinterpreted. To avoid this, Publication E [Schmitz et al., 2021b] proposes a second model that only models the variation within one day with the assumption that the initial geometry of the wall on the day of measuring is known either by the acquisition with a total station or by the fact that the reference geometry is generated the same day. The relative movements are reduced to a maximum deviation of 0.25 mm and a standard deviation of 0.16 mm, which is sufficient for the TLS uncertainty analysis.

Generally, Publication E [Schmitz et al., 2021b] helps to understand and describe the stability of the Bonn Reference Wall. The following main conclusions can be drawn:

- Large objects are affected by the atmospheric conditions and therefore, they change their geometry. This must be considered while using such an object as a test object to analyze the scanner's uncertainty.
- The dynamic modeling of the absolute wall movement requires a much more enhanced monitoring strategy than proposed to get an adequate deformation model that is sufficient for the accuracy requirements.
- The initial geometry of the wall on the day of collecting the test scans must be acquired, for example with a total station, to reduce the uncertainty due to the deformation of the wall between the reference day and the day of measuring. It would be even better to perform the measuring of the reference geometry and the test measurements on the same day. If the atmospheric conditions are constant, there is no need to apply a deformation model.

Generating a Reference Geometry

Since the establishment of an absolute deformation model is not sufficient to analyze the uncertainty on a sub-millimeter level, Publication F [Jost et al., 2023b] presents a methodology to generate a surface of higher accuracy while acquiring the test measurements. Therefore, scans are taken from seven different stations (Fig. 5.17) in two faces and with two scanners (Leica ScanStation P50 and Z+F Imager 5016). The idea is that due to the different scanners and scanning configurations, the systematically acting error sources affect the point clouds differently, which gets a random character. Hence, Publication F [Jost et al., 2023b] suggests to average all these scans to average out systematic errors. The method works as follows: After registering all scans, the data is gridded with a defined 2D grid size. All the points that lie within one grid cell are averaged for each coordinate component (X, Y, Z) separately. The median is taken as a robust mean to avoid that a badly registered point cloud influences the whole reference geometry. The resulting 3D points build the averaged point cloud.

The scanners are contemporaneously calibrated in the neighbored calibration field that has been established by Medić [2021]. Fig. 5.18 (top) shows the M3C2 differences between both scanners while the P50 is placed on S3 and the Imager 5016 on S4 (Fig. 5.17). Here, the influence of the scanning geometry, namely the orientation of the object to the scanner becomes obvious. Deviations of ±2.5 mm occur due to different scanners and the position of the scanners. In Fig. 5.18 (top), the root-mean-square error of the deviations is RMSE = 1.00 mm.

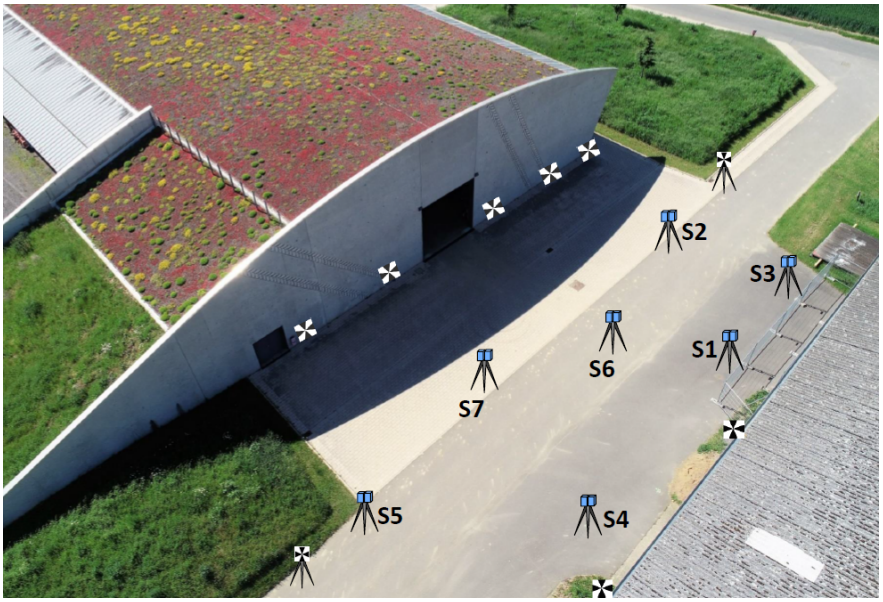

Abbildung 5.17: Scanner stations in front of the Bonn Reference Wall (modified from Jost et al. [2023b]).

The middle of Fig. 5.18 demonstrates the improvement of scanning from the same station as it shows the differences between both scanners that both scanned from S6. Only errors remain that result from the different scanners and the registration with the RMSE = 0.63 mm. The bottom plot in Fig. 5.18 depicts the success of averaging all 14 scans from one scanner as it shows the differences between both averaged point clouds. The deviations are significantly reduced as a lot of white areas remain with the RMSE = 0.36 mm. Consequently, systematic errors are strongly reduced by averaging multiple scans as the deviations between two different scanners shrink. Thus, averaging all scans of both scanners leads to an even more accurate point cloud, which can then be used to evaluate the uncertainty of terrestrial laser scanners.

The averaged point cloud is used to remove the deterministic trend from the point cloud, so only the stochastic part remains. In Fig. 5.19, this is exemplarily depicted for one scan of the Z+F Imager 5016 acquired from S6. The stochastic part is extracted by meshing the averaged point cloud and by building the cloud-to-mesh distance (C2M) to the test scan. The colors in Fig. 5.19 indicate the C2M distances. On the right, a cutout of 0.8 m x 0.8 m is shown whose location is marked with a red square in the left plot.

Even though the scan is calibrated, systematic errors are still visible in the comparison as large areas of points that are spatially close to each other have the same magnitude of the C2M distances. These errors could bias a surface approximation or a deformation analysis as they may be erroneously interpreted as deformations. However, zooming into smaller parts as in Fig. 5.19 (right), the distribution of the residuals is more random and only small-scale correlations are visible. Thus, this smaller patch can be assumed to be stationary. The methodology from Publication D [Schmitz et al., 2021c] is applied to the smaller patch to determine its correlation function according to Eq. (5.1). The following parameters are estimated for an orthogonal distance of 14 m between scanner and object: ratio of colored noise $r_c = 65\%$, correlation length in horizontal direction $k_x = 3.7$ mm, and correlation length in vertical direction $k_z = 11.6$ mm. Compared to the results from Tab. 5.2 that were obtained for a wooden wall with 15 m distance between the scanner and the object, the values are very similar even though the scanned material is different. This shows that the presented method to determine the reference surface is also suitable for the determination of short-scale correlations. However, considering Fig. 5.19, the existence of long-scale correlations is much more distinct than the short-scale correlations.

In conclusion, the generation of a test field to analyze long-scale correlations succeeded:

- It is possible to generate an up-to-date reference surface of higher accuracy, that is free from deforming influences, by averaging multiple point clouds from multiple stations.

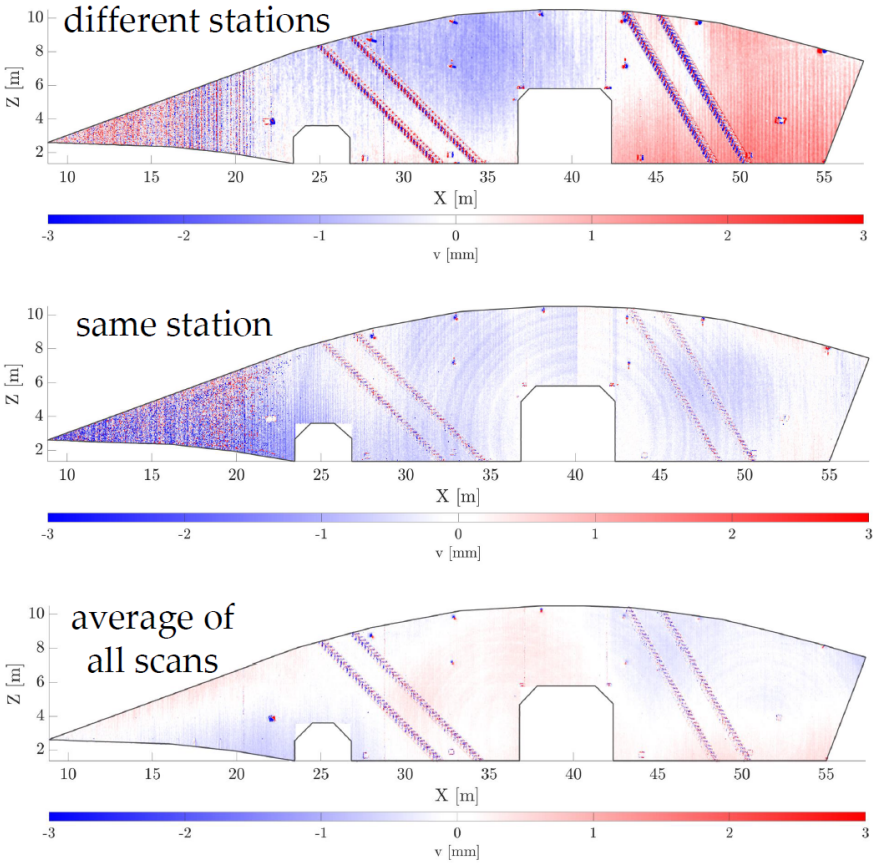

Abbildung 5.18: M3C2 differences between point clouds of the Leica ScansStation P50 and the Z+F Imager 5016 to demonstrate the improvement that is yielded by averaging multiple scans. Top: M3C2 differences between a single calibrated scan of P50 captured from S3 and a single calibrated scan of Imager 5016 captured from S4; Middle: M3C2 differences between a single calibrated scan of P50 and a single calibrated scan of Imager 5016 captured from S6; Bottom: M3C2 differences between the averaged point cloud of the P50 and the averaged point cloud of the Imager 5016 using uncalibrated scans (modified from Jost et al. [2023b]).

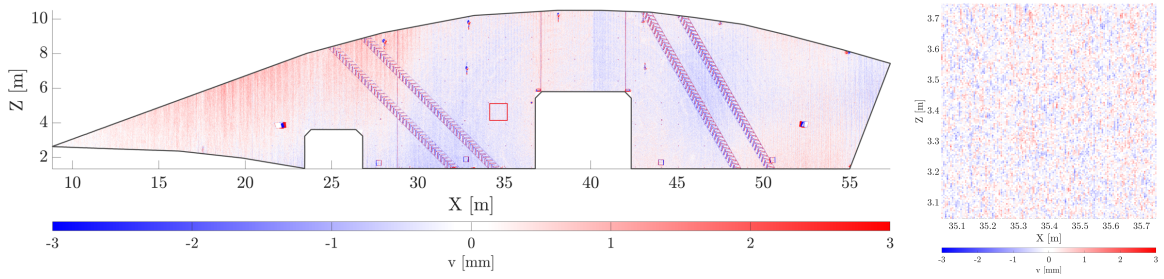

Abbildung 5.19: Stochastic part of the point cloud acquired with the Z+F Imager 5016 by illustrating the C2M distance between the reference point cloud and a calibrated scan from S6 (modified from Jost et al. [2023b]).

- The averaged point clouds can be further utilized to perform an area-based deformation analysis since the influence of systematic errors is significantly reduced.

Utility in an Area-Based Deformation Analysis

To evaluate the performance of the established method, Publication G [Jost et al., 2023a] compares an area-based deformation analysis with a point-based deformation analysis performed with a total station. Therefore, the Bonn Reference Wall is measured again from seven different stations with two faces and two scanners (Leica ScanStation P50 and Z+F Imager 5016). The scanners are additionally calibrated each day of measuring. Furthermore, a point-based measurement is carried out with a Leica TS60 at 17 signalized points on the wall. The measurements are repeated in August and September 2021 to evaluate the deformation of the wall within that time.

Fig. 5.20 depicts the M3C2 distances between the averaged point clouds of August and September 2021. Differences in the magnitude of ±1 mm are visible. Compared to the results from Fig. 5.18, it is not possible to say whether these differences result from systematic errors or real deformations. For this reason, the results are compared to a point-based deformation analysis according to the description of the congruence model given in Sec. 3.5.

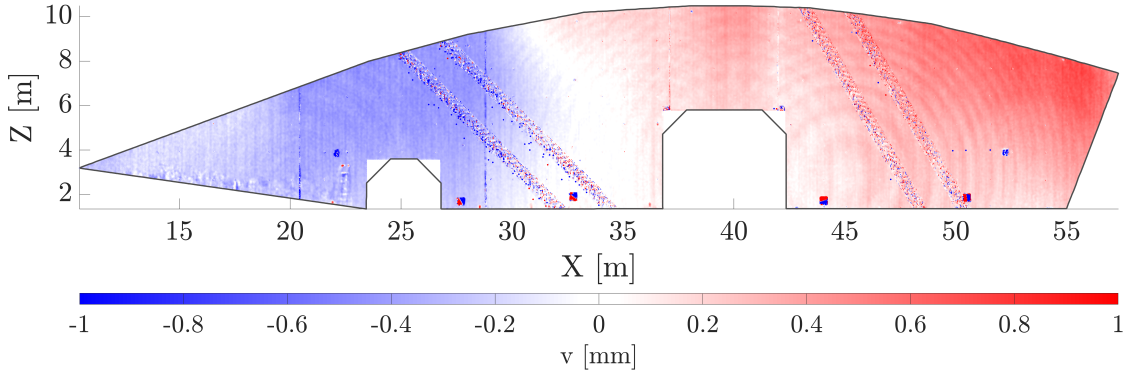

Abbildung 5.20: M3C2 differences between the two averaged point clouds of August and September using all calibrated scans of the Leica ScanStation P50 and the Z+F Imager 5016 (modified from Jost et al. [2023a]).

Fig. 5.21 demonstrates the differences between both epochs that have been determined at 17 different points with a total station. All points with a red square did significantly move. The magnitude of deformation is up to ±1 mm, which is small but the magnitude and color distribution is similar to the one of the area-based deformation analysis. This becomes more prominent when interpolating the area between the points (Fig. 5.22). The magnitude and color distributions are almost similar to the area-based deformation analysis (Fig. 5.20).

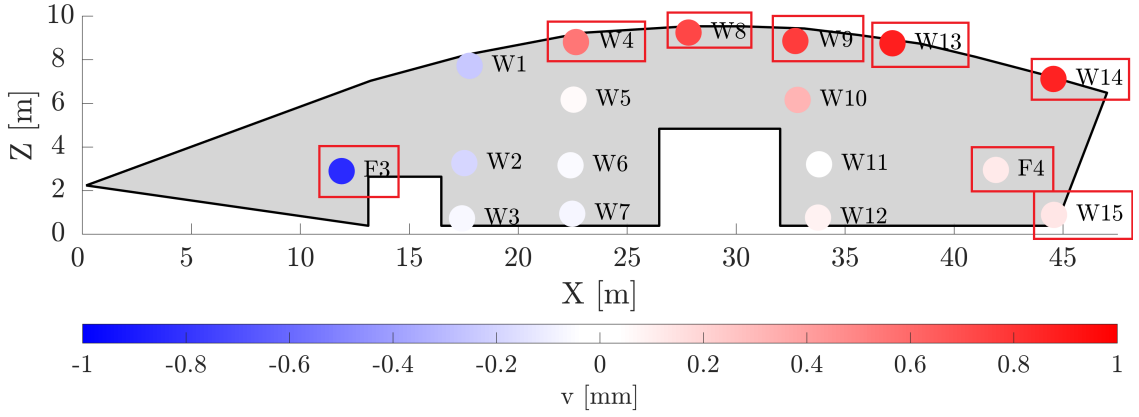

Abbildung 5.21: Point-based deformation analysis with significantly deformed points (red squares) (modified from Jost et al. [2023a]).

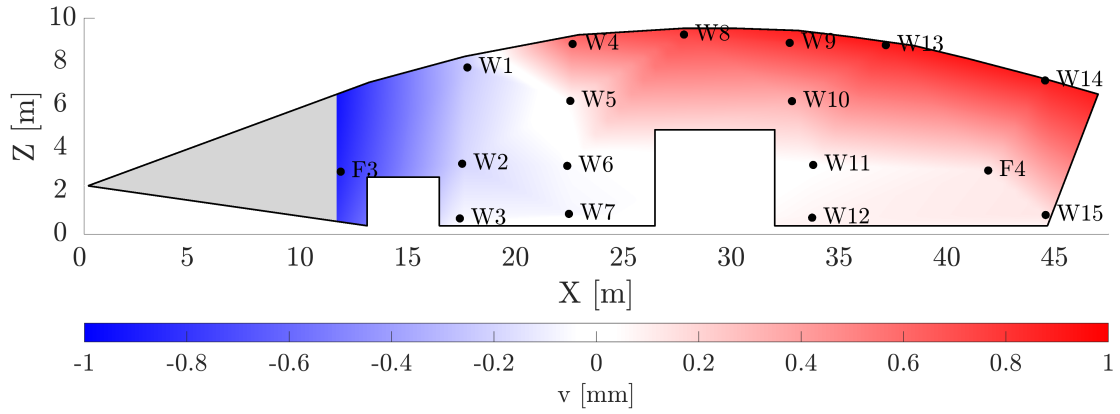

Abbildung 5.22: Interpolated results of the point-based deformation analysis (modified from Jost et al. [2023a]).

Tabelle 5.3: Out-of-plane differences between August and September determined with the point-based and the area-based deformation analysis.

Point	Point-based [mm]	Area-based [mm]	Δ [mm]
F3	**-0.84**	**-0.21**	**0.63**
F4	**0.11**	**-0.38**	**0.49**
W1	-0.24	-0.35	0.11
W2	-0.19	-0.25	0.06
W3	-0.06	-0.23	0.17
W4	**0.55**	**0.29**	**0.26**
W5	0.05	0.01	0.04
W6	-0.05	0.01	0.06
W7	-0.07	0.03	0.10
W8	**0.73**	**0.32**	**0.41**
W9	**0.77**	**0.43**	**0.34**
W10	0.32	0.23	0.09
W11	0.03	0.10	0.07
W12	0.08	0.06	0.02
W13	**0.88**	**0.50**	**0.38**
W14	**0.87**	**0.82**	**0.05**
W15	**0.13**	**0.27**	**0.14**

To get a more quantitative comparison between the point-based and the area-based deformation analyses, the differences of Fig. 5.20 at the locations of the discrete points in Fig. 5.21 are manually read. The comparison of these values to the differences determined in the point-based analysis and are given in Tab. 5.3. The third column indicates the differences between both methods. If these differences are significant or not is not possible to determine so far as no significance level for the TLS measurements exist. All points that significantly moved in the point-based deformation analysis are marked in bold font. Except for F4, all points that significantly moved have the same sign and thus the same movement direction. The magnitude of the movement is mostly smaller for the area-based deformation analysis than for the point-based one. The largest differences between both method are obvious for points F3 and F4, which are installed with additional adapters at the wall that are different for TLS and total station measurements. For all other points, the

targets and prisms are affixed to the same magnetic nests, which reduces the additional uncertainty due to the adapters. The highest difference between both methods for these points is 0.4 mm. For these points that have not been identified to move significantly in the point-based deformation analysis, the mean differences between both methods is 0.08 mm, which seems very small compared to uncertainty that can be reached with a total station or a laser scanner. Compared to the differences between two single scans from the same epoch, which amount up to 3 mm (Fig. 5.18), all differences between both methods are small. This demonstrates that the differences between the averaged point clouds of August and September yield from real deformations, at least to a high percentage, which shows that the averaging method allows for a much more sensitive deformation analysis as the differences do not result from systematic errors from the scanning process. This leads to the fact that systematic errors can no longer be misinterpreted as deformations of the object as they are averaged out before the deformation analysis.

All in all, the results of both methods coincide in terms of movement direction and points that did not significantly move. To state whether the magnitude of deformation can be statistically seen as equal or not can only be said when a significance level for the TLS measurement is established. This could be reached by carrying out this experiment multiple times to derive empirical confidence intervals. However, the overall deformation is very small and the coordinate differences of the measured points are close to the edge of being significant. Thus, this analysis should be repeated with a larger deformation where it is clear whether a deformation exists or not.

6. Further Considerations

This study focuses on conceptualizing test scenarios and methodologies to analyze the uncertainty of terrestrial laser scanners based on empirical data without identifying individual error sources as the transition behavior between error sources and their impact on the point cloud is very complex. Special attention is paid to determining short-scale correlations from the interaction between the laser beam and object and establishing a test scenario to investigate long-scale correlations. These methods contribute to a better understanding and quantification of the TLS uncertainty and the correlations between the observations. However, it opens the space for the following new questions to be solved to create a fully populated VCM for a TLS point cloud that can be used, for example, for the congruence test in an area-based deformation analysis or the correct and unbiased modeling of surfaces:

- Correlation functions have been established for stationary data in local patches (Sec. 4.2). A strategy is introduced to derive the VCM, including short-scale correlations for non-stationary data of larger objects. Furthermore, a method is established to separate the deterministic and stochastic parts of a point cloud from a larger object that consists of long-scale correlations (Sec. 5.4). However, a strategy is missing to quantify these correlations to integrate them into the VCM.
- If this strategy exists, the question arises of combining short-scale and long-scale correlations in a fully populated VCM. Since point clouds usually consist of a few million points a fully populated VCM has a size that is impossible to handle or since it is necessary for adjustments, to invert.

The contributions of this thesis can be used to further follow the goal of establishing a fully populated VCM in future research. Several possible strategies can be thought of to integrate correlations into the VCM. On the one hand, empirical studies can be carried out to be able to functionally describe the correlation behavior also for the so far rather poorly describable influences such as scanning geometry and interaction between laser beam and object surface to integrate them into a synthetic VCM according to the elementary error model (Chap. 2). On the other hand, the described strategies can be used for the backward modeling the stochastic properties that will be integrated into a combined VCM.

Both options need further investigations on short-scale correlations described in Sec. 6.1. The basis for analyzing long-scale correlations is given in this thesis. However, a strategy for proceeding further in the analysis must be part of future research as elaborated in Sec. 6.2. The combination of both correlation types will be addressed in Sec. 6.3.

6.1 Further Investigations on Short-Scale Correlations

The integration of object-related errors that create short-scale correlations into the VCM has been missing so far. Contributions were made in Publications B, C, and D [Schmitz et al., 2020, 2021a,c]. The integration of short-scale correlations either requires knowledge of the resolution capability or a reference geometry of the object. So far, both methods estimated correlations for orthogonally oriented relatively planar surfaces. However, Sec. 5.3 demonstrates the influences of the scanning geometry and the object reflectivity on the correlation pattern. To have a more generalized determination of correlations that allows for the functional modeling of the correlation length depending on the reflectivity and the scanning geometry, the experiments must be widened to a more extensive variety of setups. Having gained more knowledge on the behavior of short-scale correlations at different scanning configurations and reflectivities, these effects may be introduced in the synthetic VCM based on the elementary error model [Kerekes & Schwieger, 2020]. This requires an enhanced analysis of the resolution capability (Sec. 6.1.1) and the usage of a reference geometry with different scanning configurations (Sec. 6.1.2).

6.1.1 Enhanced Analysis of the Resolution Capability

The resolution capability provides a valuable measure to determine the minimum size of the object that can be resolved in the point cloud and is a helpful indicator to plan economic measurements. The integration of the correlations derived from the resolution capability into the VCM also allows for a more realistic parameter estimation within an adjustment.

The determination strongly depends on the scanning configuration. To make it a more general concept, a more extensive empirical analysis is needed that includes the determination of the resolution capability at different incidence angles and higher elevations. The test specimen used herein is only suitable for orthogonal measurements as the determination relies on parallel planes with a spatial gap (Publication B [Schmitz et al., 2020]). Scanning with a higher incidence angle would not allow quantifying the transition area where the laser beam hits both surfaces as the laser beam also reaches areas behind the foreground plane.

Alternatively, Chaudhry et al. [2021] introduced a methodology for predicting the resolution capability of phase-based scanners in angular direction based on information from the data sheet and simple experiments. The algorithm provided in this study can be used to determine the resolution capability of certain scanners without performing additional empirical experiments. However, this must be transferred to pulse-based scanners, and different scanning configurations are not yet introduced.

A possible solution for additional empirical experiments would be to use planes with different radiometric properties instead of planes with spatial gaps between the surfaces. The effect is almost the same: the laser beam hits two surfaces with different radiometric properties. Thus, the back-scattered intensity is averaged over the whole spot, creating a transition area with a mixed intensity of the two bordering planes. The idea becomes more conceivable when taking a look at a black and white target (Fig. 6.1) and the resulting point cloud that is colored in the corresponding intensities (Fig 6.2). The intensity values of the black parts are red, and the ones of the white parts are blue. The transition area, where the beam hits both areas, is green and yellow. The width of this area can be determined as the resolution capability. This setup allows for a more general analysis as it can also be used for higher incidence angles, higher elevations, and different reflective surfaces.

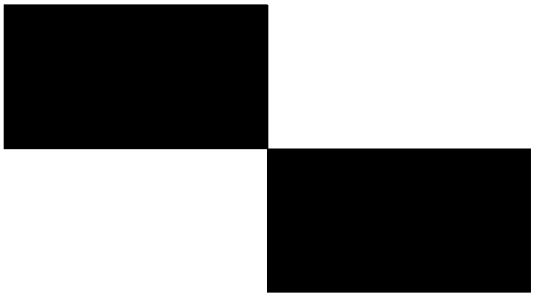

Abbildung 6.1: Exemplary target for determining the resolution capability based on radiometric information.

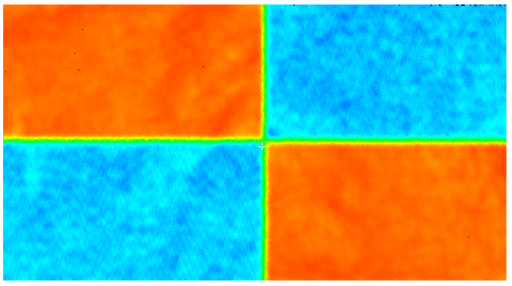

Abbildung 6.2: Point cloud of the black and white target in Fig. 6.1. The colors indicate the different intensity values.

6.1.2 Using a Reference Geometry for the Determination of Short-Scale Correlations at Higher Incidence Angles

The methodology presented in Publication D [Schmitz et al., 2021c] allows for determining short-scale correlations of TLS observations. However, it has mainly been used for surfaces aligned orthogonally to the scanner. This has the effect that the differences between the reference surface and point clouds occur due to uncertainties in the rangefinder unit. The same procedure can be likewise applied to higher incidence angles. However, errors in the angular encoders have a higher impact when scanning with higher incidence angles

(cmp. Fig. 6.5). Thus, long-scale effects may bias the residuals between reference geometry and point cloud, and they cannot be simply calculated as their orthogonal distance. If a constant bias exists, for example, that the range is constantly measured too short when the incidence angle is high as explained in Sec. 3.4.2, it must be reduced to create stationary data, i.e., the VCM is constant at every location in the point cloud, which is necessary to apply the method introduced in Publication D [Schmitz et al., 2021c]. Studies evaluating the systematic effect of the incidence angle are currently working on proposing a calibration strategy [Linzer et al., 2021; Linzer & Neuner, 2022].

Suppose the impact of the incidence angle is considered. In that case, an empirical study can be carried out to evaluate the correlation structure at different ranges and incidence angles in terms of repeatability and predictability. This knowledge would be beneficial to enhance the synthetic VCM of Kerekes & Schwieger [2020] by object-related errors that create short-scale correlations.

6.2 Analysis of Long-Scale Correlations

Publication F [Jost et al., 2023b] presents an approach to generate a reference surface of larger objects of several meters in width and height to analyze the uncertainty of TLS. The deterministic part of the point cloud can be removed, and the stochastic part remains for the analysis. Figs. 6.3 and 6.4 depict the M3C2 differences between reference geometry and the point clouds that have been acquired in Publication F [Jost et al., 2023b] from seven different stations in two faces for the Leica ScanStation P50 and the Z+F Imager 5016. Face 1 denotes the first scan, and face 2 is the second scan, where the front and back faces of the scanner are swapped. The front face measures from 0° to 180° and the back face from 180° to 360°. In all 14 scans, the face transition lies on the wall. Even though both scanners have contemporarily been calibrated, systematic effects remain that cannot be modeled, but that correlate the measurements. A strategy is required to account for these correlations.

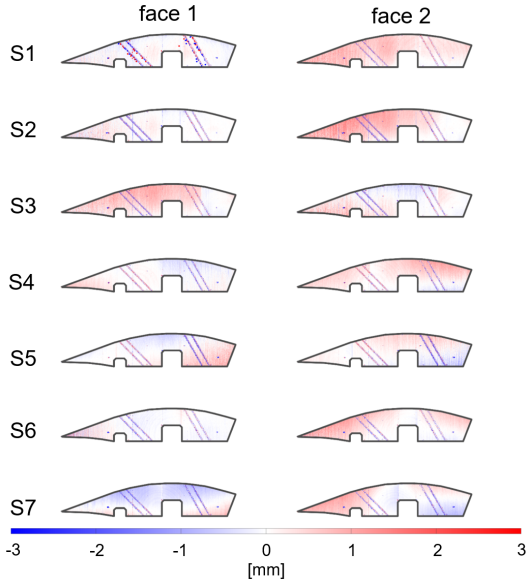

Abbildung 6.3: M3C2 differences between all calibrated single scans of the P50 and the reference geometry [Jost et al., 2023b].

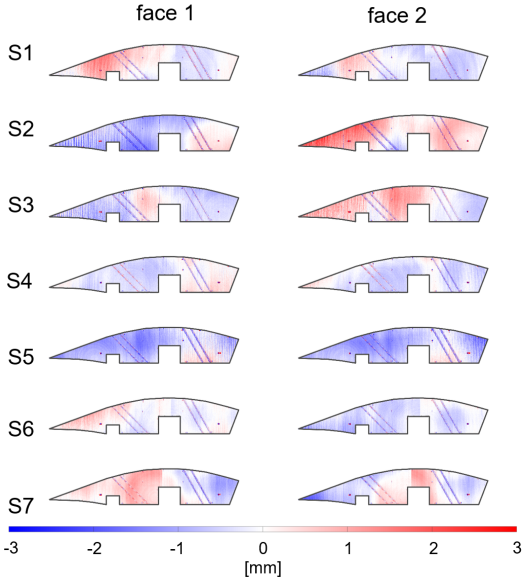

Abbildung 6.4: M3C2 differences between all calibrated single scans of the Imager 5016 and the reference geometry [Jost et al., 2023b].

One approach could be to eliminate these effects by building the average of multiple point clouds as done in Publication G [Jost et al., 2023a] or to model these deviations, for example, using B-Splines [Harmening & Neuner, 2020] and reduce them from the point cloud. However, modeling with B-Splines also needs a

sufficient stochastic model of the point cloud, which ends up in a circle of requirements where each application first needs the establishment of a reference geometry. Another option could be to forward model the long-scale effects. Since Kerekes & Schwieger [2020] already succeeded to integrate internal misalignments and atmospheric effects into the VCM, this could be further proceeded for the errors resulting from the scanning geometry as this has a huge influence on the long-scale correlations as seen in Publication F and G [Jost et al., 2023b,a]. Linzer et al. [2021] already succeeded to establish an automated evaluation approach for the incidence angle. If more knowledge is gained in this area, this effect may be calibrated, which reduces the impact of long-scale correlations. Furthermore, empirical studies that collect scans with numerous variations of the scanning geometry need to be carried out to detect dependencies between the deviations of point cloud and reference geometries and the scanning geometry. It should be further evaluated if it is possible to use explainable machine learning approaches [Roscher et al., 2020] to predict correlation patterns for different scanning configurations and object surfaces using for example surface normals, range, and intensity as input parameters.

Building the differences to a reference geometry of the Bonn Reference Wall mainly discovers out-of-plane uncertainties. If the horizontal angle is erroneous by $\Delta\varphi$, it is not detectable for a scanner that is oriented orthogonal to the wall. If the incidence angle is higher, the measured distance does not correspond to the measured horizontal angle, and the difference (red) between the true point (black cross) and measured point (green cross) is visible in the out-of-plane movement (Fig. 6.5). However, differences within the plane are not detectable. Therefore, to also investigate angular uncertainties, a different comparison strategy is necessary that considers in-plane differences as already demonstrated for deformation monitoring. Different approaches use vector fields to model in-plane-movements that are based on feature detection and matching [Holst et al., 2021] supported by a neural network [Gojcic et al., 2020]. These methods can also be applied to detect in-plane inconsistencies due to erroneous angular measurements to calibrate them or to integrate them into the VCM.

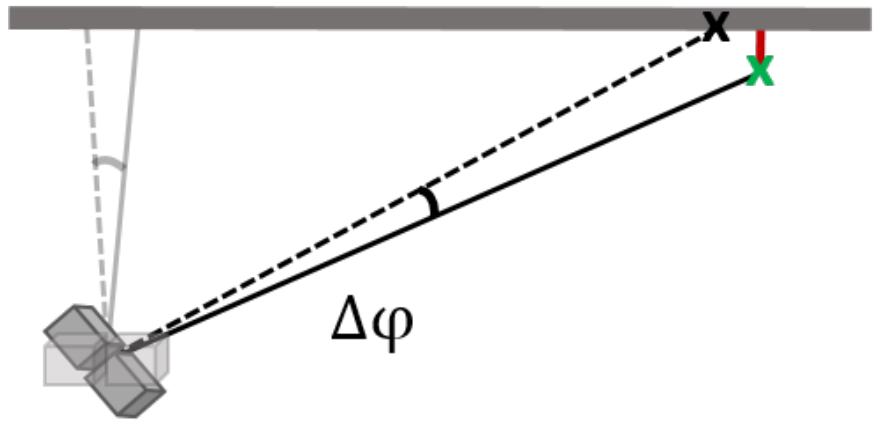

Abbildung 6.5: Impact of an erroneous horizontal angle on the point cloud comparison.

6.3 Combination of Short-Scale and Long-Scale Correlations

The computational effort is next to the quantification of correlations, one of the limiting factors while establishing a fully populated VCM. For example, the point cloud of Fig. 5.20 consists of approximately 331,000 points. Establishing a fully populated VCM for the polar observations would end up in a 1,000,000 x 1,000,000 matrix. Only introducing short-scale correlations makes the problem more benign, as only points within an area of a few centimeters are correlated, and the rest of the matrix is sparse. However, including also long-scale correlations leads to a fully populated matrix whose size exceeds the computational capacity of standard computers. Thus, it is unrealistic to combine both correlation types in one VCM.

As shown in Publication C [Schmitz et al., 2020], knowing the short-scale correlations can be used to fill the VCM of the point cloud. However, Publication B [Schmitz et al., 2020] demonstrated the derivation of the resolution capability to thin out the point cloud by irrelevant points so that the amount of data and the VCM are reduced, and only long-scale correlations need to be considered.

To also consider the long-scale effects, the reference geometry can be established according to Publication F [Jost et al., 2023b] and the residuals to the point cloud are calculated as in Figs. 6.3 and 6.4. Then, the long-scale effects can be removed by modeling the deviations as a kind of low-pass filtering so that only the short-scale effects remain that can be integrated into the VCM, which reduces its size. This would be very beneficial as long-scale effects increase the risk of misinterpreting them as deformations. Thus, there is no necessity to integrate both kinds of correlations. It is also possible to use only smaller parts of the point cloud, for example, for surface modeling, to make these computations easier.

7. Conclusions

Knowledge of the stochastic properties is vital for engineering tasks with high accuracy demands, such as an area-based deformation analysis. Several error sources can lead to random as well as systematic errors that need to be quantified, in the best scenario, calibrated, or integrated into the VCM of the point cloud. Since the interaction of different error sources is a complex process, the functional description of the effects on the point cloud is not straightforward and is not given for all error types. Especially the scanning configuration and the interaction of the laser beam with the object is leaking a functional error description. However, neighboring points are affected similarly by those error sources since the scanning geometry and the object's surface are almost the same. If the effects cannot be calibrated, this causes correlations between the single measurements that need to be accounted for in the VCM. Ignoring this fact can lead to biased estimates, wrong statistical testing, and the misinterpretation of systematic errors as geometry changes of the object. Since the laser beam, which is used for the electro-optical distance measurement, interacts with the environment and the object, this thesis mainly focuses on the rangefinder unit and less on the angular observations.

The goal of this thesis is to gain more profound knowledge of the stochastic properties, specifically on the rangefinder's precision and correlation between the measurements, to pave the way for future research to integrate these findings into a fully populated VCM. Due to the complex transmission behavior of the error sources and their effect on the point cloud, this thesis aims at developing strategies that do not focus on single error sources and tries to model them. However, it analyzes the stochastic part of the point cloud as a whole. This mostly relies on the fact that the object's surface must be well known to separate the deterministic and stochastic parts of the point cloud. The stochastic part is then analyzed in terms of rangefinder precision and short-scale and long-scale correlations. The established strategies are further developed to be easily replicated by qualified users to analyze their laser scanners. Following scientific contributions are achieved within this thesis to answer the open questions that are elaborated in Sec. 2.2:

A) Varying scanning configurations and object surface properties change the variances and covariances of the range observations. The intensity can fully describe the variances. This thesis proposes a simplified and efficient setup to determine the intensity-dependent range precision that can also be used – to a certain extent – to determine the range precision depending on scaled intensity values, as some manufacturers do not provide the raw ones. This allows for a more realistic representation of the VCM's main diagonal corresponding to range observations. Correlations resulting from the interaction of the laser beam with the object's surface are referred to as short-scale correlations herein. They can be determined in two ways: by using the resolution capability or a reference surface. This thesis presents methodologies to derive a spatial correlation function for short-scale correlations from the stochastic part of the point cloud, which can be used to fill the corresponding entries of the VCM. It further provides a methodology to deal with data sets of larger objects that are not stationary.

B) Due to short-scale correlations induced by neighboring laser spots partially illuminating the same surface, details that are supposed to be resolved by a high point density are smoothed. This thesis provides a new methodology to empirically determine the resolution capability of terrestrial laser scanners, revealing the actual level of detail that can be obtained with a certain scanner. Knowing this quantity allows to plan more efficient and economic measurement campaigns and the introduction of short-scale correlations reasoned by overlapping laser spots in the VCM.

C) The separation of the deterministic and the stochastic parts is essential for the empirical determination of the stochastic properties of a laser scan without taking individual error sources into account. Correlations that are induced by remaining errors from internal misalignments, the scanning geometry, or the atmosphere that cannot be calibrated have a larger extent with correlation lengths of several decimeters to several meters. For their investigation, the use of a large test object is inevitable. Therefore, the Bonn Reference Wall is tested to serve as a reference object. Due to deformations caused by temperature changes, it is not straightforward to use a sensor of higher accuracy to generate a reference geometry, but multiple scans with different configurations are averaged to remove remaining systematic errors. It

is demonstrated that this can, on the one hand, be used to remove the deterministic part of the point cloud and, on the other hand, perform an unbiased deformation analysis.

In conclusion, this thesis contributes to a better understanding of laser scanning uncertainty by developing new methodologies that allow for a better analysis of the range precision and short-scale and long-scale correlations. All strategies do not require specific knowledge of the error sources or specific laboratory conditions. So, they can be replicated by qualified users to understand their scanners' uncertainty better.

This thesis builds a basis for further research in the field of laser scanning uncertainty as it allows for the investigation of single components of the VCM and the setup of a VCM for point clouds of smaller and relatively planar surfaces. In the future, special focus must be paid to the integration of this information into a fully populated VCM. As outlined in Chap. 6, especially the combination of short-scale and long-scale correlations must be investigated to generate a stochastic model with a manageable size that can be used for unbiased surface approximations and deformation analyses.

8. List of Further Publications

This chapter provides an overview of further publications that are not directly related to this thesis and only involved participation as a co-author. It must be noted that the author changed her last name from Schmitz to Jost in 2022.

- Holst, C., Schmitz, B., & Kuhlmann, H. (2017a). Investigating the applicability of standard software packages for laser scanner based deformation analyses. FIG Working Week 2017, May 29 - June 02, Helsinki, Finland
- Holst, C., Schmitz, B., Schraven, A., & Kuhlmann, H. (2017b). Eignen sich in Standardsoftware implementierte Punktwolkenvergleiche zur flächenhaften Deformationsanalyse von Bauwerken? *Zeitschrift für Vermessungswesen zfv*, 2/2017, 98–110
- Holst, C., Schmitz, B., & Kuhlmann, H. (2016b). TLS–basierte Deformationsanalyse unter Nutzung von Standardsoftware. *In: Schriftenreihe DVW, Band 85, Terrestrisches Laserscanning 2016 (TLS 2016), Wißner Verlag, S. 39–58.*
- Holst, C., Janßen, J., Schmitz, B., Blome, M., Dercks, M., Schoch-Baumann, A., Blöthe, J., Schrott, L., Kuhlmann, H., & Medic, T. (2021). Increasing Spatio–Temporal Resolution for Monitoring Alpine Solifluction Using Terrestrial Laser Scanners and 3D Vector Fields. *Remote Sensing*, 13(6), 1192. `https://doi.org/10.3390/rs13061192`
- Koller, E., Jost, B., Wieser, A., Holst, C., & Kuhlmann, H. (2022). Bestimmung einer Referenzgeometrie zur Prüfung von Laserscannern. *DVW e.V. (Hrsg.): Terrestrisches Laserscanning 2022 (TLS 2022).* DVW-Schriftenreihe, Band 104, Wißner Verlag, Augsburg, S. 9-22
- Wieser, A., Balangé, L., Bauer, P., Gehrmann, T., Hartmann, J., Holst, C., Jost, B., Kuhlmann, H., Lienhart, W., Maboudi, M., et al. (2022). Erfahrungen aus einem koordinierten Vergleich aktueller Scanner. *DVW e.V. (Hrsg.): Terrestrisches Laserscanning 2022 (TLS 2022).* DVW-Schriftenreihe, Band 104, Wißner Verlag, Augsburg, S. 23-38
- Zimmermann, F., Schmitz, B., Klingbeil, L., & Kuhlmann, H. (2019). GPS Multipath Analysis Using Fresnel Zones. *Sensors*, 19(1), 25. `https://doi.org/10.3390/s19010025`

References

Abbas, M. A., Setan, H., Majid, Z., Idris, K. M., Ariff, M., Chong, A., & Lichti, D. (2014). The effect of datum constraints for terrestrial laser scanner self-calibration. In *FIG Congress 2014, Kuala Lumpur, Malaysia 16-21 June 2014*.

Alba, M., Fregonese, L., Prandi, F., Scaioni, M., & Valgoi, P. (2006). Structural monitoring of a large dam by terrestrial laser scanning. *International Archives of Photogrammetry, Remote Sensing and Spatial Information Sciences*, 36(part 5), 1–6.

Atkinson, P. M. & Lloyd, C. D. (2007). Non-stationary variogram models for geostatistical sampling optimisation: An empirical investigation using elevation data. *Computers & Geosciences*, 33(10), 1285–1300.

Barrell, H. & Sears, Junr, J. (1939). The refraction and dispersion of air and dispersion of air for the visible spectrum. *Philosophical Transactions of the Royal Society of London. Series A, Mathematical and Physical Sciences*, 238(786), 1–64.

Bartels, A. J. (1935). *Zur Morphologie geophysikalischer Zeitfunktionen.* S.-B. Preuß. Akad. Wiss.,30 (1935), 504–522.

Barzaghi, R., Cazzaniga, N. E., De Gaetani, C. I., Pinto, L., & Tornatore, V. (2018). Estimating and Comparing Dam Deformation Using Classical and GNSS Techniques. *Sensors*, 18(3), 756.

Bitenc, M., Kieffer, D. S., & Khoshelham, K. (2019). Range Versus Surface Denoising of Terrestrial Laser Scanning Data for Rock Discontinuity Roughness Estimation. *Rock Mechanics and Rock Engineering*, 52, 3103–3117.

Boehler, W., Vicent, M. B., & Marbs, A. (2003). Investigating laser scanner accuracy. *The International Archives of Photogrammetry, Remote Sensing and Spatial Information Sciences*, 34(Part 5), 696–701.

Bolkas, D. & Martinez, A. (2018). Effect of target color and scanning geometry on terrestrial LiDAR point-cloud noise and plane fitting. *Journal of Applied Geodesy*, 12(1), 109–127.

Centeno, J. A. S., Wutke, J. D., Mitishita, E. A., & Vögtle, T. (2010). Two Methods to Estimate the Spot Size of Terrestrial Laser Scanners. *Journal of Surveying Engineering*, 136(3), 126–131.

Chaudhry, S., Salido-Monzú, D., & Wieser, A. (2021). A Modeling Approach for Predicting the Resolution Capability in Terrestrial Laser Scanning. *Remote Sensing*, 13(4), 615.

Chmelina, K., Jansa, J., Hesina, G., & Traxler, C. (2012). A 3-d laser scanning system and scan data processing method for the monitoring of tunnel deformations. *Journal of Applied Geodesy*, 6(3-4), 177–185.

Chow, J., Lichti, D., & Glennie, C. (2011). Point-based versus plane-based self-calibration of static terrestrial laser scanners. *Int. Arch. Photogramm. Remote Sens. Spat. Inf. Sci*, 38(5/12), 121–126.

Clark, J. & Robson, S. (2004). Accuracy of measurements made with a Cyrax 2500 laser scanner against surfaces of known colour. *Survey Review*, 37(294), 626–638.

Cosarca, C., Jocea, A., & Savu, A. (2009). Analysis of error sources in Terrestrial Laser Scanning. *J. Geod. Cadaster*, 11, 115–124.

Cosser, E., Roberts, G. W., Meng, X., & Dodson, A. H. (2003). Measuring the dynamic deformation of bridges using a total station. In *Proceeding of the 11th FIG symposium on deformation measurements, Santorini, Greece* (pp. 25–28).

Cressie, N. (1986). Kriging nonstationary data. *Journal of the American Statistical Association*, 81(395), 625–634.

Cressie, N. (1993). *Statistics for Spatial Data.* John Wiley & Sons, Inc., New York, US.

Darbeheshti, N. & Featherstone, W. E. (2009). Non-stationary covariance function modelling in 2D least-squares collocation. *Journal of Geodesy*, 83(6), 495–508.

Eitel, J. U., Vierling, L. A., & Long, D. S. (2010). Simultaneous measurements of plant structure and chlorophyll content in broadleaf saplings with a terrestrial laser scanner. *Remote Sensing of Environment*, 114(10), 2229–2237.

Faro (2015). Faro Laser Scanner Focus 3D X130. User manual. available online: `https://knowledge.faro.com`, last accessed 2020/01/10.

Friedli, E. (2020). *Point Cloud Registration and Mitigation of Refraction Effects for Geomonitoring Using Long-Range Terrestrial Laser Scanning*. Dissertation, ETH Zurich.

Friedli, E., Presl, R., & Wieser, A. (2019). Influence of atmospheric refraction on terrestrial laser scanning at long range. In *Proceedings of the 4th Joint International Symposium on Deformation Monitoring (JISDM), Athens, Greece* (pp. 15–17).

Gojcic, Z., Zhou, C., & Wieser, A. (2020). F2S3: Robustified determination of 3D displacement vector fields using deep learning. *Journal of Applied Geodesy*, 14(2), 177–189.

Gordon, B. (2008). *Zur Bestimmung von Messunsicherheiten terrestrischer Laserscanner*. Dissertation, Technische Universität Darmstadt.

Harmening, C. & Neuner, H. (2020). Using Structural Risk Minimization to Determine the Optimal Complexity of B-Spline Surfaces for Modelling Correlated Point Cloud Data. *Journal of Geodesy*, 94(26), 1–25.

Heinz, E., Mettenleiter, M., Kuhlmann, H., & Holst, C. (2018). Strategy for Determining the Stochastic Distance Characteristics of the 2D Laser Scannner Z+F Profiler 9012A with Special Focus on the Close Range. *Sensors*, 18(7), 2253.

Heister, H. (2006). Zur standardisierten Überprüfung von terrestrischen Laserscannern (TLS). *Schriftenreihe des DVW*, 51, 35–44.

Heunecke, O., Kuhlmann, H., Welsch, W., Eichhorn, A., & Neuner, H. (2013). *Handbuch Ingenieurgeodäsie: Auswertung geodätischer Überwachungsmessungen*. 2. Auflage. Wichmann, Heidelberg, Germany.

Heunecke, O. & Welsch, W. (2000). Terminology and classification of deformation models in engineering surveys. *Journal of Geospatial Engineering*, 2(1), 35–44.

Holst, C., Artz, T., & Kuhlmann, H. (2014). Biased and unbiased estimates based on laser scans of surfaces with unknown deformations. *Journal of Applied Geodesy*, 8(3), 169–184.

Holst, C., Janßen, J., Schmitz, B., Blome, M., Dercks, M., Schoch-Baumann, A., Blöthe, J., Schrott, L., Kuhlmann, H., & Medic, T. (2021). Increasing Spatio–Temporal Resolution for Monitoring Alpine Solifluction Using Terrestrial Laser Scanners and 3D Vector Fields. *Remote Sensing*, 13(6), 1192. `https://doi.org/10.3390/rs13061192`.

Holst, C. & Kuhlmann, H. (2014). Aiming at self-calibration of terrestrial laser scanners using only one single object and one single scan. *Journal of Applied Geodesy*, 8(4), 295–310.

Holst, C. & Kuhlmann, H. (2016). Challenges and present fields of action at laser scanner based deformation analyses. *Journal of Applied Geodesy*, 10(1), 17–25.

Holst, C., Neuner, H., Wieser, A., Wunderlich, T., & Kuhlmann, H. (2016a). Calibration of Terrestrial Laser Scanners. *Allgem. Verm. Nachr.* 6/2016. S 147-157. Wichmann Verlag. Berlin.

Holst, C., Schmitz, B., & Kuhlmann, H. (2016b). TLS–basierte Deformationsanalyse unter Nutzung von Standardsoftware. *In: Schriftenreihe DVW, Band 85, Terrestrisches Laserscanning 2016 (TLS 2016), Wißner Verlag, S. 39–58.*

Holst, C., Schmitz, B., & Kuhlmann, H. (2017a). Investigating the applicability of standard software packages for laser scanner based deformation analyses. FIG Working Week 2017, May 29 - June 02, Helsinki, Finland.

Holst, C., Schmitz, B., Schraven, A., & Kuhlmann, H. (2017b). Eignen sich in Standardsoftware implementierte Punktwolkenvergleiche zur flächenhaften Deformationsanalyse von Bauwerken? *Zeitschrift für Vermessungswesen zfv*, 2/2017, 98–110.

Huxhagen, U., Kern, F., & Siegrist, B. (2011). Untersuchung zum Auflösungsvermögen terrestrischer Laserscanner mittels Böhler-Stern. *DGPF Tagungsband 20/2011*, (pp. 409–418).

Jelalian, A. V. (1992). *Laser radar systems*. Artech House, Boston, London.

Joeckel, R., Stober, M., & Huep, W. (2008). *Elektronische Entfernungs- und Richtungsmessung und ihre Integration in akutelle Positionierungsverfahren*. 5., neu bearbeitete und erweiterte Auflage. Wichmann. Heidelberg.

Jost, B., Coopmann, D., Holst, C., & Kuhlmann, H. (2023a). Real movement or systematic errors? – TLS-based deformation analysis of a concrete wall. *Journal of Applied Geodesy*, 17(2), 139–149. `https://doi.org/10.1515/jag-2022-0041`.

Jost, B., Holst, C., & Kuhlmann, H. (2023b). How to be more accurate than a single laser scan: Creating the reference geometry of a large wall. In A. Wieser (Ed.), *Beiträge zum 20. Internationalen Ingenieurvermessungskurs, 11.-14. April 2023, Zurich,*

Switzerland (pp. 131–144).: Wichmann, Berlin, Offenbach.

Jurek, T., Kuhlmann, H., & Holst, C. (2017). Impact of spatial correlations on the surface estimation based on terrestrial laser scanning. *Journal of Applied Geodesy*, 11(3), 143–155.

Kaasalainen, S., Jaakkola, A., Kaasalainen, M., Krooks, A., & Kukko, A. (2011). Analysis of incidence angle and distance effects on terrestrial laser scanner intensity: Search for correction methods. *Remote Sensing*, 3(10), 2207–2221.

Kaasalainen, S., Krooks, A., Kukko, A., & Kaartinen, H. (2009). Radiometric calibration of terrestrial laser scanners with external reference targets. *Remote Sensing*, 1(3), 144–158.

Kahmen, H. (2006). *Angewandte Geodäsie: Vermessungskunde – 20., völlig neu bearbeitete Auflage.* Walter de Gruyter. Berlin.

Kamerman, G. W. (1993). Laser radar. In *The Infrared & Electro-Optical Systems Handbook*. Infrared Information Analysis Center, Ann Arbor, Michigan and SPIE Optical Engineering Press, Bellingham, Washington. Chapter 1, 1–76.

Kauker, S., Holst, C., Schwieger, V., Kuhlmann, H., & Schön, S. (2016). Spatio-temporal Correlations of Terrestrial Laser Scanning. *Allgemeine Vermessungs Nachrichten (AVN).* 6/2016. S 170-182. Wichmann Verlag. Berlin.

Kauker, S. & Schwieger, V. (2017). A synthetic covariance matrix for monitoring by terrestrial laser scanning. *Journal of Applied Geodesy*, 11(2), 77–87.

Kerekes, G. & Schwieger, V. (2020). Elementary error model applied to terrestrial laser scanning measurements: study case arch dam Kops. *Mathematics*, 8(4), 593.

Kerekes, G. & Schwieger, V. (2021). Determining Variance-covariance Matrices for Terrestrial Laser Scans: A Case Study of the Arch Dam Kops. In *Contributions to International Conferences on Engineering Surveying: 8th INGEO International Conference on Engineering Surveying and 4th SIG Symposium on Engineering Geodesy* (pp. 57–68).: Springer, Cham.

Kermarrec, G. & Hartmann, J. (2021). Characterization of the optical encoder angular noise from terrestrial laser scanners. *Optics Express*, 29(11), 17011–17022.

Kermarrec, G., Kargoll, B., & Alkhatib, H. (2020). Deformation Analysis Using B-Spline Surface with Correlated Terrestrial Laser Scanner Observations–A Bridge Under Load. *Remote Sensing*, 12(5), 829.

Kermarrec, G. & Lösler, M. (2021). How to account for temporal correlations with a diagonal correlation model in a nonlinear functional model: a plane fitting with simulated and real TLS measurements. *Journal of Geodesy*, 95(1), 1–21.

Kermarrec, G., Lösler, M., & Hartmann, J. (2021). Analysis of the temporal correlations of TLS range observations from plane fitting residuals. *ISPRS Journal of Photogrammetry and Remote Sensing*, 171, 119–132.

Kermarrec, G., Paffenholz, J.-A., & Alkhatib, H. (2019). How Significant Are Differences Obtained by Neglecting Correlations When Testing for Deformation: A Real Case Study Using Bootstrapping with Terrestrial Laser Scanner Observations Approximated by B-Spline Surfaces. *Sensors*, 19(17), 3640.

Kermarrec, G. & Schön, S. (2016). Taking correlations in GPS least squares adjustments into account with a diagonal covariance matrix. *Journal of Geodesy*, 90(9), 793–805.

Kern, F. (2003). Automatisierte Modellierung von Bauwerksgeometrien aus 3D-Laserscanner-Daten. *Geodätische Schriftenreihe der Technischen Universitat Braunschweig.* Dissertation.

Kersten, T., Sternberg, H., & Stiemer, E. (2005a). First experiences with terrestrial laser scanning for indoor cultural heritage applications using two different scanning systems. *Proceedings of the ISPRS working group*, 5, 24–25.

Kersten, T. P., Sternberg, H., & Mechelke, K. (2005b). Investigations into the accuracy behaviour of the terrestrial laser scanning system Mensi GS100. *Proc. in the Optical 3D Measurement Techniques*, 1, 122–131.

Koch, K., Kuhlmann, H., & Schuh, W.-D. (2010). Approximating covariance matrices estimated in multivariate models by estimated auto-and cross-covariances. *Journal of Geodesy*, 84(6), 383–397.

Koch, K.-R. (1999). *Parameter Estimation and Hypothesis Testing in Linear Models.* Second, Updated and Enlarged edition. Springer, Berlin, Heidelberg (Germany).

Koch, K. R. (2008). Determining uncertainties of correlated measurements by Monte Carlo simulations applied to laserscanning. *Journal of Applied Geodesy*, 2(3), 139–147.

Koller, E., Jost, B., Wieser, A., Holst, C., & Kuhlmann, H. (2022). Bestimmung einer Referenzgeometrie zur Prüfung von Laserscannern. *DVW e.V. (Hrsg.): Terrestrisches Laserscanning 2022 (TLS 2022)*. DVW-Schriftenreihe, Band 104, Wißner Verlag, Augsburg, S. 9-22.

Kuhlmann, H. (2001). Importance of autocorrelation for parameter estimation in regression models. In *Proceedings of the 10th FIG International Symposium on Deformation Measurements, 19–22 March 2001, Orange, California* (pp. 354–361).

Kuhlmann, H. & Glaser, A. (2002). Investigation of new measurement techniques for bridge monitoring. In *2nd Symposium on Geodesy for Geotechnical and Structural Engineering, Berlin, Germany* (pp. 123–132).

Kuhlmann, H. & Holst, C. (2015). Flächenhafte Abtastung mit Laserscanning: Messtechnik, flächenhafte Modellierungen und aktuelle Entwicklungen im Bereich des terrestrischen Laserscannings. In *Handbuch der Geodäsie* (pp. 1–46). Springer Spektrum, Berlin, Heidelberg.

Kuhlmann, H. & Schwieger, V. (2015). *Das deutsche Vermessungs- und Geoinformationswesen 2015*, Kapitel Ingenieurgeodäsie, (pp. 739–780). Wichman Verlag, Berlin.

Kuhlmann, H., Schwieger, V., Wieser, A., & Niemeier, W. (2014). Engineering Geodesy-Definition and Core Competencies. *Journal of Applied Geodesy*, 8(4), 327–334.

Lague, D., Brodu, N., & Leroux, J. (2013). Accurate 3D comparison of complex topography with terrestrial laser scanner: Application to the Rangitikei canyon (NZ). *ISPRS Journal of Photogrammetry and Remote Sensing*, 82, 10–26.

Lambertus, T., Belton, D., & Helmholz, P. (2018). Empirical Investigation of a Stochastic Model Based on Intensity Values for Terrestrial Laser Scanning. *Allgemeine Vermessungsnachrichten (AVN)*, 3/2018, 43–52. Wichmann Verlag. Berlin.

Lee, I. S., Lee, J. O., Park, H. J., & Bae, K. H. (2010). Investigations into the influence of object characteristics on the quality of terrestrial laser scanner data. *KSCE Journal of Civil Engineering*, 14(6), 905–913.

Leica (2013). Leica ScanStation P20, Industry's Best Performing Ultra-High Speed Scanner. Data sheet. Available online: `https://w3.leica-geosystems.com/downloads123/hds/hds/scanstation_p20/brochures-datasheet/leica_scanstation_p20_dat_en.pdf`, (accessed on 16 May 2019).

Leica Geosystems (2017). Leica ScanStation P50 Because every detail matters. Data sheet, Heerbrugg, Switzerland, available online: `leica-geosystems.com`, last accessed 2020/01/10.

Leica Geosystems (2018). Leica RTC360 User Manual Version 1.0. User manual, Heerbrugg, Switzerland.

Lichti, D. D. (2004). A resolution measure for terrestrial laser scanners. *The International Archives of the Photogrammetry, Remote Sensing and Spatial Information Sciences*, 34(Part XXX), 6.

Lichti, D. D. (2007). Error modelling, calibration and analysis of an AM–CW terrestrial laser scanner system. *ISPRS Journal of Photogrammetry and Remote Sensing*, 61(5), 307–324.

Lichti, D. D. (2010). Terrestrial laser scanner self-calibration: Correlation sources and their mitigation. *ISPRS Journal of Photogrammetry and Remote Sensing*, 65(1), 93–102.

Lichti, D. D., Gordon, S. J., & Tipdecho, T. (2005). Error models and propagation in directly georeferenced terrestrial laser scanner networks. *Journal of Surveying Engineering*, 131(4), 135–142.

Lichti, D. D. & Harvey, B. (2002). The effects of reflecting surface material properties on time-of-flight laser scanner measurements. In *Proceedings of the Symposium on Geospatial Theory, Processing and Applications* (pp. 1–9).

Lichti, D. D. & Jamtsho, S. (2006). Angular resolution of terrestrial laser scanners. *Photogrammetric Record*, 21(114), 141–160.

Lienhart, W., Ehrhart, M., & Grick, M. (2017). High frequent total station measurements for the monitoring of bridge vibrations. *Journal of Applied Geodesy*, 11(1), 1–8.

Lindstaedt, M., Kersten, T., Meschelke, K., & Graeger, T. (2012). Prüfverfahren für terrestrische Laserscanner - Gemeinsame geometrische Genauigkeitsuntersuchungen verschiedener Laserscanner an der HCU Hamburg. *In: Luhmann, T., Schumacher, C. (Hrsg.): Photogrammetrie Laserscanning*

Optische 3D-Messtechnik - Beiträge der Oldenburger 3D-Tage. Wichmann Verlag, Berlin, Offenbach, pp. 264-275.

Linzer, F. & Neuner, H.-B. (2022). Transferability of an estimation procedure for distance deviations ofterrestrial laser scanners from laboratory to on-site conditions. In *5th Joint International Symposium on Deformation Monitoring (JISDM), 20-22 June 2022, Valencia, Spain* (pp. 319–326).

Linzer, F., Papčová, M., & Neuner, H. (2021). Quantification of Systematic Distance Deviations for Scanning Total Stations Using Robotic Applications. In *Contributions to International Conferences on Engineering Surveying* (pp. 98–108).: Springer, Cham.

Medić, T. (2021). *Efficient calibration strategies for panoramic terrestrial laser scanners*. Dissertation, Rheinische Friedrich-Wilhelms-Universität Bonn.

Medić, T., Holst, C., & Kuhlmann, H. (2017). Towards System Calibration of Panoramic Laser Scanners from a Single Station. *Sensors*, 17(5), 1145.

Medić, T., Kuhlmann, H., & Holst, C. (2019). Automatic In-Situ Self-Calibration of a Panoramic TLS from a Single Station Using 2D Keypoints. *ISPRS Annals of Photogrammetry, Remote Sensing and Spatial Information Sciences*, 42, 413–420.

Medić, T., Kuhlmann, H., & Holst, C. (2020). Designing and Evaluating a User-Oriented Calibration Field for the Target-Based Self-Calibration of Panoramic Terrestrial Laser Scanners. *Remote Sensing*, 12(1), 15.

Medić, T., Kuhlmann, H., & Holst, C. (2021). A priori vs. in-situ terrestrial laser scanner calibration in the context of the instability of calibration parameters. In *Contributions to International Conferences on Engineering Surveying, INGEO & SIG 2020, Dubrovnik, Croatia. Springer Proceedings in Earth and Environmental Sciences* (pp. 128–141).: Springer, Cham.

Moritz, H. (1972). Advanced least-squares methods. Report no. 175, Department of Geodetic Science, Ohio State University, USA.

Mukupa, W., Roberts, G. W., Hancock, C. M., & Al-Manasir, K. (2017). A review of the use of terrestrial laser scanning application for change detection and deformation monitoring of structures. *Survey Review*, 49(353), 99–116.

Muralikrishnan, B. (2021). Performance evaluation of terrestrial laser scanners-a review. *Measurement Science and Technology*, 32(7), 072001.

Muralikrishnan, B., Ferrucci, M., Sawyer, D., Gerner, G., Lee, V., Blackburn, C., Phillips, S., Petrov, P., Yakovlev, Y., Astrelin, A., et al. (2015). Volumetric performance evaluation of a laser scanner based on geometric error model. *Precision Engineering*, 40, 139–150.

Muralikrishnan, B., Rachakonda, P., Shilling, M., Lee, V., Blackburn, C., Sawyer, D., Cheok, G., & Cournoyer, L. (2016). *Report on the May 2016 ASTM E57. 02 Instrument Runoff at NIST, Part 1: Background Information and Key Findings*. US Department of Commerce, National Institute of Standards and Technology.

Niemeier, W. (2008). *Ausgleichungsrechnung: Statistische Auswertemethoden*. 2. Auflage. Walter de Gruyter. Berlin.

Pelzer, H. (1971). Zur Analyse geodätischer Deformationsmessungen. Deutsche Geodätische Kommission, Reihe C, No. 164, München.

Pesci, A. & Teza, G. (2008). Terrestrial laser scanner and retro-reflective targets: an experiment for anomalous effects investigation. *International Journal of Remote Sensing*, 29(19), 5749–5765.

Pfeifer, N., Dorninger, P., Haring, A., & Fan, H. (2007). Investigating Terrestrial Laser Scanning Intensity Data: Quality and Functional Relations. *Proceedings of the 8th International Conference on Optical 3-D Measurement Techniques*, (pp. 389–399).

Raschhofer, J., Kerekes, G., Harmening, C., Neuner, H., & Schwieger, V. (2021). Estimating Control Points for B-Spline Surfaces Using Fully Populated Synthetic Variance–Covariance Matrices for TLS Point Clouds. *Remote Sensing*, 13(16), 3124.

Reshetyuk, Y. (2009). *Self-calibration and direct georeferencing in terrestrial laser scanning*. Dissertation, Royal Institute of Technology (KTH), Stockholm (Sweden).

Reshetyuk, Y. (2010). A unified approach to self-calibration of terrestrial laser scanners. *ISPRS Journal of Photogrammetry and Remote Sensing*, 65(5), 445–456.

Roscher, R., Bohn, B., Duarte, M. F., & Garcke, J. (2020). Explainable machine learning for scientific insights and discoveries. *IEEE Access*, 8, 42200–42216.

Scaioni, M., Barazzetti, L., Giussani, A., Previtali, M., Roncoroni, F., & Alba, M. I. (2014). Photogrammetric techniques for monitoring tunnel deformation. *Earth Science Informatics*, 7(2), 83–95.

Scaioni, M., Marsella, M., Crosetto, M., Tornatore, V., & Wang, J. (2018). Geodetic and Remote-Sensing Sensors for Dam Deformation Monitoring. *Sensors*, 18(11), 3682.

Schabenberger, O. & Gotway, C. A. (2005). *Statistical Methods for Spatial Data Analysis*. Chapman & Hall/CRC Press, Boca Raton, Florida.

Schäfer, T. (2017). Berührungslose und flächenhafte Deformations- messungen an Betonoberflächen unter besonderer Berücksichtigung der Interaktion zwischen Laserstrahl und Oberfläche. Dissertation. Deutsche Geodätische Kommission, Reihe C, Nr. 805, München.

Schmitz, B., Coopmann, D., Kuhlmann, H., & Holst, C. (2021a). Using the Resolution Capability and the Effective Number of Measurements to Select the Right Terrestrial Laser Scanner. In *Contributions to International Conferences on Engineering Surveying, INGEO & SIG 2020, Dubrovnik, Croatia. Springer Proceedings in Earth and Environmental Sciences* (pp. 85–97).: Springer, Cham.

Schmitz, B., Holst, C., Medic, T., Lichti, D. D., & Kuhlmann, H. (2019). How to Efficiently Determine the Range Precision of 3D Terrestrial Laser Scanners. *Sensors*, 19(6), 1466. https://doi.org/10.3390/s19061466.

Schmitz, B., Kuhlmann, H., & Holst, C. (2020). Investigating the resolution capability of terrestrial laser scanners and its impact on the effective number of measurements. *ISPRS Journal of Photogrammetry and Remote Sensing*, 159, 41–52. https://doi.org/10.1016/j.isprsjprs.2019.11.002.

Schmitz, B., Kuhlmann, H., & Holst, C. (2021b). Deformation analysis of a reference wall towards the uncertainty investigation of terrestrial laser scanners. *Journal of Applied Geodesy*, 15(3), 189–206. https://doi.org/10.1515/jag-2020-0025.

Schmitz, B., Kuhlmann, H., & Holst, C. (2021c). Towards the empirical determination of correlations in terrestrial laser scanner range observations and the comparison of the correlation structure of different scanners. *ISPRS Journal of Photogrammetry and Remote Sensing*, 182, 228–241. https://doi.org/10.1016/j.isprsjprs.2021.10.012.

Schofield, W. & Breach, M. (2007). *Engineering Surveying, Sixth Edition*. Elsevier, Oxford (UK).

Schuh, W.-D. (2017). Signalverarbeitung in der physikalischen Geodäsie. In *Erdmessung und Satellitengeodäsie* (pp. 73–121). Springer Spektrum, Berlin.

Schwieger, V. (1999). *Ein Elementarfehlermodell für GPS-Überwachungsmessungen: Konstruktion und Bedeutung interepochaler Korrelationen*. Wissenschaftliche Arbeiten der Fachrichtung Vermessungswesen der Universität Hannover, Heft Nr. 231, Hannover.

Sherman, M. (2011). *Spatial Statistics and Spatio–Temporal Data, Covariance Functions and Directional Properties*. John Wiley & Sons, Ltd, West Sussex, United Kingdom.

Soudarissanane, S. (2016). *The geometry of terrestrial laser scanning; identification of errors, modeling and mitigation of scanning geometry*. Dissertation, TU Delft (Netherlands).

Soudarissanane, S., Lindenbergh, R., Menenti, M., & Teunissen, P. (2011). Scanning geometry: Influencing factor on the quality of terrestrial laser scanning points. *ISPRS Journal of Photogrammetry and Remote Sensing*, 66(4), 389–399.

Strauss, A., Bien, J., Neuner, H., Harmening, C., Seywald, C., Österreicher, M., Voit, K., Pistone, E., Spyridis, P., & Bergmeister, K. (2020). Sensing and monitoring in tunnels testing and monitoring methods for the assessment of tunnels. *Structural Concrete*, (pp. 1–21).

Taubenheim, J. (1969). *Statistische Auswertung geophysikalischer und meteorologischer Daten*. Akademische Verlagsgesellschaft Geest & Portig K.-G. Leipzig.

Voegtle, T., Schwab, I., & Landes, T. (2008). Influences of different materials on the measurements of a terrestrial laser scanner (TLS). In *Proc. of the XXI Congress, The International Society for Photogrammetry and Remote Sensing, ISPRS2008*, volume 37 (pp. 1061–1066).

Voegtle, T. & Wakaluk, S. (2009). Effects on the measurements of the terrestrial laser scanner HDS 6000 (Leica) caused by different object materials. *Proceedings of ISPRS Work*, 38(2009), 68–74.

Vosselman, G. & Maas, H.-G. (2010). *Airborne and Terrestrial Laser Scanning*. Whittles Publishing, Dunbeath, Scotland (UK).

Walser, B. & Gordon, B. (2013). Der Laserscanner, eine Black-Box? *Schrriftenreihe DVW, Band 72, Terrestrisches Laserscanning 2013 (TLS 2013)*, (pp. 149–164).

Welsch, W. & Heunecke, O. (2001). Models and terminology for the analysis of geodetic monitoring observations, Official report of the ad-hoc committee of FIG working group 6.1. *The 10th FIG International Symposium on Deformation Measurements, 19–22 March 2001, Orange, California, USA*, (pp. 390–412).

Wieser, A., Balangé, L., Bauer, P., Gehrmann, T., Hartmann, J., Holst, C., Jost, B., Kuhlmann, H., Lienhart, W., Maboudi, M., et al. (2022). Erfahrungen aus einem koordinierten Vergleich aktueller Scanner. *DVW e.V. (Hrsg.): Terrestrisches Laserscanning 2022 (TLS 2022)*. DVW-Schriftenreihe, Band 104, Wißner Verlag, Augsburg, S. 23-38.

Witte, B. & Sparla, P. (2011). *Vermessungskunde und Grundlagen der Statisktik für das Bauwesen. 7., überarbeitete und erweiterte Auflage*. Wichmann. Berlin und Offenbach, Germany.

Wujanz, D., Burger, M., Mettenleiter, M., & Neitzel, F. (2017). An intensity-based stochastic model for terrestrial laser scanners. *ISPRS Journal of Photogrammetry and Remote Sensing*, 125, 146–155.

Wujanz, D., Burger, M., Tschirschwitz, F., Nietzschmann, T., Neitzel, F., & Kersten, T. (2018). Determination of Intensity-Based Stochastic Models for Terrestrial Laser Scanners Utilising 3D-Point Clouds. *Sensors*, 18(7), 2187.

Wunderlich, T., Niemeier, W., Wujanz, D., Holst, C., Neitzel, F., & Kuhlmann, H. (2016). Areal deformation analysis from TLS point cloud–The challenge. *Allgemeine Vermessungs Nachrichten*, 123, 340–351.

Wunderlich, T., Wasmeier, P., Ohlmann-Lauber, J., Schäfer, T., & Reidl, F. (2013). *Objective Specifications of Terrestrial Laserscanners – A Contribution of the Geodetic Laboratory at the Technische Universität München*. Technical report, Blue Series Books at the Chair of Geodesy. Volume 21, Technische Universität München.

Yu, J., Zhu, P., Xu, B., & Meng, X. (2017). Experimental assessment of high sampling-rate robotic total station for monitoring bridge dynamic responses. *Measurement*, 104, 60–69.

Zámečníková, M. & Neuner, H. (2018). Methods for quantification of systematic distance deviations under incidence angle with scanning total stations. *ISPRS Journal of Photogrammetry and Remote Sensing*, 144, 268–284.

Zámečníková, M., Wieser, A., Woschitz, H., & Ressl, C. (2014). Influence of surface reflectivity on reflectorless electronic distance measurement and terrestrial laser scanning. *Journal of Applied Geodesy*, 8(4), 311–326.

Zhao, X., Kermarrec, G., Kargoll, B., Alkhatib, H., & Neumann, I. (2019). Influence of the simplified stochastic model of TLS measurements on geometry-based deformation analysis. *Journal of Applied Geodesy*, 13(3), 199–214.

Zimmermann, F., Schmitz, B., Klingbeil, L., & Kuhlmann, H. (2019). GPS Multipath Analysis Using Fresnel Zones. *Sensors*, 19(1), 25. `https://doi.org/10.3390/s19010025`.

Zogg, H. (2008). Investigations of high precision terresrtrial laser scannning with emphasis on the development of a robust close-range 3D–laser scanning system. Dissertation, Institut für Geodäsie und Photogrammetrie an der Eidgenössischen Technischen Hochschule Zürich, Mittelungen Nr. 98.

Zoller + Fröhlich (2018). Reaching new levels Z+F Imager 5016 User Manual V 1.8. User manual, Wangen im Allgäu, Germany.